January 2020

Application And Development Of Advanced Atomic-Scale Analysis And Simulations For Complex Systems

Hyeonseok Lee

APPLICATION AND DEVELOPMENT OF ADVANCED ATOMIC-SCALE ANALYSIS AND SIMULATIONS FOR COMPLEX SYSTEMS

by

Hyeonseok Lee

Bachelor of Science, Inha University (South Korea), 2010

Master of Engineering, Illinois Institute of Tech. (USA), 2017

A Dissertation
Submitted to the Graduate Faculty

of the

University of North Dakota

In partial fulfillment of the requirements

for the degree of

Doctor of Philosophy

Grand Forks, North Dakota

August

2020

Name: Hyeonseok Lee

Degree: Doctor of Philosophy

This document, submitted in partial fulfillment of the requirements for the degree from the University of North Dakota, has been read by the Faculty Advisory Committee under whom the work has been done and is hereby approved.

DocuSigned by:
Hui Pu
Dr. Hui Pu

DocuSigned by:
Vamegh Rasouli
Dr. Vamegh Rasouli

DocuSigned by:
Farnaz A. Shakib
Dr. Farnaz A. Shakib

DocuSigned by:
Hossein Salehfar
Dr. Hossein Salehfar

This document is being submitted by the appointed advisory committee as having met all the requirements of the School of Graduate Studies at the University of North Dakota and is hereby approved.

DocuSigned by:
Chris Nelson
Chris Nelson
Dean of the School of Graduate Studies

7/27/2020
Date

PERMISSION

Title APPLICATION AND DEVELOPMENT OF ADVANCED ATOMIC-SCALE ANALYSIS AND SIMULATIONS FOR COMPLEX SYSTEMS

Department Petroleum Engineering

Degree Doctor of Philosophy

In presenting this dissertation in partial fulfillment of the requirements for a graduate degree from the University of North Dakota, I agree that the library of this University shall make it freely available for inspection. I further agree that permission for extensive copying for scholarly purposes may be granted by the professor who supervised my dissertation work or, in his absence, by the Chairperson of the department or the dean of the Graduate School. It is understood that any copying or publication or other use of this dissertation or part thereof for financial gain shall not be allowed without my written permission. It is also understood that due recognition shall be given to me and to the University of North Dakota in any scholarly use which may be made of any material in my dissertation.

Hyeonseok Lee
June 21, 2020

TABLE OF CONTENTS

LISTS OF FIGUTRES

LISTS OF TABLES

ACKNOWLEDGEMENTS

I would like to express my deepest gratitude to my advisors Dr. Mehdi Ostadhassan and Dr. Hui Pu for the insightful guidance, great patience, and sincere encouragement during my time in the Ph.D. program at the University of North Dakota. Without his invaluable support and trust, the dissertation would not be possible. I would also want to thank Dr. Vamegh Rasouli, Dr. Farnaz A. Shakib, Dr. Hossein Salehfar who honored me for being members of my committee.

I wish to express my sincere appreciation to the members of my advisory Committee for their guidance and support during my time in the doctoral program at the University of North Dakota.

The financial support of the North Dakota Industrial Commission (NDIC) is highly appreciated.

Finally, and most importantly, I would like to give my great thanks to my parents and my wife for their encouragement, patience, and love.

To my wonderful wife Sung-Eun Park,

Brought to me by God's beautiful grace.

Partner with me on a vibrant journey, full of life.

ABSTRACT

A series of studies have investigated the applicability of kerogen, which is an amorphous and insoluble organic matter abundant in unconventional shale formations. This geo−materials are known to have undergone significant alteration in chemical structure during thermal maturation which is characterized using a combination of solid−state ^{1}H & ^{13}C−NMR, X−ray photoelectron spectroscopy (XPS), Fourier transform infrared (FTIR), Matrix-assisted laser desorption ionization-time of flight mass spectrometry (MALDI-TOF-MS) techniques. For these studies, four kerogen samples (type−II) from the Bakken Formation were selected based on the differences in their thermal maturity, as well as representing the pre−oil and oil window stages as measured through organic petrology and bulk geochemical screening of the samples. Results documented a systematic structural change in these four samples where the ratio of CH_3/CH_2 increased when the maturity increases, along with the presence of shorter aliphatic chain length. Furthermore, the aromatic carbon structure becomes more abundant in higher maturities and oil window stages. It concluded that, the structural and chemical changes that occurs in the organic matter involves defunctionalization of heteroatom functional groups, coupled with an increase in cross−linked carbon in the residual remaining kerogen. Also molecular weight distribution variations in kerogen samples revealed the rate of change in molecular mass populations as a function of thermal maturity.

The studies using computational simulation techniques investigated the applicability of kerogen for separation of the mixture of gases (CO_2 and CH_4) in dry and wet (brine) conditions for an effective storage and injection operation. Here, through grand canonical Monte Carlo (GCMC)/molecular dynamics (MD) simulations, the studies of thermodynamics and kinetics investigated the CO_2 transportation and adsorption behavior on three-dimensional (3D) kerogen molecular models from the Bakken, which contains non-periodically arrayed functional groups. The stronger interaction of CO_2 molecules with the model leads to the penetration of CO_2 molecules to the sub-surface levels. And, the concentration of brine shows a positive effect for CO_2/CH_4 selectivity that supports our goals of sequestration and enhanced production. These results suggest the important role of kerogen in the separation and transport of gas in organic−rich shale plays that are the target for sequestration of CO_2 and/or enhanced oil recovery (EOR).

PART 1 RESEARCH OVERVIEW

CHAPTER 1. INTRODUCTION & OBJECTIVE

1. Introduction

In the past few years, there has been growing attention to organic-rich shale reservoirs due to their importance in hydrocarbon production and CO_2 sequestration (Alvarado & Manrique, 2010; Jia et al., 2019). The high abundance of total organic carbon (TOC) in shale layers, which were deposited in these rocks hundreds of millions of years ago, would lead to the generation of oil and gas through thermal maturation. This process takes place due to the exposure of rocks containing organics to adequate temperature and pressure as the depth of burial increases. During this geologic process, the organic matter known as kerogen, which has a complex and amorphous molecular structure, breaks down and goes through a significant structural and compositional transformation (Durand, 1980; Rullkötter & Michaelis, 1990). In this regard, the study of kerogen structural changes has the potential to better characterize CO_2 sequestration and the enhanced oil recovery (EOR) methods (Lee et al., 2019). However, there is a significant difficulty in understanding the mechanism of kerogen cracking coupled to hydrocarbon generation due to chemical heterogeneity and complexity of the kerogen molecular structure. Moreover, the limitation of analytical methods could not thoroughly provide quantitative molecular information of kerogen structure (Vandenbroucke & Largeau, 2006).

Kerogen characterization methods such as visual kerogen analysis and pyrolysis (bulk geochemical techniques) are limited to the determination of the type of kerogen, maturity level, and hydrocarbon generating potential. Hence, in order to obtain the detailed structural information of kerogen, a number of spectroscopic techniques have been deployed (Clough et al., 2015; Tong et al., 2011, 2016). The methods mentioned are destructive in addition to the limited information they can provide, thus other non−destructive methods such as Fourier transform infrared (FTIR) spectroscopy, Raman spectroscopy, X−ray photoelectron spectroscopy (XPS), X−ray diffraction (XRD), MALDI-TOF-MS (Matrix-assisted laser desorption ionization-time of flight mass spectrometry), and ^{1}H & ^{13}C solid−state nuclear magnetic resonance (^{1}H & ^{13}C−NMR) have been utilized to obtain quantitative structural information from the kerogen (Khatibi et al., 2018; Lis et

al., 2005; Z. Wei et al., 2005). These direct methods can examine the solid kerogen sample without imposing any alterations so that the results would enable studying the structure and assist in building macromolecular models of kerogen by computational technique at the same time (Khatabi & Aghajanpour, 2018).

Kerogen, composed of mainly carbon, hydrogen, oxygen, nitrogen, and sulfur, experiences major structural and compositional changes as it undergoes maturation as a function of burial depth, i.e. pressure and temperature (Abarghani et al., 2018) and finally breaks down to petroleum and other by-products. Therefore, building computational molecular models for kerogen is a much desired but challenging task, and not surprisingly, it has been continuously evolving with the advancements in computational methods (Bousige et al., 2016; H. Wang et al., 2019). In addition to the development of the molecular models for this purpose, the computational techniques have also become frequent tools for simulating the gas adsorption and desorption processes. Simulation of adsorption behavior is important since organic−rich shales are becoming a repository of greenhouse gas storage which can also improve their productivity in CO_2 enhanced oil recovery (EOR) and sequestration.

Moreover, it is a challenge to produce hydrocarbons and store CO_2 simultaneously due to the interference of hydrocarbons and brine in CO_2 sorption (Alvarado & Manrique, 2010). Moreover, the CO_2 selectivity, the ratio of the adsorbed CO_2 onto the membrane (here kerogen) over hydrocarbons (Zhang et al., 2015), is drastically affected by temperature and pressure (Alvarado & Manrique, 2010). Hence, it is necessary to have a clear picture of CO_2 diffusion kinetics and thermodynamics over a range of brine concentrations at different temperatures and pressures for more efficient CO_2 separation, injection and sequestration. The investigation of CO_2 selectivity in the presence of mixtures (CO_2, CH_4, and the brine) is the key to improving CO_2 separation in unconventional organic-rich reservoirs.

2. Research Objective

In these studies, four isolated (extracted) kerogens from the mineral matrix at four different stages of natural thermal maturity from the Bakken Shale formation, from pre−oil to oil window stages, were examined by a combination of non−destructive analytical methods (^{1}H & ^{13}C−NMR, XPS, FTIR, MALDI-TOF-MS) for molecular weight quantification along with chemical and structural

analysis. This study aimed to identify structural characteristics and evolution of solid−state organic compounds as it undergoes thermal maturity in nature and to discover these changes in terms of quantitative and qualitative information from a chemical structure point of view. Additionally, the study investigated other aspects of thermal maturation that can help us explain processes that would generate hydrocarbons from the organic compounds in the source rock.

Secondly, in order to precisely estimate the capacity of organic matter in terms of adsorption for sequestration and/or associated mechanisms for enhanced oil recovery, building a 3D molecular model of the Bakken kerogen has become imperative. Here, the study reports a new representative molecular model for organic matter from the Bakken (kerogen type II) based on previous experimental chemical compositional data (R. Kelemen et al., 2007). The models were validated with gas (CO_2 and N_2) adsorption isotherms based on both experimental techniques and theoretical simulations. CO_2 and N_2 diffusion behaviors in the kerogen system are also investigated to present a complete picture of interactions that would occur between kerogen and gas molecules.

Additionally, the representative models of Bakken kerogen contain surface pores and functional groups consisting of carbon, hydrogen, oxygen, nitrogen, and sulfur. Having established the reliability of our Bakken kerogen model, here, the study employs these models to demonstrate the applicability of kerogen for separation of the mixture of CO_2 and CH_4 gases in dry and wet (brine) conditions via molecular simulations. Here the studies emphasized the effect of brine as the formation water and investigated the interaction of brine with the CO_2 and CH_4 gases and its overall effect on the gas sorption by kerogen (Fakcharoenphol et al., 2014). The study analyzed the diffusion and separation of CO_2/CH_4/brine systems which would affect the performance of the EOR process in particular tight shale formations where the improvement of recovery through CO_2 injection is still ambiguous and under research (Edwards et al., 2015; Jin et al., 2017).

CHAPTER 2. STRUCTURAL CHARACTERIZATION OF ORGANIC COMPOUNDS IN SHALE PLAY

1. Materials and Methods

1.1 Samples

Solid−state organic compound, type II kerogen samples were extracted from four different wells in the Bakken formation which is one of the largest unconventional shale oil plays in North America and is currently being studied for unconventional CO_2 EOR and sequestration (Lin & Patrick Ritz, 1993; Michels et al., 1996; Salmon et al., 2009). Initially, the degree of maturity of four Bakken kerogen samples (sample A−D) were examined by bitumen reflectance (%SBR_o) along with bulk geochemical properties using Rock−Eval 6 pyrolysis that is summarized in Table 1. In Figure 1 and Table 1, samples A−B are at the thermally immature (pre−oil window) stage, while, samples C−D are at the peak mature (oil window) stage.

Table 1. Properties of four solid−state organic compound (kerogen) samples (type II)[a].

Sample No.	T_{max} (°C)	TOC (wt %)	HI (mg/g C)	SBRo (%)
A	428	14.56	569	0.33
B	432	15.76	531	0.49
C	449	12.69	260	0.72
D	452	16.36	171	0.94

[a]The values were examined by the UV reflectance (%SBR_o) and Rock−Eval 6 with parameters: Tmax, TOC (Total organic carbon), HI (hydrogen index).

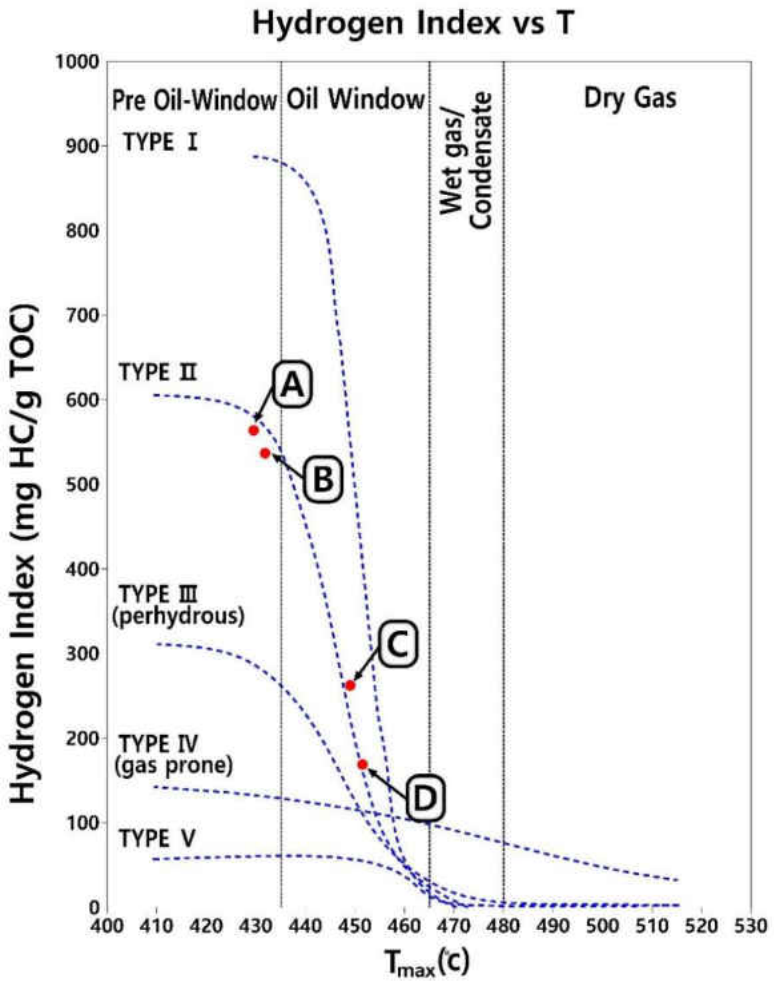

Figure 1 Selected samples A−D are following kerogen type II thermal maturity trend where Samples A−B are at the thermally immature (pre−oil window) stage, and samples C−D are at the peak mature (oil window) stage.

1.2 Solid−State ^{1}H & ^{13}C−NMR (Nuclear Magnetic Resonance)

Solid−state ^{1}H & $^{1}3C$−NMR analysis was carried out using a Bruker Avance III HD spectrometer with cross polarization−magic angle spinning (CP/MAS). The kerogen sample (100−150 mg) was packed and spun at 5 kHz. A contact time of 1.5 ms and recycle delay time of 5 s were used in the cross−polarization (CP). Resonance frequencies of ^{1}H−NMR and ^{13}C−NMR were 500 MHz and 125 MHz, respectively with the spectral widths of 10 kHz and 25 kHz for ^{1}H−NMR and ^{13}C−NMR. The relative proportion of different carbon types in the samples was quantified through curve fitting of the ^{13}C−NMR spectrum, which was conducted with the ratios of Gaussian to Lorentzian

distribution; the full width at half−maximum (fwhm). The details of structural parameters and assignments of chemical data shifts are presented.

1.3 XPS (X−ray Photoelectron Spectroscopy)

Freshly−powdered samples were pressed on indium foils and analyzed by a Al Kα (1486.6 eV) X−ray source with a pass energy of 89.5 eV and 44.75 eV for the survey and higher−resolution scans, respectively. During the XPS measurements, the pressure was kept at or below 1×10^{-9} mbar. The angle between the X−ray source, which is aligned along the surface normal, and the spectrometer is 54.7. All the XPS core−level spectra were analyzed using Augerscan and Origin software's. The core−level peaks are fitted using a Gaussian−Lorentzian (GL) function to include the instrumental response function along with the core−level line shape. The secondary electron background was subtracted using a Shirley function. The charging of the sample was compensated by irradiating the sample with an electron−flood gun (5 eV) (Van der Heide P., 2011).

1.4 ATR−FTIR (Fourier transform infrared spectroscopy)

Infrared spectra of kerogen samples were recorded in adsorption between 450 and 4000 cm^{-1} wavelengths using a Thermo Fisher Scientific, Nicolet iS50 FTIR Spectrometer. Four kerogen samples were pulverized using a ball mill before the characterizations. Fourier transform infrared (FTIR) spectroscopy using attenuated total reflectance (ATR) was utilized to analyze the isolated kerogens. Unlike transmittance FTIR, ATR does not require that kerogen samples to be mixed with potassium bromide and form into pellets under high pressure, which reduces the time needed to prepare the samples. Kerogen samples were placed in contact with an internal reflection material, and IR spectra were obtained based on the excitation of the molecular vibrations of chemical bonds by the absorption of light. The stretching absorption of a vibrating chemical bond is observed at higher frequencies (wavenumbers) than the corresponding bending or bond deformation vibrations (Chen et al., 2015; Coates, 2006). In this study, it was decided to analyze the C-H set of stretch vibrations that are observed in kerogen samples, which is also done in previous studies (Craddock et al., 2018). It should be noted that recorded bands of the absorption were identified through comparison with the published spectra shown in Table 2.

Table 2 Saturated aliphatic group and aromatic ring group frequencies.

Origin	Group frequency (cm^{-1})	Functional Group/ Assignment
Methyl(-CH_3)	2970-2950	Methyl C-H asymmetric stretch
	2880-2860	Methyl C-H symmetric stretch
Methylene (>CH_2)	2935-2915	Methylene C-H asymmetric stretch
	2865-2845	Methylene C-H symmetric stretch
Aromatic (C-H)	3130-3070	Aromatic C-H stretch

Table 2 presents the stretching absorption for C-H stretch vibrations for methyl (-CH_3), methylene (>CH_2), and aromatics (C-H). These are the most common characteristics of an organic compound containing the aliphatic fragments. The intensities observed are corresponding to the asymmetric and symmetric stretching and bending of the C-H bonds of the central carbon atom. The C-H stretching vibrations for the saturated aliphatic occur between 3000 and 2800 cm^{-1}, and the aromatic ring stretch vibrations occur between 3130 and 3070 cm^{-1}. IR structural evaluations, which have been established in earlier studies (Lis et al., 2005), were calculated from acquired spectra. The intensities of bands assigned by the functional groups were deconvoluted through a curve fitting procedure (Chen et al., 2015; Coates, 2006). The CH_3/CH_2 ratio ($I_{(2970-2950)}/I_{(2935-2915)}$) indicates the average chain length of aliphatic and the degree of chain branching. Moreover, the aromaticity index ($I_{(3130-3070)}/(I_{(2970-2950)}+I_{(2935-2915)})$ represents the degree of aromatic structures to aliphatic chain structures (Zodrow et al., 2012).

1.5 MALDI-TOF-MS

The AB SCIEX TOF/TOF 5800 mass spectrometry system was used for the identification and relative quantitation of kerogen molecular weight. A dilution series of kerogen powder were prepared for two different test setups, in the absence and the presence of the matrix. In the second set up where the matrix is presented, dilutions were mixed with α-Cyano-4-hydroxycinnamic acid (α-CHCA) in 1:1 ratio. The matrix, α-CHCA, is commonly used in conjunction with organic molecules, particularly for relatively higher-weight ones (Beavis et al., 1992). Each sample (1 μL) was spotted onto a standard stainless steel plate and allowed to air-dry. Spectra were acquired with

MS reflector mode for 1,000 shots, and the analysis was conducted over a range of 60 to 5000 Da by use of an adjusted accelerating voltage.

2. Results

2.1. Solid−State ^{1}H & ^{13}C−NMR

Aromatic and aliphatic proton regions of ^{1}H–NMR spectrum provide relatively qualitative information of hydrogen at different maturity levels (Wang et al., 2018). From the acquired spectra in Figure 2 (left), aromatic and aliphatic protons exist in the 6.4–8.3 ppm range and 0.5–4.3 ppm range, respectively. The ^{1}H−NMR spectra of sample A–D in Figure 2 (left) show a broad asymmetric line centered around 0–1 ppm (centered at 0.64, 0.24, 0.54, and 0.91 ppm, respectively). Sample A (immature) has a strong intensity in the range of the aliphatic protons between 0.5 to 4.3 ppm; the peak at 4.15 ppm indicates that the ratio of aliphatic protons to the aromatic ring is higher than the rest of the samples. In this regard, the results reveal that the shape of the ^{1}H−NMR spectrum becomes sharp as the degree of maturity increases, which manifests the number of protons attached to aliphatic carbon reduces.

The ^{13}C−NMR spectra of kerogen samples mainly reveal three regions: the aliphatic region at 0–90 ppm, the aromatic region at 100–165 ppm, and carbonyl/carboxyl carbon region at 165–220 ppm (Qing Wang et al., 2018; Q. Wei & Tang, 2018). Figure 2 (right) illustrates that the ^{13}C−NMR spectrum of immature kerogen is distinct from the mature one in the range of the aromatic carbons between 90 to 220 ppm. Highly matured kerogen has a stronger intensity in ^{13}C–NMR spectrum related to aromatic structure. To acquire the details of carbon structural information, overlapping peak resolving of the ^{13}C–NMR spectra are deconvoluted by the fitting procedure.

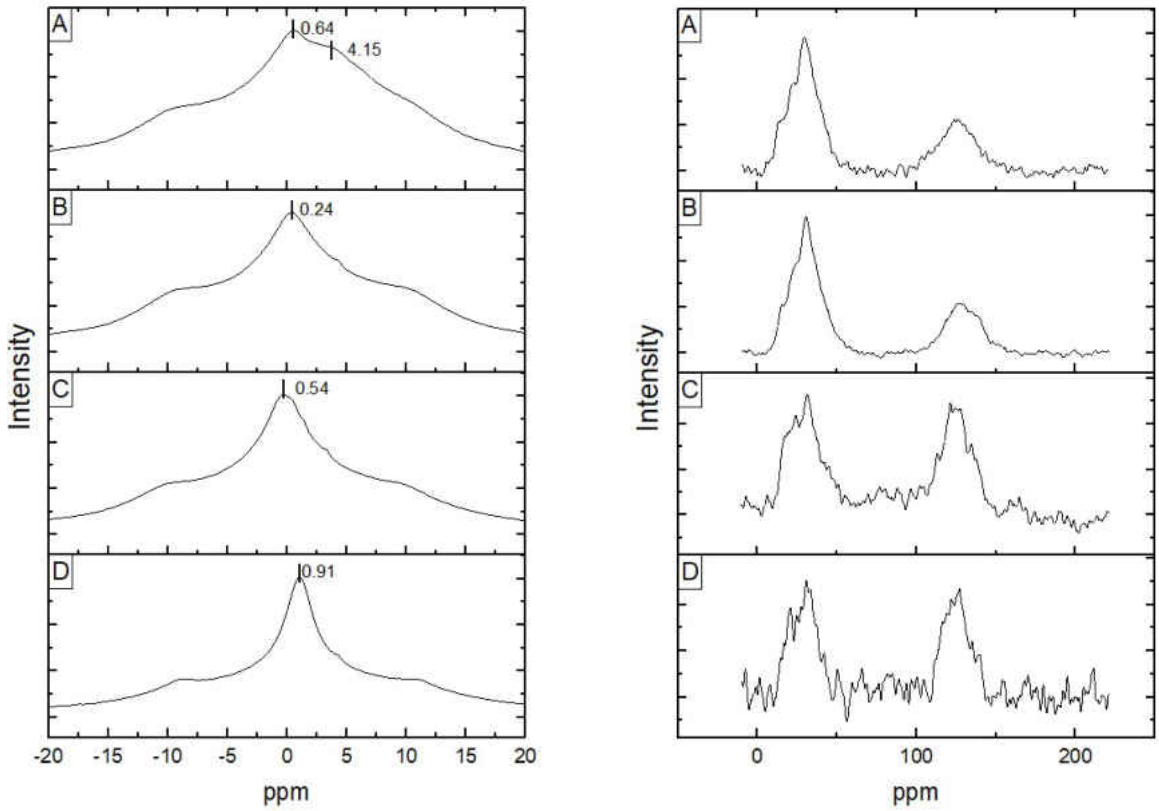

Figure 2. ^{1}H−NMR (left) and ^{13}C−NMR (right) spectra of kerogen samples from samples A-D.

All ^{13}C chemical shift (ppm) were measured and assigned in carbon structural functionalities (f_{al}^{1}: aliphatic methyl, f_{al}^{2}: aromatic methyl, f_{al}^{H1}: methylene, f_{al}^{H2}: quaternary carbon, f_{al}^{O1}: methoxyl/aromatic methoxyl, f_{al}^{O2}: aliphatic carbon bonded to oxygen in cyclic hydrocarbon, f_{ar}^{H}: protonated aromatic carbon, f_{ar}^{B}: bridgehead aromatic carbon, f_{ar}^{S}: branched aromatic carbon, f_{ar}^{P}: oxy−aromatic carbon, and f_{a}^{C}: carbonyl/carboxyl carbon) (Qing Wang et al., 2018; Q. Wei & Tang, 2018) As shown in the ^{13}C−NMR analysis, with increasing thermal maturity, the aliphatic functional groups (0–90 ppm) exhibit a reduction trend in the relative amount of carbon, whereas the aromatic carbon groups (90–165 ppm) increase. This behavior is in an agreement with ^{1}H−NMR spectra in Figure 2 (left). The nonpolar alkyl carbons (0–51 ppm) generally diminish with the degree of maturity, except the aromatic methyl (f_{al}^{2}) group which could be reflected by the increase of aromatic carbon. In addition, the study infers that loss of oxygen at the early stages of maturation is due to a comparatively weak bond between oxygen–related carbon and kerogen backbone (Qian Wang et al., 2017).

2.2. XPS

Different types of organic carbon and oxygen forms were determined by analyzing the carbon (1s) peak. In each sample, four peaks located approximately at 285 eV, 286 eV, 287.5 eV, and 289 eV were determined after fitting the XPS carbon (1s) signal. The peak at 285 was attributed to both aromatic and aliphatic carbon. The amount of aromatic carbon was estimated using the XPS technique for $\prod$ to $\prod^*$ signal intensity as has been used previously (Kelemen et al., 1993). This confirms that the highly mature kerogen has an abundance of aromatic carbon structure as revealed in the solid−state ^{1}H & ^{13}C−NMR results. The peaks at 286 eV, 287.5 eV, and 289 eV originate from carbon atoms bound to one oxygen atom by a single bond (C−O), carbon atoms bound to one oxygen atom by double bonds (C=O), and carbon atoms bound to two oxygen atoms (O=C−O), respectively. In the most mature stage (sample D), the results show a relatively large amount of enrichment for oxygen−related carbon, whereas the rest of the samples (A−C) exhibit a comparatively similar amount of oxygen−related carbons in kerogen structure.

Organic nitrogen and sulfur information in kerogen structure was also obtained using XPS curve fitting methods, which at different energy positions are used to fit with the XPS N 1s and S 2p spectra, respectively. Nitrogen (1s) kerogen spectra were curve−resolved using four peaks at fixed energy positions of 397, 398.6, 399.4, 400.2, and 401.4 eV. Considering the organic sulfur (2p), the binding energy between 162−165.7 eV is assigned to pyrite, aliphatic and aromatic sulfur, and sulfoxide in XPS S 2p spectrum having $2p_{3/4}$ and S $2p_{1/2}$. The peaks at 168.0 (± 0.5) to 170.5 (± 0.5) eV can be indexed to S $2p_{3/4}$ and S $2p_{1/2}$ of SO_x (sulfate/sulfite/sulfone).

2.3 FTIR

The intensities, depicted in Figure 3, correspond to the asymmetric and symmetric stretching and bending of the C−H/C=O/C=C−C bonds about the central carbon atom on a relative basis in the spectra of kerogen samples. The reason for the overlapped original spectra is due to the same amount of energy, which is required for several vibrations. Therefore, IR structural evaluations have been established from acquired spectra documented in earlier studies (Rullkötter & Michaelis, 1990; Qing Wang et al., 2018) To find the intensities at desired frequencies, the FTIR spectrum area 1800−1500 cm^{-1} and 3200−2700 cm^{-1} was fitted by the Fourier self−deconvolution (Yao et

al., 2002); the coefficients of determination (R^2) of the peak fitting for the region in all spectra were found between 0.994−0.996.

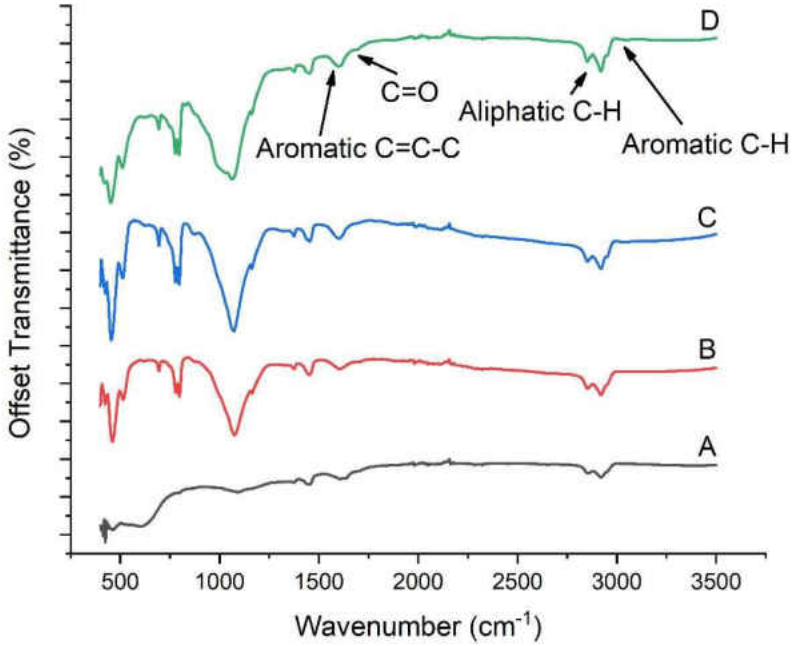

Figure 3. FTIR spectra of kerogens with increasing maturity exhibit the changes in the C−H stretch vibration area (2800−3200 cm^{-1}), aromatic C=C−C ring stretch vibration area (1615−1580 cm^{-1}), and Carbonyl/Carboxyl group vibration area (1650−1750 cm^{-1}).

Here, the study examined the C−H stretching band intensities for CH_3, CH_2, aromatic ring CH, aromatic ring C=C−C, and C=O based on the deconvolution results. Four indices (CH_3/CH_2 ratio, aromaticity, A−factor, and C−factor) were used to evaluate the structural characteristic of each different kerogen. The CH_3/CH_2 ratio [$I_{(2970–2950)}/I_{(2935–2915)}$] indicates the average chain length of aliphatic and the degree of chain branching. Aromaticity [$I_{(3130–3070)}/(I_{(2970–2950)}+I_{(2935–2915)})$] represents the degree of aromatic structure versus aliphatic chain structure. The A−factor [$I_{(2935–2915)}/(I_{(2935–2915)}+I_{(1615–1580)})$] and C−factor [$I_{(1750–1650)}/(I_{(1750–1650)}+I_{(1615–1580)})$] describe the relative amount of aliphatic carbon and oxygenated carbon to aromatic carbon, respectively (Qing Wang et al., 2018) and all indices are calculated through integrating the area under the curves. When the maturity increases, the CH_3/CH_2 ratio acquired demonstrates that the aliphatic chain length is comparatively shorter, and the branching is developed. Restated, highly mature kerogen

has more aromatic ring contribution and less methyl/methylene involvement with the expected increase in aromatic structure.

2.4 MALDI-TOF-MS

The ionization process in MALDI-TOF proceeds through the capture of a proton, which forms a charged adduct with the molecular species of the sample. As the number of charged adducts reflects the signal intensity of the molecular weight, a quantitative MWD analysis of any chemical compound is conducted. Four kerogen samples of this study were analyzed by MALDI-TOF to attribute maturation effects on the MWD of organic matter. Furthermore, systematic naturally matured kerogens with single biogenic origin have rarely been researched with MALDI-TOF, which limits the guidelines for an optimal and effective matrix selection based on the literature. Hence, in our study, kerogen samples were examined in both the presence and in the absence of the matrix (α-CHCA) for comparison and more accurate results.

(a) (b)

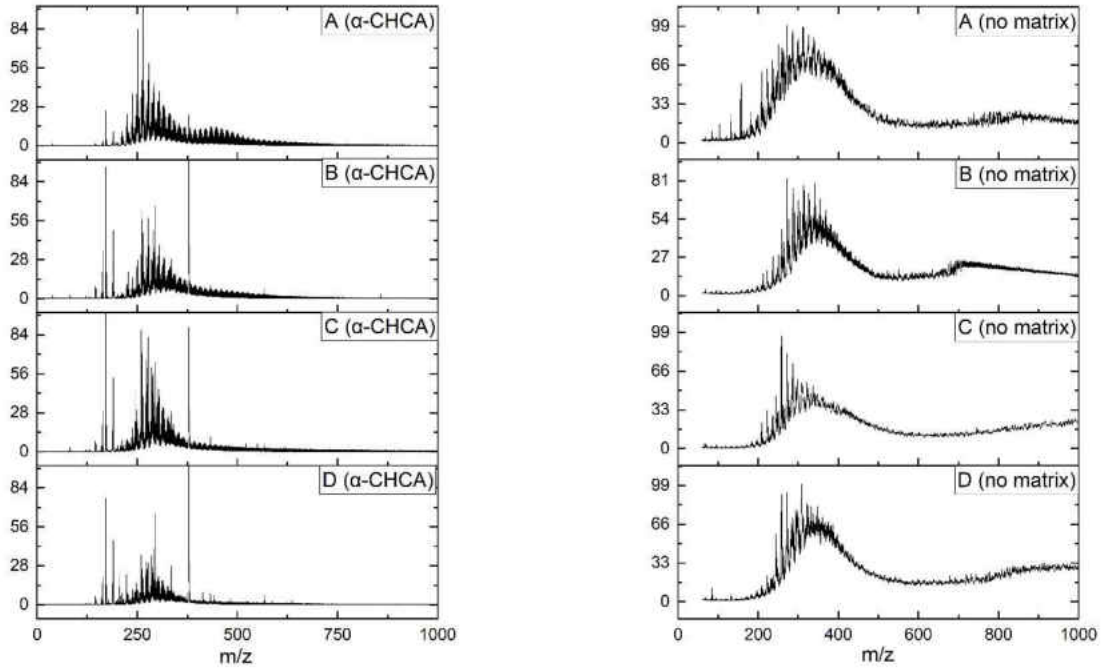

(c) (d)

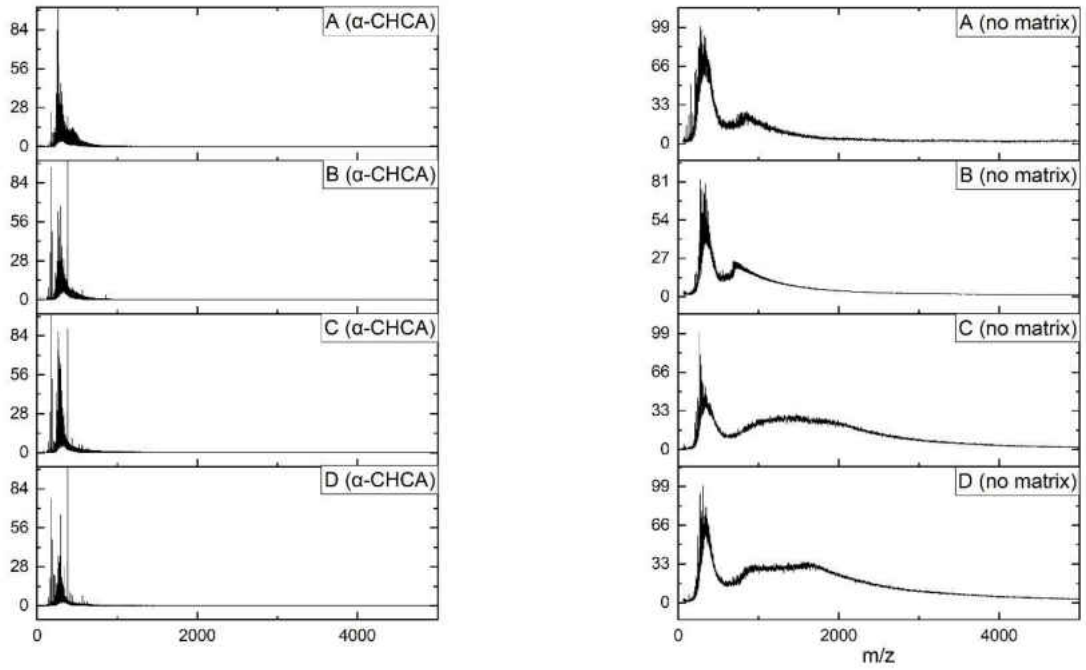

Figure 4. Normalized MALDI-TOF spectra of kerogens in the order of increasing maturity from A-D (a and c) in the presence of the matrix (α-CHCA) and (b and d) in the absence of the matrix. The spectra are plotted over (a and b) a range of 60 to 1000 Da and (c and d) a range of 60 to 5000 Da.

Figure 4 exhibits the mass spectra of kerogen samples obtained both in the presence and in the absence of the matrix. In all of these spectra for the presence of the matrix, unidentified high-intensity signals were observed in the relatively low-mass region between 200 and 400 m/z. Also, the study could not find a regular ionization and pattern overall. This confirms that kerogen does not have a specific chemical structure and contains various functional groups which are differently ionized, which hinders the signal interpretation from analyzing molecules in kerogen. Also, overall spectra representing the samples in Figure 4 do not show a particular relationship with signal intensities unlike polymers and proteins. However, signal intensity changes were found with respect to the degree of thermal maturation. As a result of this alteration in the intensity, it is conclusive that the maturation process would change the molecular structure of kerogen in terms of the molecular mass of the organic matter. This infers that the chemical structure of kerogen has been evolved while bond-breaking and forming have occurred (Takeda & Asakawa, 1988). Thus,

the study can at least conclude that MALDI result confirms the chemical structure changes by maturation. Sample A, the immature kerogen, exhibits signals between 250 to 350 m/z with the highest intensity regardless of the presence or absence of the matrix. In addition, when the maturation is progressed, strong signals become evident in the presence of the matrix, near 170 m/z and 370 m/z.

3. Discussion

3.1. Carbon Structural Changes

(a)

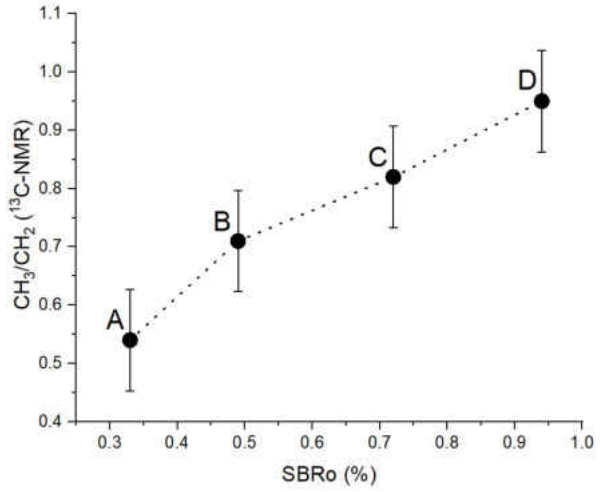

(b)

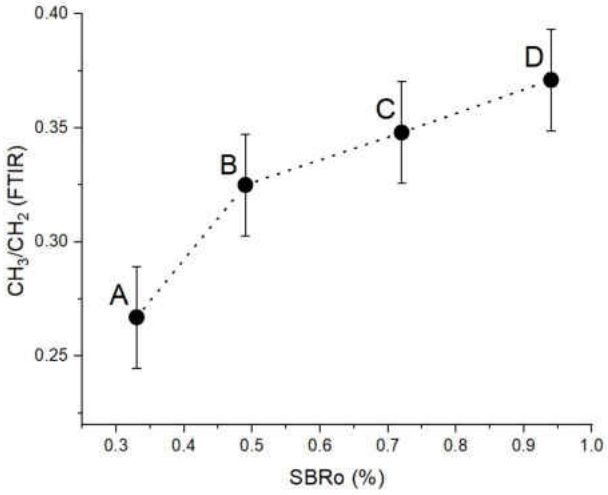

(c)

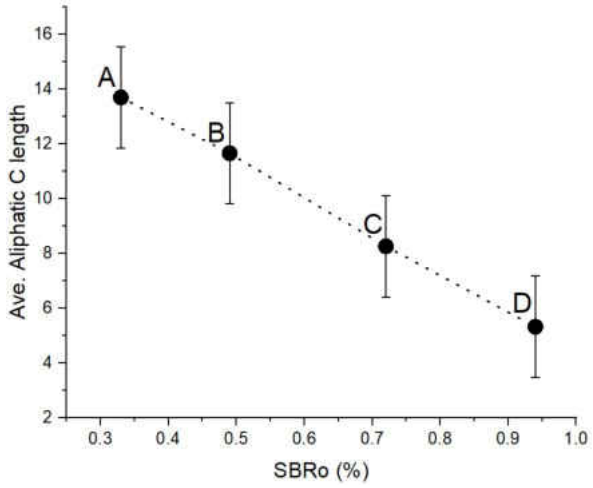

(d)

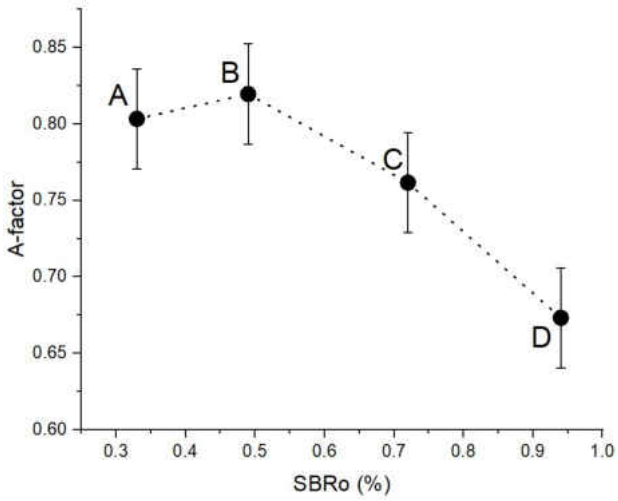

Figure 5. The aliphatic carbon structure changes by thermal maturity. The ratio of methyl/methylene is estimated from (a) $^{13}C-NMR$ [$(f_{al}^{1} + f_{al}^{2})/ f_{al}^{H1}$] and (b) FTIR [$I_{(2970-2950)}/I_{(2935-2915)}$] results. (c) Average aliphatic carbon chain length by $^{13}C-NMR$ [$(f_{al}^{1} + f_{al}^{2} + f_{al}^{H1} + f_{al}^{H2} + f_{al}^{O1} + f_{al}^{O2}) / f_{ar}^{S}$]. (d) A−factor by FTIR [$I_{(2935-2915)}/(I_{(2935-2915)}+I_{(1615-1580)})$]. Error bars represent standard errors.

The ratios of CH_3/CH_2 from $^{13}C-NMR$ have a similar order of increase to those obtained from the FTIR analysis when the maturity increases (Figures 5a−b), which is consistent with the previously described data from type II kerogen structure (Craddock et al., 2018). This growth of CH_3/CH_2 ratio could be evidence of chain cleavage coupled with hydrocarbon generation. While kerogen maturation occurs naturally, the molecular structure of this macromolecule evolves through bond−breaking and bond−forming, under changing physical conditions (temperature, pressure, and time) of the subsurface (Durand, 1980; Takeda & Asakawa, 1988). In terms of carbon to carbon (C−C) bond in the kerogen structure, bond−dissociation energy (BDE) between α and β carbon is weaker than one between α and aromatic carbon (Manka et al., 1985; Yao et al., 2002). Also, short branching carbon (such as methyl) to carbon in the backbone structure has less BDE than longer chain carbon (Lin & Patrick Ritz, 1993). It appears that kerogen samples of the Bakken shale play also follow this mechanism which indicates a higher ratio of CH_3/CH_2 during thermal maturation as shown in Figures 5a−b. In addition to the ratio of CH_3/CH_2, the average aliphatic carbon length and the amount of aromatic carbon follows this trend too. Figure 5c explains that the average length of aliphatic carbon reduces as the maturity increases, indicating that thermal maturation accompanies the structural changes in kerogen with both shorter aliphatic chain and a higher ratio of CH_3/CH_2, as delineated by FTIR and $^{13}C-NMR$.

(a) (b)

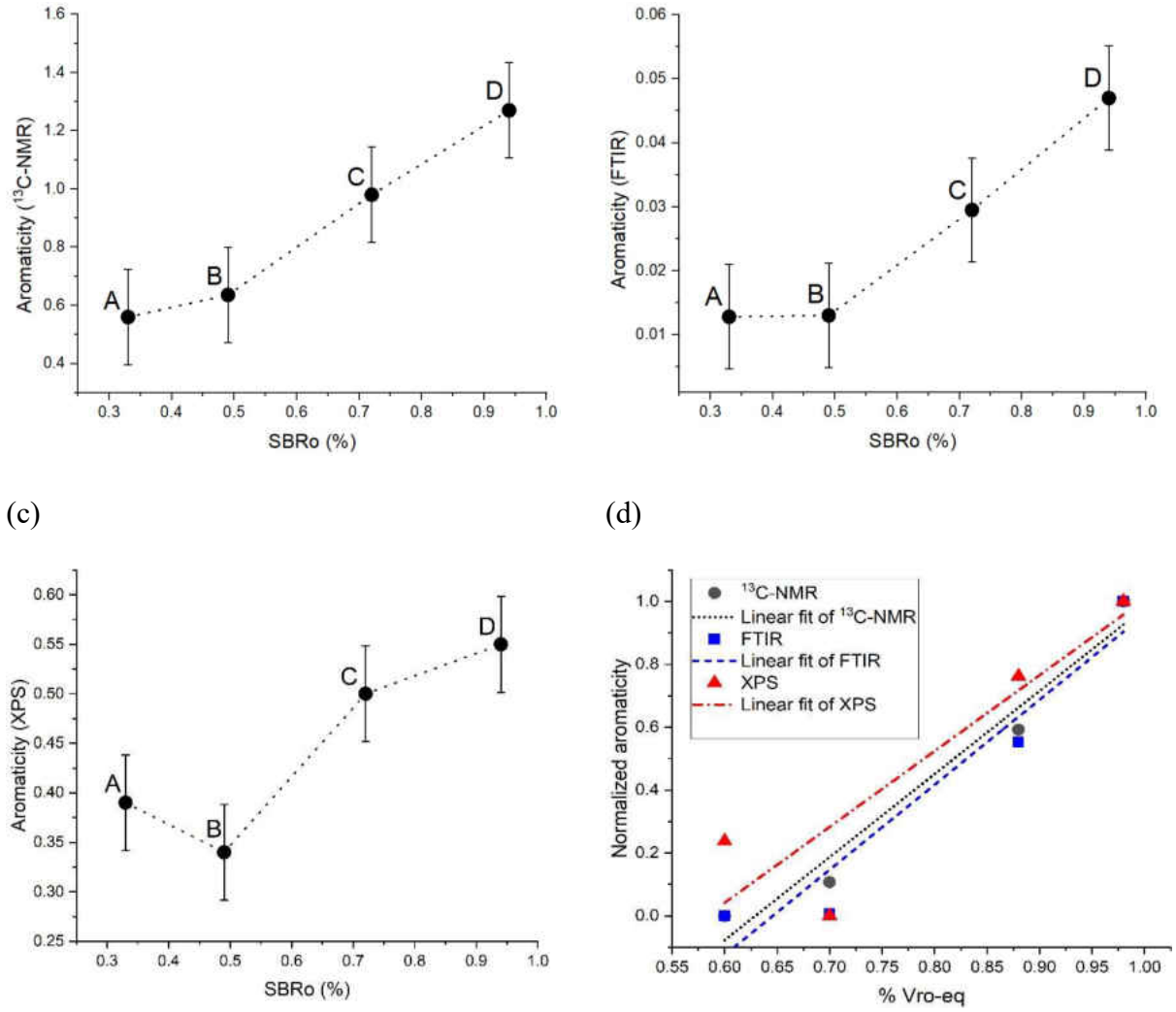

Figure 6. The aromatic carbon structural changes by thermal maturity. The aromaticity (aromatic carbon/aliphatic carbon) was calculated from (a) ^{13}C−NMR [$f_{ar}^{H} + f_{ar}^{B} + f_{ar}^{S} + f_{ar}^{P}$], (b) FTIR [$I_{(3130-3070)}/(I_{(2970-2950)}+I_{(2935-2915)})$], and (c) XPS [mole % aromatic carbon]. (d) Comparison of aromaticity slop trends (linearly fitted). Error bars represent standard errors.

Figure 6 depicts the aromatic carbon as investigated by three different analytical methods, ^{13}C−NMR, FTIR, and XPS. Figures 6a−c verifies our finding that higher maturity kerogen overall tends to have more amount of aromatic carbon. This is also compatible with the ^{1}H−NMR result, which infers to the ratio of aliphatic protons to the aromatic ring compared to the rest of protons. With an increase of maturity (sample A to D), the spectrum becomes sharper and has diminished intensity in the range of the aliphatic protons between 0.5 to 4.3 ppm, which represents the abundance of aromatic structure. This observation is collectively acceptable excluding sample B

with the amount of aromatic carbon of XPS being comparatively 13% lower than the one of $^{13}C-NMR$.

FTIR results also propose that the aromaticity value of sample B is similar to sample A, which is different than the overall observed trend. This latest outcome can support lower A-factor values for Sample B compared to Sample A, as seen in Figure 5d. In addition, the degree of aromaticity (Figure 6d) estimated from three techniques ($^{13}C-NMR$, FTIR, and XPS) strongly confirms that the aromaticity is increasing. Notably, the study found that based on the aromaticity results there is relatively a considerable rift between pre−oil and oil window stage samples. Following the oil window stage, the amount of aromatic carbon fairly increases, as well as the rate of change in aromaticity as seen by the slope of the curve which is found higher through advancing thermal maturity in the oil generation window.

3.2 Heteroatoms

The loss of oxygen functional groups drives early structural changes. Because the oxygen−related carbon bonds have relatively weak BDE, the carboxyl and carbonyl groups can be easily defunctionalized (Craddock et al., 2018; Salmon et al., 2009). In our study, the results revealed that kerogen maturation involves relatively bulky oxygen−related carbon reduction at the early stage of maturation (pre−oil window) then it increases in oil window stage, which is verified by $^{13}C-NMR$ and XPS.

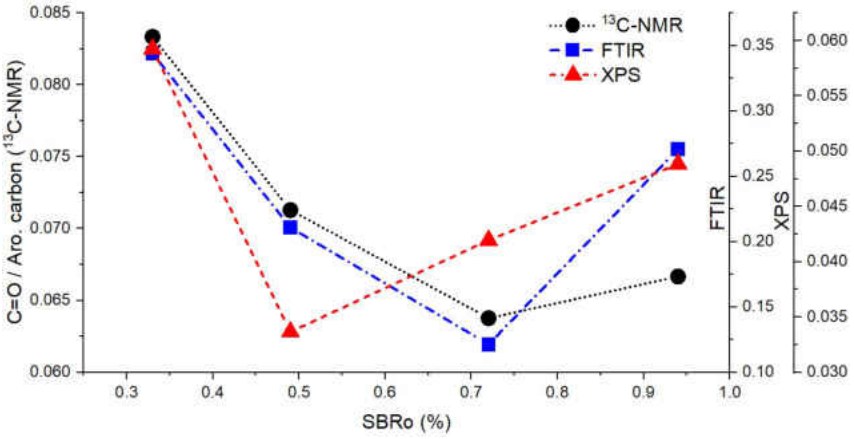

Figure 7. The ratios of C=O/aromatic carbon were estimated from ^{13}C−NMR, FTIR, and XPS results, which were calculated by $f_a^C/(f_{ar}^H + f_{ar}^B + f_{ar}^S + f_{ar}^P)$, C−factor $[I_{(1650-1750)}/(I_{(1650-1750)}+I_{(1615-1580)})]$, and [(mole % of total oxygen) × (C=O and C−O=O fraction)/(mole % of aromatic carbon)], respectively.

The changes in the ratios of C=O/aromatic carbon were investigated by three methods (^{13}C−NMR, FTIR, and XPS) depicted in Figure 6. Because it is difficult to analyze the organic oxygen group from ^{13}C−NMR (R. Kelemen et al., 2007), the comparison of the three methods is presented in the same graph to help us better understand and verify the results. As thermal maturity increases, first, the ratio of C=O/aromatic carbon decreases regardless of the method, along with the ratio of carbonyl/carboxyl functional groups to aromatic carbon which also was found to reduce at the early stages of maturation. Then, in the oil−window stage (sample C−D), the ratio of C=O/aromatic carbon starts to rise showing that the amount of oxygen estimated in sample D to become higher than sample C. Although most oxygen−containing functional groups will be expelled from the organic matter during the initial stages of thermal maturation, the results exhibit an unexpected increase in the oxygen content of the functional groups in the higher maturity ranges of kerogen. This can be explained by the enrichment of oxygen through the addition of oxygen from inorganic mineral or water (interstitial water) impurities as thermal maturity increases which are also observed in other studies (Craddock et al., 2018; Michels et al., 1996). It's also expected that the formation of insoluble pyro−bitumen, which is highly oxidized as thermal maturity advances, may lead to an unexpected increase of C=O/aromatic carbon ratio in higher thermal maturation (Lis et al., 2005).

3.3 Molecular Weight

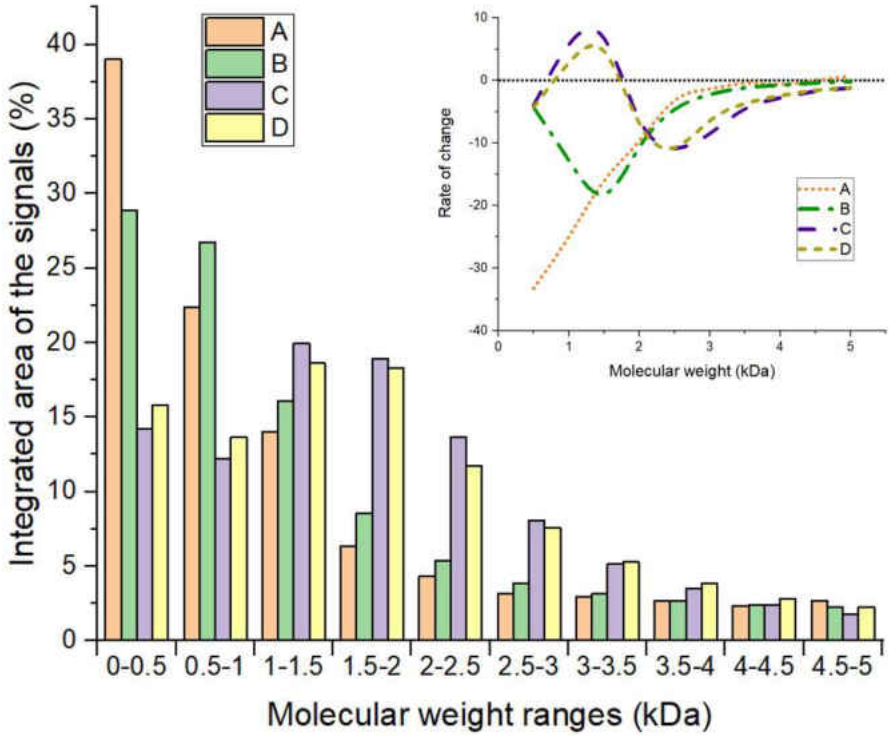

Figure 8. Molecular weight distribution (MWD) diagram of four samples presents different molecular weight ranges at different thermal maturity stages in the absence of the matrix. The relative areas of each sample are compared within the designated intervals. This specific MWD and intervals are used since this particular format showed the most distinct variation in MWs. The smaller image is based on MWD, rate of change (derivatives) of integrated MALDI-TOF signals with respect to molecular weight over the interval 0 to 5 kDa.

Figure 8 exhibits four molecular weight distribution (MWD) diagrams in separate intervals obtained from immature to late mature organic matters. Each independent value of four samples was created through the summation of the area under molecular weight signals based on the normalized spectra (Figure 4). Furthermore, this particular partitioning (distribution) of MWs is decided through trying different molecular weight intervals and plotting MWDs of these four different samples when the most distinct and meaningful trends are delineated. The study also notes that the quantitative value in Figure 8 disregards total MW and solely pertains to the comparative change of MWD regarding the maturity since the area ratio was adopted. It was found that, for relatively immature kerogen (A and B), around 60% of the signals are under 1 kDa range, whereas the majority of recorded signals for relatively higher maturity kerogen samples (C and D)

are found between 1 to 2 kDa range. Immature sample (A) has the highest signal in the range under 500 Da; this indicates that relatively lighter molecular structures exist in kerogen compound prior to maturation. Meanwhile, the MWD for samples A and B continuously decreases in higher mass ranges. Remarkably, as the degree of the maturation increases, the higher signal distribution in the heavier range is observed in Figure 8.

Additionally, the rate of change in MW is also investigated for each maturity stage over the entire range from 0 to 5 kDa. The smaller graph in Figure 8 is obtained through taking the derivatives of the integral of MALDI-TOF spectra to represent the rate of change in the quantity of that specific MW interval for each sample. The most important aspect of this graph is that at a specific MW (around 2.5 kDa) all of four samples start to show relatively similar increasing trends in the rate of MW quantities, and then this becomes constant regardless of their maturity at higher MW region (> 4 kDa). The difference in MWD and rate of change in MWs between the immature (A and B) and late mature (C and D) kerogens could refer to the boundary from pre-oil to oil generation window and to the phenomenon where hydrocarbons are generated and expelled from the OM through a nonlinear trend (Abarghani et al., 2019). This major change in molecular structure corresponds to the onset of oil-window, when a major alteration is expected to take place (molecular structure and molecular weight) around 2.5 kDa where all MW rate of change graphs in the smaller image in Figure 8 coincide and start to perform with a similar increasing trend.

CHAPTER 3. COMPUTATIONAL MOLECULAR MODELLING AND SIMULATIONS

1. Kerogen Model

The molecular models of the Bakken kerogen were obtained from computational simulations in accordance with experimental analysis obtained from geochemistry screening by Rock-Eval pyrolysis (T. Wang et al., 2018), ^{13}C nuclear magnetic resonance (NMR) spectroscopy, X-ray photon spectroscopy (XPS) and gas adsorption isotherms (Liu et al., 2017; R. Kelemen et al., 2007) The organic matter structures were modeled based on type II kerogen (representative of the Bakken) in the pre-oil window (immature) and were mainly composed of carbon and hydrogen with nitrogen, oxygen, and sulfur atoms as attachments (Fig. 9).

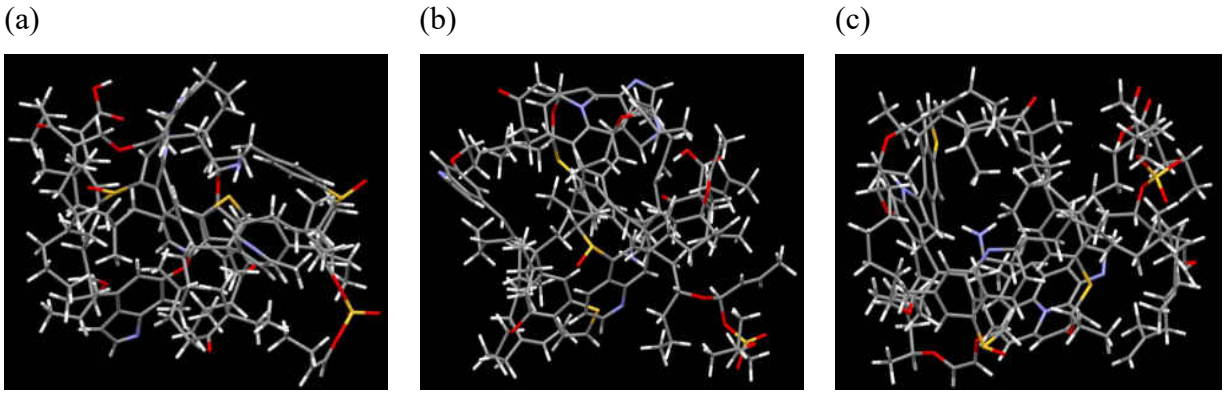

Figure 9. Constructed and optimized Bakken kerogen model A (a), model B (b), and model C (c). Different geometric configuration and chemical compositions with the following color code, carbon: black; hydrogen: white; oxygen: red; sulfur: yellow and nitrogen: blue. (a) $C_{141}H_{187}N_6O_{15}S_4$, *(b)* $C_{152}H_{193}N_6O_{15}S_4$, *and (c)* $C_{158}H_{207}N_6O_{16}S_4$.

The structures of these three Bakken kerogen models (Models A, B, and C) are a complicated mixture of chain and mesh. Each model owns a different chemical composition and topology, $C_{140}H_{176}N_6O_{15}S_4$, $C_{151}H_{179}N_6O_{15}S_4$, and $C_{158}H_{188}N_6O_{16}S_4$, respectively. The structures contain disordered pores with the radius ~3−7 Å while the calculated densities of Models A, B, and C are around 1.1, 1.2, and 1.3 gcm^{3-}, respectively. These models have been already shown to reproduce the experimental adsorption isotherms for CO_2 and N_2 uptake at low pressure and correctly assign Bakken kerogen as a selective CO_2 absorbent in the presence of N_2 (Liu et al., 2017).

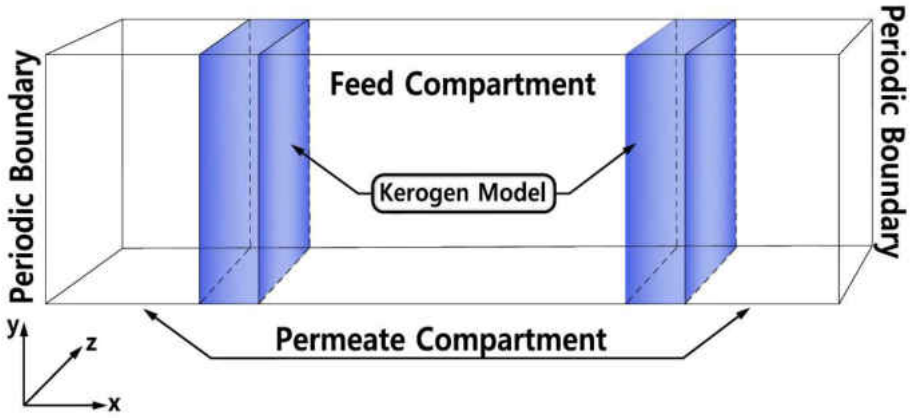

Figure 10. Schematic illustration of alternating Feed/Permeate compartment; molecular kerogen model is collected and tethered into one gas diffusion/separation system.

The study collected and tethered all three molecular models into one gas diffusion/separation system to avoid a biased outcome from our simulation results. Packmol package was utilized to place one of each kerogen models (Models A, B, and C) in a feed compartment, as shown in Fig. 10. These two systems were then allowed to come to relaxation by running NVT molecular dynamics simulations. Since the three kerogen models were simply adhered to one another and clustered, packing them in different modes was not considered. In this system, gaseous fluids in feed compartment would diffuse to two different surfaces of kerogen, to the left and right models in Fig. 10. The details of all parameters which attribute to chemical composition and carbon-based structure of these molecules are described in Table 3. The kerogen model in this system is composed of inner and outer pores, which is a disordered molecular structure and includes functional groups.

Table 3. Average of carbon structural parameters for the Bakken kerogen models (combination of model A, B, and C).

Structure	Kerogen model (Combined)
Aromatic	35
Carboxyl/Amide/Carbonyl	2.6
Protonated aromatic	17
Phenoxy/Phenolic	2.1
Alkyl-substituted aromatic	6.6

Bridged aromatic	9.2
Aliphatic	62
Methylene/Methine	32
Methyl/Methoxy	12
Alcohol/ether	4.1

Note: the data presented here are ratio per 100 number of carbon.

2. Molecular dynamics Simulation Setup

Simulation of molecular transport utilizes a system setup that is developed by others on an osmosis/reverse osmosis system (Murad & Lin, 2001). The simulation system for studying gas separation/diffusion based on our kerogen model can be found in Fig. 10. Two identical kerogen models are used along with periodic boundary conditions to create alternating fluid compartments in the x-direction, while the system is infinite in the transverse dimensions (y,z) (Fig. 10). Kerogen atoms are tethered to their known equilibrium positions using a simple harmonic tether. The region between the two kerogen models (feed compartment) was filled with the fluid to be separated at the desired conditions. Initially empty left and right permeate compartments were set up to provide the driving force while periodic boundary conditions would allow a continuous compartment. Long-range site−site interactions are modeled using Lennard-Jones (LJ) and Coulombic potentials as following:

$$E_{total} = \sum_{i<j} 4\varepsilon \left[\left(\frac{\sigma_{ij}}{r_{ij}}\right)^{12} - \left(\frac{\sigma_{ij}}{r_{ij}}\right)^{6} \right] + \sum_{i<j} \frac{Cq_i q_j}{\varepsilon R_{ij}} \quad , r_{ij} < r_c \qquad (1)$$

where r_{ij} is the distance between sites i and j, r_C is the cutoff radius beyond which the short-range interactions are neglected, σ_{ij} and ε are the L-J parameters, q_i and q_j represent the charges on sites i and j, and C is a unit conversion constant. These potentials are summed over all sites to obtain the total intermolecular interactions.

To carry out molecular dynamics simulation on the mixture fluid (CO_2, CH_4, H_2O, Na^{1+}, and Cl^{1-}), the harmonic potential was employed between the model and gas molecules, along with the site to site non-bonding interaction potential. Transportation of fluid particles within the kerogen models was investigated using molecular dynamics simulations at a practical temperature and pressures

relevant to the Bakken Formation (T = 333 to 393 K and P = 1 to 30 Bar) (Gosnold, W. and McDonald, M.R. and Klenner, Robert and Merriam, 2012). Water was modeled under a simple point charge (SPC) (Berendsen et al., 1981), while CO_2 is modeled using the flexible force field developed by Cygan et al.(Cygan et al., 2012), CH_4 is represented by the TraPPE force field and Na^{1+} and Cl^{1-} ions are modeled using the parameters proposed by Smith and Dang (G. Martin & Ilja Siepmann, 1998; Smith & Dang, 1994) The parameters and charges used in this study are summarized in Table 4.

Table 4. Parameters related to the adsorbates (CH_4, CO_2, and Brine).

Molecules	Atoms/Ions	Charge	σ(Å)	ε (Kcal/mol)
CH_4	C	0.00	3.73	0.2941
H_2O	O	-0.82	3.17	0.1554
	H	0.41	0.0	0.0
CO_2	C	0.65	2.80	0.0559
	O	-0.325	3.028	0.1597
Salt	Na^{1+}	1.00	2.35	0.13
	Cl^{1-}	-1.00	4.40	0.10

Initial configurations were created using Packmol to construct non-overlapping random fluid initial configurations.[31] All equilibrium simulations (EMD) of the systems considered here, were carried out by molecular dynamics of gas adsorption processes using "osmosis and reverse osmosis" technique with LAMMPS simulation package (Murad & Lin, 2001; Plimpton, 1995) The particle−particle/particle−mesh (PPPM) technique was used in the treatment of long-range Coulombic interactions beyond the cutoff radius of 1.4 nm (Brown et al., 2012).

All simulation cells are parallel to the kerogen/mixture fluid interface, and periodic boundary conditions are employed in all of the three dimensions. The system size is sufficiently large to ensure that finite-size effects are negligible in our 1 ns equilibration simulations that are performed in the NPT ensemble, where the volume variations are achieved by changing the box length only in the x-direction. Then, NVT ensemble equilibrium molecular dynamics simulations were performed, in which the temperature of the system is kept at a fixed value by a Gaussian thermostat. All simulations were carried out at three different temperatures, 333K, 363K, and 393K, which are

typical temperatures for the Bakken formation (Gosnold, W. and McDonald, M.R. and Klenner, Robert and Merriam, 2012).

3. Molecular dynamics Result and Discussion

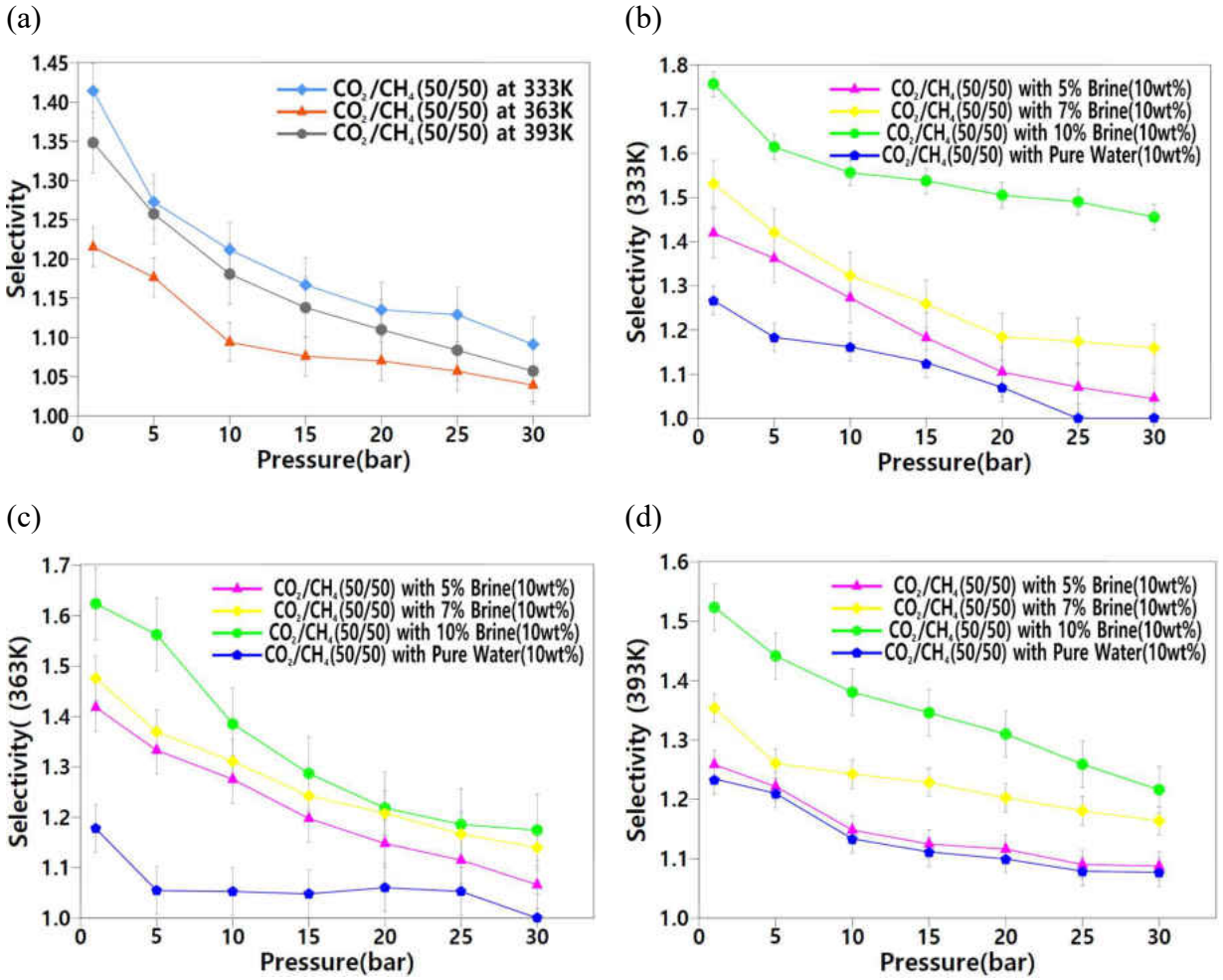

Figure 11. (a) Estimated CO_2/CH_4 selectivity for the binary mixture (CO_2/CH_4:50/50 mol%) on the kerogen model. Estimated CO_2/CH_4 selectivity for the mixture of CO_2/CH_4/Brine on the kerogen model at (b) 333K, (c) 363K, and (d) 393K. In panels b-d, the comparative concentration of $CO_2/CH_4/H_2O$/NaCl in solutions of 5%, 7%, and 10% brine is 42.3/42.3/15.2/0.2 mol%, 42.3/42.3/15.1/0.4 mol%, and 42.5/42.5/14.5/0.5 mol%, respectively. Error bars are shown at certain pressure steps.

Fig. 11 displays CO_2/CH_4 selectivity of the Bakken kerogen in the presence of 5%, 7%, and 10% brine concentrations at different system temperatures. The motivation of this study was to

investigate the possibility of a successful CO_2 EOR and sequestration operation from the molecular point of view in the Bakken at different concentrations of brine, since it varies regionally in the Williston Basin where this rock unit is extended in the subsurface. Considering this important factor, the concentration of brine was broadly selected to particularly explain the effects of brine on such operation, i.e. a range of 3 to 10% of brine concentration in the mixture with 10 wt% of the whole mixture. The very notable result is that when the gas mixture contains a higher concentration of brine, kerogen demonstrates a much higher CO_2/CH_4 selectivity over the entire pressure range (1 to 30 bar).

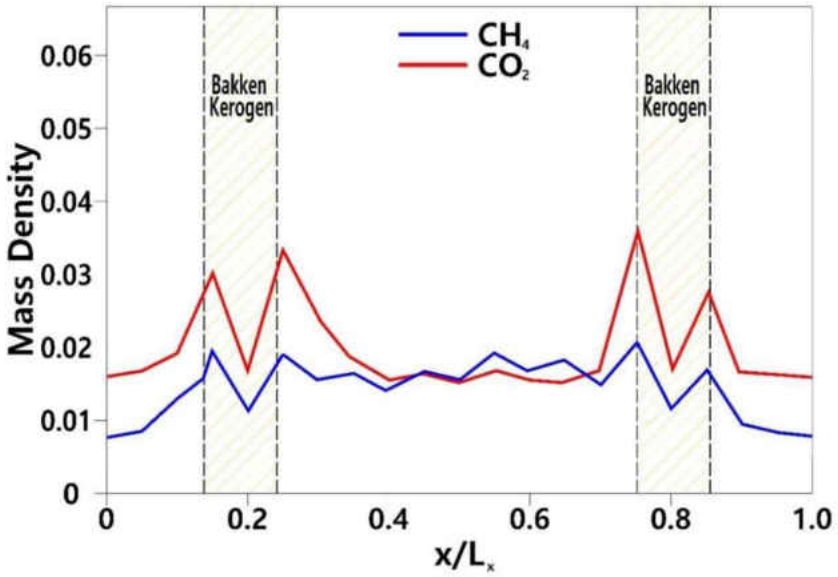

Figure 12. Density mass profile for CO_2 and CH_4 molecules with 10 wt% brine at 333K in a steady-state simulation, and an initial solution concentration of 42.5 CO_2/42.5 CH_4/14.5 H_2O/0.5 NaCl mol%. L_x is the system dimension perpendicular to the kerogen model.

It was found that when CO_2 containing mixtures diffuse in the system, Fig. 12, the interaction between the kerogen model and each molecule would vary. Considering the competitive diffusion of CO_2 and CH_4 in the system, CO_2 molecules are mainly observed to place on the surface region of the model, while CH_4 molecules are detected on both the bulk and the surface of the model due to weaker interactions with the kerogen molecule and functional groups. CO_2 molecules express

higher interactions with kerogen pore surfaces than CH_4 and water molecules, thus occupying available space and sites on the kerogen surface. Based on these results, the injection of CO_2 in the Bakken can provide us with the desired outcome to satisfy a successful and economical carbon capture and EOR operation simultaneously.

CHAPTER 4. CONCLUSIONS

1. Structural Characterization of Organic Compounds in Shale Play Bakken

These studies show how hydrocarbon generation can impose changes in the source rock organic compound structure during the maturation process. The analysis of extracted kerogen through spectroscopic techniques (^{1}H & ^{13}C−NMR, XPS, FTIR, and MALDI-TOF) was used to determine chemical contents and molecular structures as maturation advances. This study will enable us to better model separation and capture processes in shale play via theoretical methods. Based on the results the following conclusions can be made:

- The structural changes of kerogen pertaining to the abundance of the aromatic and aliphatic chain length correlate well with the maturity of kerogen. Based on the aliphatic carbon chain that is detected in kerogen structure by ^{1}H & ^{13}C−NMR and FTIR, the ratio of CH_3/CH_2 increases when the maturity increases accompanied with the shorter aliphatic chain length.
- In contrast to aliphatic carbon, the aromatic carbon structure becomes more abundant in higher maturity and oil window stage. All three techniques (^{13}C−NMR, XPS, and FTIR) confirms an increasing trend similar to aromaticity with the same rate of changes. Also, a considerable discrepancy between pre−oil window and oil window stage regarding aromaticity was observed.
- The MWD variation provided different molecular weight ranges at different thermal maturity stages in the absence of the matrix. Relatively immature kerogens exhibited around 60% of the signals under 1 kDa range, with the strongest signals in the range under 500 Da, whereas the majority of signals of mature kerogens were found between 1 to 2 kDa range.
- The shorter aliphatic chain length and abundant aromatic structure are expected and delineated based on FTIR structural indices (CH_3/CH_2 and Aromaticity) when the degree of maturity increases which was correlated to the MWDs. The structural kerogen alteration in the abundance of the aromatic and shorten aliphatic chain length as its maturity progress tends to make the weight of molecules/fragments in kerogen heavier.

2. Computational Molecular Modelling and Simulation

The studies report a molecular model for amorphous organic matter (kerogen) built based on experimental constraints. GCMC and MD simulations were run to compute gas adsorption isotherms on the model and were compared to our experimental results. We have demonstrated that electrostatic and van der Waals interactions between the disordered surface of the kerogen and different gases govern the separation process. The provided insights into the thermodynamics and kinetics of the adsorption selectivity phenomenon in this work could be useful to design a more effective CO_2 separation and capture process in kerogen. Based on the results the following conclusions can be made:

- Adsorption of CO_2 molecules on a clustered model also shows similar adsorption isotherm behavior overall. Based on the simulation results the study uncovered, the kerogen model seems to have a stronger interaction with CO_2 molecules than N_2 molecules such that CO_2 molecules are not only adsorbed on the surface but also penetrate to the sub-surface level of the model.

- Higher CO_2/CH_4 selectivity happens when the gas mixture contains a higher concentration of brine at a given temperature and pressure. When the mixture contains pure water, CO_2/CH_4 selectivity will become less than a dry system.

- Brine and its concentration seem to have a significant impact on the CO_2/CH_4 selectivity at different temperature and pressure, and can be the main controlling factor for a successful carbon dioxide capture and EOR operation in an unconventional organic-rich shale.

REFERENCES

Abarghani, A., Ostadhassan, M., Gentzis, T., Carvajal-Ortiz, H., & Bubach, B. (2018). Organofacies study of the Bakken source rock in North Dakota, USA, based on organic petrology and geochemistry. *International Journal of Coal Geology*, *188*, 79–93. https://doi.org/10.1016/J.COAL.2018.02.004

Abarghani, A., Ostadhassan, M., Gentzis, T., Carvajal-Ortiz, H., Ocubalidet, S., Bubach, B., Mann, M., & Hou, X. (2019). Correlating Rock-Eval™ Tmax with bitumen reflectance from organic petrology in the Bakken Formation. *International Journal of Coal Geology*, *205*, 87–104. https://doi.org/10.1016/j.coal.2019.03.003

Alvarado, V., & Manrique, E. (2010). Enhanced Oil Recovery: An Update Review. *Energies*, *3*(9), 1529–1575. https://doi.org/10.3390/en3091529

Beavis, R. C., Chaudhary, T., & Chait, B. T. (1992). α-Cyano-4-hydroxycinnamic acid as a matrix for matrixassisted laser desorption mass spectromtry. *Organic Mass Spectrometry*, *27*(2), 156–158. https://doi.org/10.1002/oms.1210270217

Berendsen, H. J. C., Postma, J. P. M., van Gunsteren, W. F., & Hermans, J. (1981). *Interaction Models for Water in Relation to Protein Hydration* (pp. 331–342). https://doi.org/10.1007/978-94-015-7658-1_21

Bousige, C., Ghimbeu, C. M., Vix-Guterl, C., Pomerantz, A. E., Suleimenova, A., Vaughan, G., Garbarino, G., Feygenson, M., Wildgruber, C., Ulm, F.-J., Pellenq, R. J.-M., & Coasne, B. (2016). Realistic molecular model of kerogen's nanostructure. *Nature Materials*, *15*(5), 576–582. https://doi.org/10.1038/nmat4541

Brown, W. M., Kohlmeyer, A., Plimpton, S. J., & Tharrington, A. N. (2012). Implementing molecular dynamics on hybrid high performance computers – Particle–particle particle-mesh. *Computer Physics Communications*, *183*(3), 449–459. https://doi.org/10.1016/J.CPC.2011.10.012

Chen, Y., Zou, C., Mastalerz, M., Hu, S., Gasaway, C., & Tao, X. (2015). Applications of Micro-Fourier Transform Infrared Spectroscopy (FTIR) in the Geological Sciences—A Review.

International Journal of Molecular Sciences, *16*(12), 30223–30250. https://doi.org/10.3390/ijms161226227

Clough, A., Sigle, J. L., Jacobi, D., Sheremata, J., & White, J. L. (2015). Characterization of Kerogen and Source Rock Maturation Using Solid-State NMR Spectroscopy. *Energy & Fuels*, *29*(10), 6370–6382. https://doi.org/10.1021/acs.energyfuels.5b01669

Coates, J. (2006). Interpretation of Infrared Spectra, A Practical Approach. In *Encyclopedia of Analytical Chemistry*. John Wiley & Sons, Ltd. https://doi.org/10.1002/9780470027318.a5606

Craddock, P. R., Bake, K. D., & Pomerantz, A. E. (2018). Chemical, Molecular, and Microstructural Evolution of Kerogen during Thermal Maturation: Case Study from the Woodford Shale of Oklahoma. *Energy & Fuels*, *32*(4), 4859–4872. https://doi.org/10.1021/acs.energyfuels.8b00189

Cygan, R. T., Romanov, V. N., & Myshakin, E. M. (2012). Molecular Simulation of Carbon Dioxide Capture by Montmorillonite Using an Accurate and Flexible Force Field. *The Journal of Physical Chemistry C*, *116*(24), 13079–13091. https://doi.org/10.1021/jp3007574

Durand, B. (1980). *Sedimentary Organic Matter and Kerogen. Definition and Quantitative Importance of Kerogen. Kerogen, Insoluble Organic Matter from Sedimentary Rock*. Editions technips.

Edwards, R. W. J., Celia, M. A., Bandilla, K. W., Doster, F., & Kanno, C. M. (2015). A Model To Estimate Carbon Dioxide Injectivity and Storage Capacity for Geological Sequestration in Shale Gas Wells. *Environmental Science & Technology*, *49*(15), 9222–9229. https://doi.org/10.1021/acs.est.5b01982

Fakcharoenphol, P., Kurtoglu, B., Kazemi, H., Charoenwongsa, S., & Wu, Y.-S. (2014, April 1). The Effect of Osmotic Pressure on Improve Oil Recovery from Fractured Shale Formations. *SPE Unconventional Resources Conference*. https://doi.org/10.2118/168998-MS

G. Martin, M., & Ilja Siepmann, J. (1998). Transferable Potentials for Phase Equilibria. 1. United-Atom Description of n-Alkanes. *The Journal of Physical Chemistry B*, *102*(14), 2569–2577. https://doi.org/10.1021/jp972543+

Gosnold, W. and McDonald, M.R. and Klenner, Robert and Merriam, D. (2012). Thermostratigraphy of the Williston Basin. *Transactions - Geothermal Resources Council*, *36*, 663–670.

Jia, B., Tsau, J.-S., & Barati, R. (2019). A review of the current progress of CO2 injection EOR and carbon storage in shale oil reservoirs. *Fuel*, *236*, 404–427. https://doi.org/10.1016/J.FUEL.2018.08.103

Jin, L., Hawthorne, S., Sorensen, J., Pekot, L., Kurz, B., Smith, S., Heebink, L., Herdegen, V., Bosshart, N., Torres, J., Dalkhaa, C., Peterson, K., Gorecki, C., Steadman, E., & Harju, J. (2017). Advancing CO2 enhanced oil recovery and storage in unconventional oil play—Experimental studies on Bakken shales. *Applied Energy*, *208*, 171–183. https://doi.org/10.1016/j.apenergy.2017.10.054

Kelemen, S. R., Rose, K. D., & Kwiatek, P. J. (1993). Carbon aromaticity based on XPS II to II□ signal intensity. *Applied Surface Science*, *64*(2), 167–174. https://doi.org/10.1016/0169-4332(93)90276-H

Khatabi, S., & Aghajanpour, A. (2018). Raman spectroscopy: an analytical tool for evaluating organic matter. *Journal of Oil, Gas and Petrochemical Sciences*, *1*(1), 28–33. https://doi.org/10.30881/jogps.00007

Khatibi, S., Ostadhassan, M., Tuschel, D., Gentzis, T., Bubach, B., & Carvajal-Ortiz, H. (2018). Raman spectroscopy to study thermal maturity and elastic modulus of kerogen. *International Journal of Coal Geology*, *185*, 103–118. https://doi.org/10.1016/j.coal.2017.11.008

Lee, H., A. Shakib, F., Shokouhimehr, M., Bubach, B., Kong, L., & Ostadhassan, M. (2019). Optimal Separation of CO2/CH4/Brine with Amorphous Kerogen: A Thermodynamics and Kinetics Study. *The Journal of Physical Chemistry C*, *123*(34), 20877–20883. https://doi.org/10.1021/acs.jpcc.9b04432

Lin, R., & Patrick Ritz, G. (1993). Studying individual macerals using i.r. microspectrometry, and implications on oil versus gas/condensate proneness and “low-rank” generation. *Organic Geochemistry*, *20*(6), 695–706. https://doi.org/10.1016/0146-6380(93)90055-G

Lis, G. P., Mastalerz, M., Schimmelmann, A., Lewan, M. D., & Stankiewicz, B. A. (2005). FTIR absorption indices for thermal maturity in comparison with vitrinite reflectance R0 in type-II kerogens from Devonian black shales. *Organic Geochemistry*, *36*(11), 1533–1552. https://doi.org/10.1016/j.orggeochem.2005.07.001

Liu, K., Ostadhassan, M., Zou, J., Gentizs, T., & Rezaee, R. (2017). Nanoscale pore structure characterization of the Bakken shale in the USA. *Fuel*, *209*, 567–578. https://doi.org/10.1016/j.fuel.2017.08.034

Manka, M. J., Brown, R. L., & Stein, S. E. (1985). Flow ESR and static studies of the decomposition of phenyl-substituted ethanes. *The Journal of Physical Chemistry*, *89*(25), 5421–5427. https://doi.org/10.1021/j100271a022

Michels, R., Langlois, E., Ruau, O., Mansuy, L., Elie, M., & Landais, P. (1996). Evolution of Asphaltenes during Artificial Maturation: A Record of the Chemical Processes. *Energy & Fuels*, *10*(1), 39–48. https://doi.org/10.1021/ef9501410

Murad, S., & Lin, J. (2001). Using Thin Zeolite Membranes and External Electric Fields To Separate Supercritical Aqueous Electrolyte Solutions. *Industrial & Engineering Chemistry Research*, *41*(5), 1076–1083. https://doi.org/10.1021/ie010425+

Plimpton, S. (1995). Fast Parallel Algorithms for Short-Range Molecular Dynamics. *Journal of Computational Physics*, *117*(1), 1–19. https://doi.org/10.1006/JCPH.1995.1039

R. Kelemen, S., Afeworki, M., L. Gorbaty, M., Sansone, M., J. Kwiatek, P., C. Walters, C., Freund, H., Siskin, M., E. Bence, A., J. Curry, D., Solum, M., J. Pugmire, R., Vandenbroucke, M., Leblond, M., & Behar, F. (2007). Direct Characterization of Kerogen by X-ray and Solid-State 13C Nuclear Magnetic Resonance Methods. *Energy & Fuels*, *21*(3), 1548–1561. https://doi.org/10.1021/ef060321h

Rullkötter, J., & Michaelis, W. (1990). The structure of kerogen and related materials. A review of recent progress and future trends. *Organic Geochemistry*, *16*(4–6), 829–852. https://doi.org/10.1016/0146-6380(90)90121-F

Salmon, E., Behar, F., Lorant, F., Hatcher, P. G., & Marquaire, P.-M. (2009). Early maturation processes in coal. Part 1: Pyrolysis mass balance and structural evolution of coalified wood

from the Morwell Brown Coal seam. *Organic Geochemistry*, *40*(4), 500–509. https://doi.org/10.1016/j.orggeochem.2009.01.004

Smith, D. E., & Dang, L. X. (1994). Computer simulations of NaCl association in polarizable water. *The Journal of Chemical Physics*, *100*(5), 3757–3766. https://doi.org/10.1063/1.466363

Takeda, N., & Asakawa, T. (1988). Study of petroleum generation by pyrolysis—I. Pyrolysis experiments by Rock-Eval and assumption of molecular structural change of kerogen using13C-NMR. *Applied Geochemistry*, *3*(5), 441–453. https://doi.org/10.1016/0883-2927(88)90018-2

Tong, J., Han, X., Wang, S., & Jiang, X. (2011). Evaluation of Structural Characteristics of Huadian Oil Shale Kerogen Using Direct Techniques (Solid-State 13C NMR, XPS, FT-IR, and XRD). *Energy & Fuels*, *25*(9), 4006–4013. https://doi.org/10.1021/ef200738p

Tong, J., Jiang, X., Han, X., & Wang, X. (2016). Evaluation of the macromolecular structure of Huadian oil shale kerogen using molecular modeling. *Fuel*, *181*, 330–339. https://doi.org/10.1016/j.fuel.2016.04.139

Van der Heide P. (2011). *X-ray photoelectron spectroscopy: an introduction to principles and practices.* John Wiley & Sons.

Vandenbroucke, M., & Largeau, C. (2006). Kerogen origin, evolution and structure. *Organic Geochemistry*, *38*, 719–833. https://doi.org/10.1016/j.orggeochem.2007.01.001

Wang, H., Qu, Z., Yin, Y., Bai, J., & Yu, B. (2019). Review of Molecular Simulation Method for Gas Adsorption/desorption and Diffusion in Shale Matrix. *Journal of Thermal Science*, *28*(1), 1–16. https://doi.org/10.1007/s11630-018-1053-9

Wang, Qian, Hou, Y., Wu, W., Yu, Z., Ren, S., Liu, Q., & Liu, Z. (2017). A study on the structure of Yilan oil shale kerogen based on its alkali-oxygen oxidation yields of benzene carboxylic acids, 13 C NMR and XPS. *Fuel Processing Technology*, *166*, 30–40. https://doi.org/10.1016/j.fuproc.2017.05.024

Wang, Qing, Cui, D., Wang, P., Bai, J., Wang, Z., & Liu, B. (2018). A comparison of the structures of >300 °C fractions in six Chinese shale oils obtained from different locations

using 1H NMR, 13C NMR and FT-IR analyses. *Fuel*, *211*, 341–352. https://doi.org/10.1016/j.fuel.2017.09.071

Wang, T., Tian, S., Li, G., & Sheng, M. (2018). Selective adsorption of supercritical carbon dioxide and methane binary mixture in shale kerogen nanopores. *Journal of Natural Gas Science and Engineering*, *50*, 181–188. https://doi.org/10.1016/j.jngse.2017.12.002

Wei, Q., & Tang, Y. (2018). 13C-NMR Study on Structure Evolution Characteristics of High-Organic-Sulfur Coals from Typical Chinese Areas. *Minerals*, *8*(2), 49. https://doi.org/10.3390/min8020049

Wei, Z., Gao, X., Zhang, D., & Da, J. (2005). Assessment of Thermal Evolution of Kerogen Geopolymers with Their Structural Parameters Measured by Solid-State 13 C NMR Spectroscopy. *Energy & Fuels*, *19*(1), 240–250. https://doi.org/10.1021/ef0498566

Yao, X.-Q., Hou, X.-J., Wu, G.-S., Xu, Y.-Y., Xiang, H.-W., Jiao, H., & Li, Y.-W. (2002). Estimation of C−C Bond Dissociation Enthalpies of Large Aromatic Hydrocarbon Compounds Using DFT Methods. *The Journal of Physical Chemistry A*, *106*(31), 7184–7189. https://doi.org/10.1021/jp020607x

Zhang, J., Liu, K., Clennell, M. B., Dewhurst, D. N., & Pervukhina, M. (2015). Molecular simulation of CO2–CH4 competitive adsorption and induced coal swelling. *Fuel*, *160*, 309–317. https://doi.org/10.1016/j.fuel.2015.07.092

Zodrow, E. L., D'Angelo, J. A., Helleur, R., & Šimůnek, Z. (2012). Functional groups and common pyrolysate products of Odontopteris cantabrica (index fossil for the Cantabrian Substage, Carboniferous). *International Journal of Coal Geology*, *100*, 40–50. https://doi.org/10.1016/j.coal.2012.06.002

PART 2 PUBLISHED PAPERS

Paper 1: Structure Evolution of Organic Compounds in Shale Plays by Spectroscopy (1H & 13C−NMR, XPS, and FTIR) Analysis

energy&fuels

pubs.acs.org/EF Article

Structural Evolution of Organic Matter in Deep Shales by Spectroscopy (^{1}H and ^{13}C Nuclear Magnetic Resonance, X-ray Photoelectron Spectroscopy, and Fourier Transform Infrared) Analysis

Hyeonseok Lee, Nuri Oncel, Bo Liu, Alexandera Kukay, Furkan Altincicek, Rajender S. Varma, Mohammadreza Shokouhimehr,* and Mehdi Ostadhassan*

Cite This: https://dx.doi.org/10.1021/acs.energyfuels.9b03851 Read Online

ACCESS | Metrics & More | Article Recommendations | Supporting Information

ABSTRACT: Amorphous organic matter in geomaterials also known as kerogen undergoes significant alteration in chemical structure during thermal maturation, which is characterized using a combination of solid-state ^{1}H and ^{13}C nuclear magnetic resonance (NMR), X-ray photoelectron spectroscopy (XPS), and Fourier transform infrared (FTIR) techniques. For this study, four kerogen samples (type II) from the Bakken Formation were selected on the basis of the differences in their thermal maturity as well as representing the pre-oil and oil window stages as measured through organic petrology and bulk geochemical screening of the samples using programmed pyrolysis. Later, organic matter was extracted from selected aliquots for chemical spectroscopy. Results documented a systematic structural change in these four samples, where the ratio of CH_3/CH_2 increased when the maturity increases, along with the presence of a shorter aliphatic chain length. Furthermore, the aromatic carbon structure becomes more abundant in higher maturities and oil window stages quantified by ^{13}C NMR, XPS, and FTIR. Also, the rate of increase in aromaticity demonstrates a considerable rift between the pre-oil window and oil window stages, as verified through bulk geochemical screening of the samples with Rock-Eval 6 pyrolysis hydrogen index. Notably, it is found that kerogen maturation causes the relatively bulky oxygen-related carbon compounds to reduce at the early stages of maturation (pre-oil window), followed by the concentration of such compounds at higher maturity stages. Next, the ratio of carbonyl/carboxyl functional groups to aromatic carbon shows an increase in the oil window stage, while a reduction of sulfur in higher maturities was detected mainly in the SO_x forms. Finally, the nitrogen content of the samples is reported in a variety of forms, which varied regardless of the thermal maturation. It is concluded that the structural and chemical changes that occur in the organic matter involve defunctionalization of heteroatom functional groups, coupled with an increase in cross-linked carbon in the residual remaining kerogen.

1. INTRODUCTION

The abundance of organic carbon and heteroatoms in shale layers, which are deposited in source rocks in the form of organic matter, leads to the generation of hydrocarbon through thermal maturation. The solid-state organic compound (known as kerogen) of these atoms breaks down and undergoes a significant structural and compositional transformation during thermal maturation.[1,2] In this regard, the study pertaining to these changes in kerogen structure has the potential to better characterize CO_2 sequestration and enhanced oil recovery (EOR) methods.[3] However, there is significant difficulty in understanding the mechanism of kerogen cracking coupled to hydrocarbon generation as a result of chemical heterogeneity and complexity of the kerogen molecular structure. Moreover, the limitation of analytical methods could not thoroughly provide quantitative molecular information on the kerogen structure.[4]

Kerogen characterization methods, such as visual kerogen analysis (VKA) and pyrolysis (bulk geochemical techniques), are limited to the determination of the type of kerogen, maturity level, and hydrocarbon generating potential. Hence, to obtain detailed structural information on kerogen, a number of spectroscopic techniques have been deployed.[5−7] The methods mentioned are destructive in addition to the limited information that they can provide; thus, other non-destructive methods, such as Fourier transform infrared (FTIR) spectroscopy, Raman spectroscopy, X-ray photoelectron spectroscopy (XPS), X-ray diffraction (XRD), and ^{1}H and ^{13}C solid-state nuclear magnetic resonance (NMR) have been used to obtain quantitative structural information from kerogen.[5,8−10] These direct methods can examine the solid kerogen sample without imposing any alterations, so that the results would enable studying the structure and assist in building macromolecular models of kerogen though a computational technique at the same time.[11,12]

Organic carbon in source rocks has been investigated by the solid-state ^{13}C NMR technique coupled with FTIR.[13,14] These

Received: November 5, 2019
Revised: January 15, 2020
Published: February 7, 2020

spectroscopic tools can provide the qualitative and quantitative information related to both the structural assignment of carbon and the distribution of aromatic/aliphatic carbons in organic compounds in the past decade.[15−17] To study the organic heteroatoms (oxygen, nitrogen, and sulfur), FTIR and Raman are common methods employed for the analysis of functional groups in complex organic solids. However, as a result of the limitations of the functional groups acquired from these techniques, quantitative analysis is not adequate to fully provide detailed structural information. To complement missing data, XPS has been used to evaluate the organic compounds by overcoming this inherent deficiency to quantify organic heteroatoms with acceptable results.[18,19]

In this study, four isolated (extracted) kerogens from the mineral matrix at four different stages of natural thermal maturity from the Bakken shale formation, from pre-oil to oil window stages, were examined by a combination of non-destructive analytical methods (^{1}H and ^{13}C NMR, XPS, and FTIR) for chemical and structural analyses. The aim of this study was to identify structural characteristics and evolution of solid-state organic compounds as they undergo thermal maturity in nature and to discover these changes in terms of quantitative and qualitative information from a chemical structure point of view. Additionally, we investigated other aspects of thermal maturation that can help us explain processes that would generate hydrocarbons from the organic compounds in the source rock.

2. MATERIALS AND METHODS

2.1. Samples. Solid-state organic compound, type II kerogen samples were extracted from four different wells in the Bakken formation, which is one of the largest unconventional shale oil plays in North America and is currently being studied for unconventional CO_2 EOR and sequestration.[20−22] Initially, the degree of maturity four Bakken kerogen samples (samples A−D) was examined by bitumen reflectance (% SBR_o) along with bulk geochemical properties using Rock-Eval 6 pyrolysis that is summarized in Table 1. In Figure 1 and Table 1, samples A and B are at the thermally immature (pre-oil window) stage, while samples C and D are at the peak mature (oil window) stage. It is important to note that selected kerogen samples were isolated using HCl and HF, and details of the sample preparation and organic matter extraction procedure can be found in studies by Abarghani et al.[23] and Khatibi et al.[24]

Table 1. Properties of Four Solid-State Organic Compound (Kerogen) Samples (Type II)[a]

sample	T_{max} (°C)	TOC (wt %)	HI (mg/g of C)	SBR_o (%)
A	428	14.56	569	0.33
B	432	15.76	531	0.49
C	449	12.69	260	0.72
D	452	16.36	171	0.94

[a]The values were examined by the ultraviolet (UV) reflectance (% SBR_o) and Rock-Eval 6 with parameters: T_{max}, total organic carbon (TOC), and hydrogen index (HI).

2.2. Solid-State ^{1}H and ^{13}C NMR. Solid-state ^{1}H and ^{13}C NMR analysis was carried out using a Bruker Avance III HD spectrometer with cross-polarization/magic angle spinning (CP/MAS). The kerogen sample (100−150 mg) was packed and spun at 5 kHz. A contact time of 1.5 ms and recycle delay time of 5 s were used in the cross-polarization (CP). Resonance frequencies of ^{1}H and ^{13}C NMR were 500 and 125 MHz, respectively, with the spectral widths of 10 and 25 kHz for ^{1}H and ^{13}C NMR. The relative proportion of different carbon types in the samples was quantified through curve fitting of the

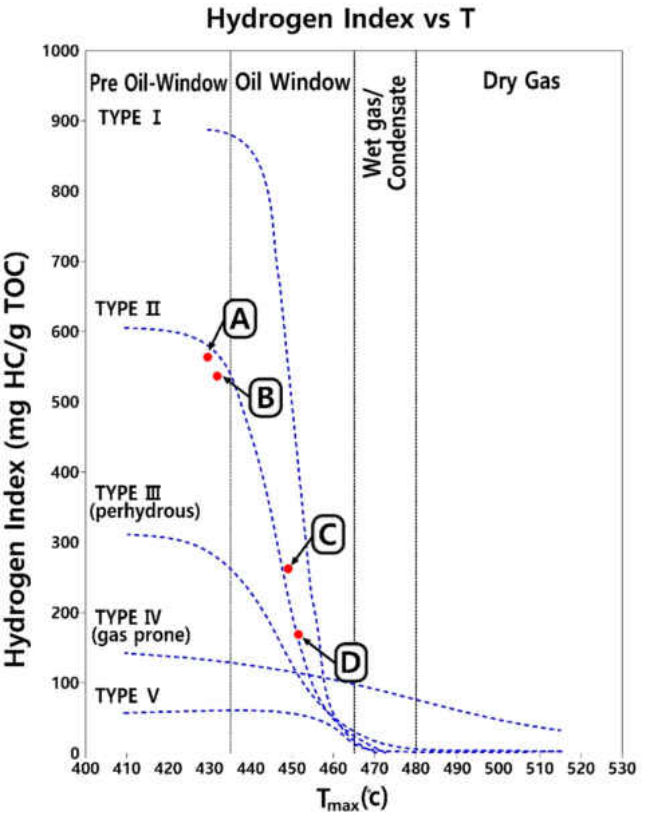

Figure 1. Selected samples A−D are following the kerogen type II thermal maturity trend, where samples A and B are at the thermally immature (pre-oil window) stage and samples C and D are at the peak mature (oil window) stage.

^{13}C NMR spectrum, which was conducted with the ratios of the Gaussian/Lorentzian distribution, the full width at half maximum (fwhm). The details of structural parameters and assignments of chemical data shifts are presented in Table 2.[25,26]

2.3. XPS. Freshly powdered samples were pressed on indium foils and analyzed by a Al Kα (1486.6 eV) X-ray source with pass energy of 89.5 and 44.75 eV for the survey and higher resolution scans, respectively. During the XPS measurements, the pressure was kept at or below 1×10^{-9} mbar. The angle between the X-ray source, which is aligned along the surface normal, and the spectrometer is 54.7. All of the XPS core-level spectra were analyzed using Augerscan and Origin software. The core-level peaks are fitted using a Gaussian−Lorentzian (GL) function to include the instrumental response function along with the core-level line shape. The secondary electron background was subtracted using a Shirley function. We compensated the charging of the sample by irradiating the sample with an electron-flood gun (5 eV).[27]

2.4. FTIR. The infrared (IR) spectra of kerogen samples were recorded in the adsorption range between 450 and 4000 cm^{-1} using a Thermo Fisher Scientific, Nicolet iS50 FTIR spectrometer. Four kerogen samples were pulverized using a ball mill prior to characterizations. FTIR spectroscopy using attenuated total reflectance (ATR) was employed to analyze kerogen extracts. Unlike transmittance FTIR, ATR does not require that kerogen samples be mixed with potassium bromide and formed into pellets under high pressure, thus reducing the time needed for the sample preparation. Kerogen samples were placed in contact with an internal reflection compound, and IR spectra were obtained on the basis of the excitation of the molecular vibrations of chemical bonds by the absorption of the light. The stretching absorptions of a vibrating chemical bond are observed at higher frequencies (wavenumbers) than the corresponding bending or bond deformation vibrations.[28] Because kerogen is a rather complex entity, which limits the analysis

https://dx.doi.org/10.1021/acs.energyfuels.9b03851
Energy Fuels XXXX, XXX, XXX−XXX

Table 2. Structural Parameters and Assignments from ^{13}C NMR Spectra of the Samples[a]

	f_{al}^{1}	f_{al}^{2}	f_{al}^{H1}	f_{al}^{H2}	f_{al}^{O1}	f_{al}^{O2}	f_{ar}^{H}	f_{ar}^{B}	f_{ar}^{S}	f_{ar}^{P}	f_{a}^{C}
ppm	(0−16)	(16−25)	(25−36)	(36−51)	(51−75)	(75−90)	(90−129)	(129−137)	(137−150)	(150−165)	(165−220)
A	0.080	0.050	0.240	0.20	0.056	0.02	0.23	0.032	0.047	0.015	0.030
B	0.075	0.064	0.196	0.19	0.057	0.03	0.25	0.035	0.052	0.024	0.027
C	0.070	0.067	0.165	0.10	0.049	0.05	0.34	0.037	0.061	0.029	0.032
D	0.056	0.066	0.120	0.10	0.051	0.04	0.37	0.045	0.084	0.030	0.038

[a]All ^{13}C chemical shifts (ppm) were measured and assigned in carbon structural functionalities (f_{al}^{1}, aliphatic methyl; f_{al}^{2}, aromatic methyl; f_{al}^{H1}, methylene; f_{al}^{H2}, quaternary carbon; f_{al}^{O1}, methoxyl/aromatic methoxyl; f_{al}^{O2}, aliphatic carbon bonded to oxygen in cyclic hydrocarbon; f_{ar}^{H}, protonated aromatic carbon; f_{ar}^{B}, bridgehead aromatic carbon; f_{ar}^{S}, branched aromatic carbon; f_{ar}^{P}, oxy-aromatic carbon; and f_{a}^{C}, carbonyl/carboxyl carbon).[25,26]

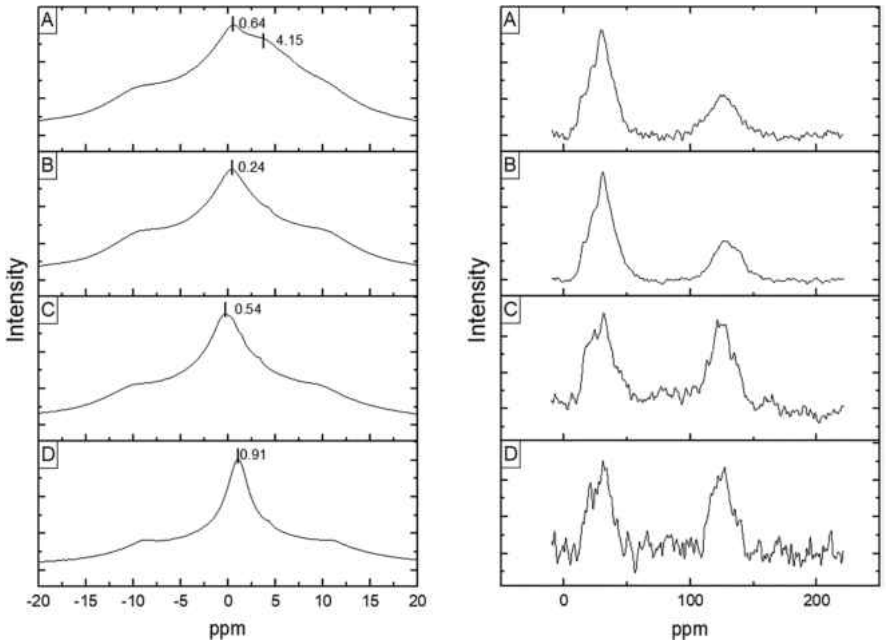

Figure 2. (Left) ^{1}H NMR and (right) ^{13}C NMR spectra of kerogen samples of samples A−D.

of integrated bands in the bending vibration area, we decided to look at the C−H set of stretch vibrations observed in kerogen samples, as proposed in previous studies;[28,29] bands of the absorption were identifying by comparison to published spectra.

3. RESULTS

3.1. Solid-State ^{1}H and ^{13}C NMR. Aromatic and aliphatic proton regions of the ^{1}H NMR spectrum provide relatively qualitative information on hydrogen at different maturity levels.[26] From the acquired spectra on the left panel of Figure 2, aromatic and aliphatic protons exist in the 6.4−8.3 and 0.5−4.3 ppm ranges, respectively. The ^{1}H NMR spectra of samples A−D on the left panel of Figure 2 show a broad asymmetric line centered around 0−1 ppm (centered at 0.64, 0.24, 0.54, and 0.91 ppm, respectively). Sample A (immature) has a strong intensity in the range of the aliphatic protons between 0.5 and 4.3 ppm; the peak at 4.15 ppm indicates that the ratio of aliphatic protons to the aromatic ring is higher than the rest of the samples. In this regard, the results reveal that the shape of ^{1}H NMR spectrum becomes sharp as the degree of maturity increases, which manifests the number of protons attached to aliphatic carbon reduces. However, the ^{1}H NMR spectra output as a result of highly overlapping peaks was difficult to distinguish and quantify the structural formation of hydrogen, which has been a problem in the past.[30,31] Therefore, we decided to rely solely on the result of ^{13}C NMR to extract quantitative information about carbon-related structures.

The ^{13}C NMR spectra of kerogen samples mainly reveal three regions: the aliphatic region at 0−90 ppm, the aromatic region at 100−165 ppm, and carbonyl/carboxyl carbon region at 165−220 ppm.[25,26] The right panel of Figure 2 illustrates that the ^{13}C NMR spectrum of immature kerogen is distinct from that of mature kerogen in the range of the aromatic carbons between 90 and 220 ppm. Highly matured kerogen has a stronger intensity in the ^{13}C NMR spectrum related to the aromatic structure. To acquire the details of carbon structural information, overlapping peak resolving of the ^{13}C NMR spectra is deconvoluted by the fitting procedure. The relative areas calculated by the peak fitting, which represent the relative amount of the carbon-containing functional groups, are listed in Table 2.

As shown in the ^{13}C NMR analysis (Table 2), with increasing thermal maturity, the aliphatic functional groups (0−90 ppm) exhibit a reduction trend in the relative amount of carbon, whereas the aromatic carbon groups (90−165 ppm) increase. This behavior is in an agreement with ^{1}H NMR spectra on the left panel of Figure 2. The nonpolar alkyl carbons (0−51 ppm) generally diminish with the degree of maturity, except the aromatic methyl (f_{al}^{2}) group, which could be reflected by the increase of aromatic carbon. In addition, we infer that loss of oxygen at the early stages of maturation is due to a comparatively weak bond between oxygen-related carbon and the kerogen backbone.[19] However, the results revealed

https://dx.doi.org/10.1021/acs.energyfuels.9b03851
Energy Fuels XXXX, XXX, XXX−XXX

that there is not any meaningful relationship between oxygen-related carbons (f_{al}^{O1}, f_{al}^{O2}, and f_{a}^{C}) and thermal maturity. We understand that, because the stoichiometry of the oxygen-related signal is uncertain,[29] it is difficult to estimate the accurate values concerning oxygen-related carbon. However, this study additionally investigated the changes of oxygen-related carbon with XPS and FTIR during the maturation, and on the basis of the results given in Table 2, the evaluations of the carbon skeletal structure were correlated to the maturity levels of kerogen that is discussed later.

3.2. XPS. Different types of organic carbon and oxygen forms were determined by analyzing the carbon (1s) peak. In each sample, we determined four peaks located at approximately 285, 286, 287.5, and 289 eV after fitting the XPS carbon (1s) signal. The peak at 285 eV was attributed to both aromatic and aliphatic carbon. The amount of aromatic carbon was estimated using the XPS technique for $\prod$ to $\prod^*$ signal intensity, as used previously.[32] This confirms that highly mature kerogen has an abundance of the aromatic carbon structure, as revealed in the solid-state ^{1}H and ^{13}C NMR results. The peaks at 286, 287.5, and 289 eV originate from carbon atoms bound to one oxygen atom by a single bond (C−O), carbon atoms bound to one oxygen atom by double bonds (C═O), and carbon atoms bound to two oxygen atoms via both double and single bonds (O═C−O), respectively. In the most mature stage (sample D), the results show a relatively large amount of enrichment for oxygen-related carbon, whereas the rest of the samples (A−C) exhibit a comparatively similar amount of oxygen-related carbons in the kerogen structure (Table 3).

Organic nitrogen and sulfur information in the kerogen structure was also obtained using XPS curve-fitting methods, which at different energy positions are used to fit with the XPS N 1s and S 2p spectra, respectively. Nitrogen (1s) kerogen spectra were curve-resolved using four peaks at fixed energy positions of 397, 398.6, 399.4, 400.2, and 401.4 eV. Considering organic sulfur (2p), the binding energy between 162 and 165.7 eV is assigned to pyrite, aliphatic, and aromatic sulfur and sulfoxide in the XPS S 2p spectrum having $2p_{3/4}$ and S $2p_{1/2}$. The peaks from 168.0 (±0.5) to 170.5 (±0.5) eV can be indexed to S $2p_{3/4}$ and S $2p_{1/2}$ of SO_x (sulfate/sulfite/sulfone). The peak locations, which are a little higher than the expectation, could be affected by the poor electrical contact in surface oxidation; the accumulation of positive charge shifts peaks toward a higher binding energy. Because the peaks at 168.0 and 160.5 eV are overlapped and have also been observed in previous literature, we consider that the summation of this region presents the SO_x assignment of sulfate, sulfite, and sulfoxide.[5,29] Table 3 exhibits the details of quantitative structural parameters based on the curve fitting into different components of the selected kerogen samples (A−D).

Table 3. Structural Parameters and Assignment for the XPS Spectra of the Kerogen Samples

			mole percent			
elemental	functionality	binding energy (eV)	A	B	C	D
C1 1s	aliphatic	248.8	49	58	40	16.4
	aromatic[a]		39	34	50	55
	C−O	286	1.2	0.6	1.4	23.1
	O−C═O	287.5	3.5	6.2	11	6.2
	C═O	289	7.3	4.6	2.8	2.3
N 1s	nitride	397		19.8	24.8	12.5
	pyridinic	398.6		16.4	15.7	22.2
	quaternary	401.4		23.6	10.6	31.3
	amino	399.4		20.6	42	9.8
	pyrrolic	400.2		19.6	6.8	24.2
S 2p	pyrite (FeS_2)	162	13.5	16.4	6.2	0.5
	aliphatic	163	10.1	1.7	1.5	11.9
	aromatic	164	20.1	1.3	3	14.9
	sulfoxide	165.7	0.3	0	0	5.3
	SO_x[b]	168−170.5	58.0	80.6	89.4	67.4

[a]The amount of aromatic carbon was estimated by the technique of XPS $\prod$ to $\prod^*$ signal intensity in previous literature.[32] [b]The summation of the region presents the SO_x assignment of sulfate, sulfite, and sulfoxide.

3.3. FTIR. The intensities, depicted in Figure 3, correspond to the asymmetric and symmetric stretching and bending of

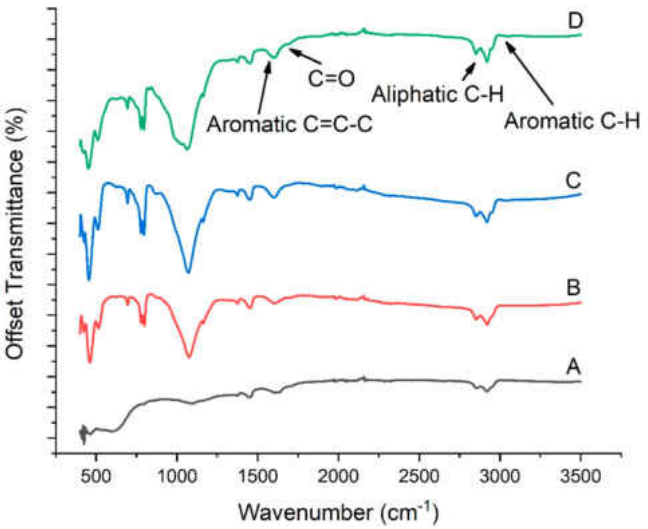

Figure 3. FTIR spectra of kerogens with increasing maturity exhibit the changes in the C−H stretch vibration area (2800−3200 cm^{-1}), aromatic C═C−C ring stretch vibration area (1615−1580 cm^{-1}), and carbonyl/carboxyl group vibration area (1650−1750 cm^{-1}).

the C−H/C═O/C═C−C bonds about the central carbon atom on a relative basis in the spectra of kerogen samples. The reason for the overlapped original spectra is due to the same amount of energy, which is required for several vibrations. Therefore, IR structural evaluations have been established from acquired spectra documented in earlier studies.[2,26] To find the intensities at desired frequencies, the FTIR spectrum areas 1800−1500 and 3200−2700 cm^{-1} were fitted by the Fourier self-deconvolution;[33] the coefficients of determination (R^2) of the peak fitting for the region in all spectra were found between 0.994 and 0.996.

Here, we examined the C−H stretching band intensities for CH_3, CH_2, aromatic ring CH, aromatic ring C═C−C, and C═O based on the deconvolution results. Four indices (CH_3/CH_2 ratio, aromaticity, *A* factor, and *C* factor) were used to evaluate the structural characteristic of each different kerogen. The CH_3/CH_2 ratio $[I_{(2970-2950)}/I_{(2935-2915)}]$ indicates the average chain length of the aliphatic and the degree of chain branching. Aromaticity $[I_{(3130-3070)}/(I_{(2970-2950)} + I_{(2935-2915)})]$ represents the degree of aromatic structure versus aliphatic

https://dx.doi.org/10.1021/acs.energyfuels.9b03851
Energy Fuels XXXX, XXX, XXX−XXX

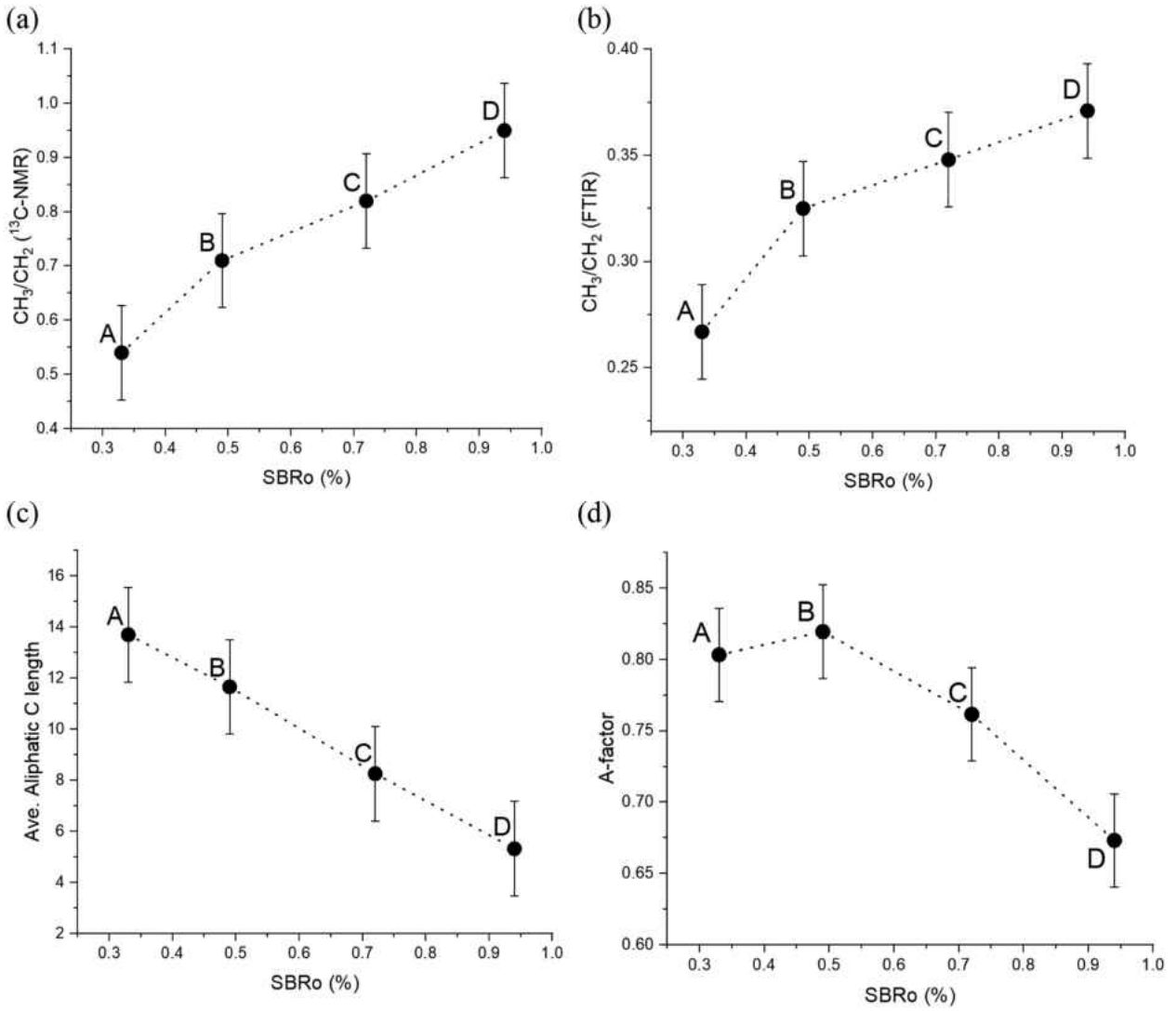

Figure 4. Aliphatic carbon structure changes by thermal maturity. The ratio of methyl/methylene is estimated from (a) ^{13}C NMR $[(f_{al}^{1} + f_{al}^{2})/f_{al}^{H1}]$ and (b) FTIR $[I_{(2970-2950)}/I_{(2935-2915)}]$ results. (c) Average aliphatic carbon chain length by ^{13}C NMR $[(f_{al}^{1} + f_{al}^{2} + f_{al}^{H1} + f_{al}^{H2} + f_{al}^{O1} + f_{al}^{O2})/f_{ar}^{S}]$. (d) *A* factor by FTIR $[I_{(2935-2915)}/(I_{(2935-2915)} + I_{(1615-1580)})]$. Error bars represent standard errors.

chain structure. The *A* factor $[I_{(2935-2915)}/(I_{(2935-2915)} + I_{(1615-1580)})]$ and *C* factor $[I_{(1750-1650)}/(I_{(1750-1650)} + I_{(1615-1580)})]$ describe the relative amount of aliphatic carbon and oxygenated carbon to aromatic carbon, respectively,[26] and all indices are calculated through integrating the area under the curves. When the maturity increases, the CH_3/CH_2 ratio acquired demonstrates that the aliphatic chain length is comparatively shorter and the branching is developed. Restated, highly mature kerogen has more aromatic ring contribution and less methyl/methylene involvement with the expected increase in the aromatic structure (aromaticity index). The observed trends corroborate findings from previous studies where, during the maturation, chemical structure changes have been drawn into shorten aliphatic chain length and expanding aromaticity.[26] The result of the *A* factor, regarding the relative amount of aliphatic to aromatic carbon, indicates that there is generally a decreasing trend over the degree of maturation. Oxygen-related information (*C* factor) reveals that the ratio of oxygen-related carbon to aromatic carbon initially decreases (immature stage) and then rises as the mature stage advances; the comparative details of the indices are discussed in more details in the Discussion.

4. DISCUSSION

4.1. Carbon Structural Changes. The ratios of CH_3/CH_2 from ^{13}C NMR have an order of increase similar to those obtained from the FTIR analysis when the maturity increases (panels a and b of Figure 4), which is consistent with the previously described data from the type II kerogen structure.[34] This growth of the CH_3/CH_2 ratio could be evidence of chain cleavage coupled with hydrocarbon generation. While kerogen maturation occurs naturally, the molecular structure of this macromolecule evolves through bond breaking and bond forming, under changing physical conditions (temperature, pressure, and time) of the subsurface.[1,35] In terms of carbon−carbon (C−C) bond in the kerogen structure, bond dissociation energy (BDE) between α and β carbon is weaker than that between α and aromatic carbon.[33,36] Also, short branching carbon (such as methyl) to carbon in the backbone structure has less BDE than longer chain carbon.[20,34] It appears that kerogen samples of the Bakken shale play also follow this

https://dx.doi.org/10.1021/acs.energyfuels.9b03851
Energy Fuels XXXX, XXX, XXX−XXX

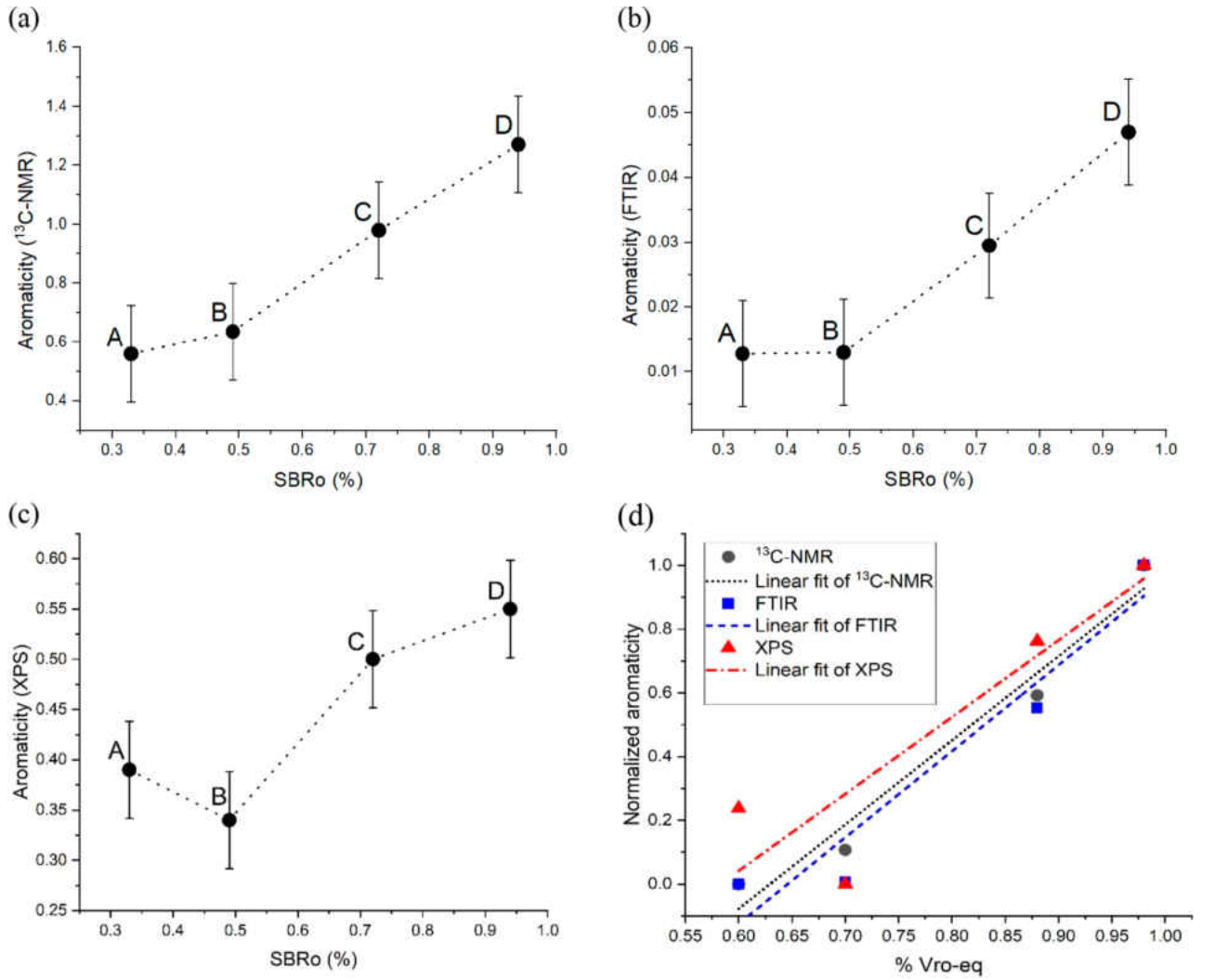

Figure 5. Aromatic carbon structural changes by thermal maturity. The aromaticity (aromatic carbon/aliphatic carbon) was calculated from (a) ^{13}C NMR ($f_{ar}^{H} + f_{ar}^{B} + f_{ar}^{S} + f_{ar}^{P}$), (b) FTIR [$I_{(3130-3070)}/(I_{(2970-2950)} + I_{(2935-2915)})$], and (c) XPS (mole percent aromatic carbon). (d) Comparison of aromaticity slope trends (linearly fitted). Error bars represent standard errors.

mechanism, which indicates a higher ratio of CH_3/CH_2 during thermal maturation, as shown in panels a and b of Figure 4. In addition to the ratio of CH_3/CH_2, the average aliphatic carbon length and amount of aromatic carbon follows this trend too. Figure 4c explains that the average length of aliphatic carbon reduces as the maturity increases, thereby meaning that thermal maturation accompanies the structural changes in kerogen with both shorter aliphatic chain and a higher ratio of CH_3/CH_2, as delineated by FTIR and ^{13}C NMR.

Also, the *A* factor calculated through FTIR data (Figure 4d) shows that the relative ratio of aliphatic to aromatic carbon generally decreases in accordance with the shape of the ^{1}H NMR spectrum, apart from sample B that has the highest overall value. The higher *A* factor value of sample A than sample B was expected because the ratio of CH_3/CH_2 increases, and as a result, the aliphatic chain length becomes shorter. However, sample B was found to have the largest *A* factor, and this could be explained by the fact that the quantities of aromatic carbon in sample B are relatively lower than expected. This result is confirmed by the information that is obtained from the analysis of aromatic carbon that is presented in Figure 5.

Figure 5 depicts aromatic carbon as investigated by three different analytical methods: ^{13}C NMR, FTIR, and XPS. Panels a–c of Figure 5 verify our findings that a higher maturity kerogen overall tends to have a larger amount of aromatic carbon. This is also compatible with the ^{1}H NMR result, which infers the ratio of aliphatic protons to the aromatic ring compared to the rest of the protons. With an increase of maturity (from samples A to D), the spectrum becomes sharper and has diminished intensity in the range of the aliphatic protons between 0.5 and 4.3 ppm, which represents the abundance of the aromatic structure. This observation is collectively acceptable, excluding sample B, with the amount of aromatic carbon of XPS being comparatively 13% lower than that of ^{13}C NMR.

FTIR results also propose that the aromaticity value of sample B is similar to that of sample A, which is different from the overall observed trend. This latest outcome can support lower *A* factor values for sample B compared to sample A, as seen in Figure 4d. In addition, the degree of aromaticity (Figure 5d) estimated from three techniques (^{13}C NMR, FTIR, and XPS) strongly confirms that the aromaticity is increasing. Notably, we found that, on the basis of the aromaticity results, there is relatively a considerable rift

https://dx.doi.org/10.1021/acs.energyfuels.9b03851
Energy Fuels XXXX, XXX, XXX−XXX

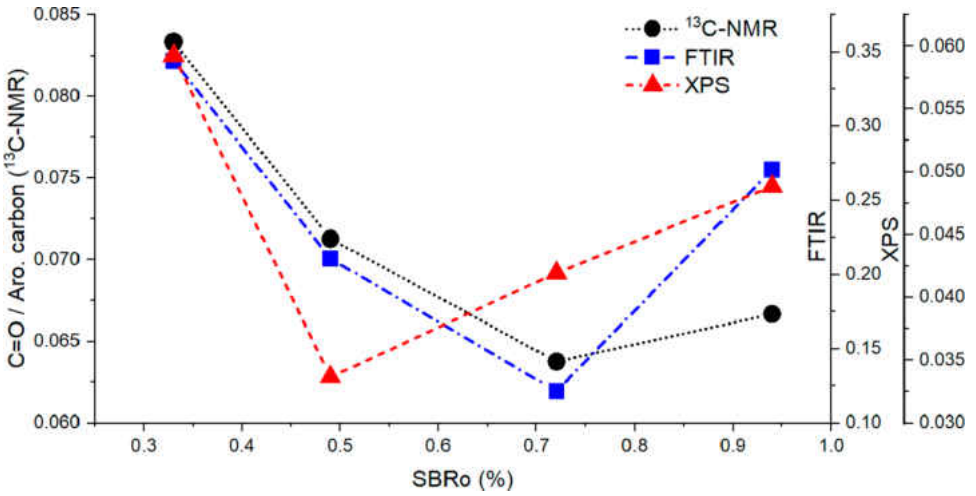

Figure 6. Ratios of C═O/aromatic carbon were estimated from ^{13}C NMR, FTIR, and XPS results, which were calculated by $f_a^C/(f_{ar}^H + f_{ar}^B + f_{ar}^S + f_{ar}^P)$, *C* factor $[I_{(1650-1750)}/(I_{(1650-1750)} + I_{(1615-1580)})]$, and [(mole percent of total oxygen)(C═O and C−O═O fraction)/(mole percent of aromatic carbon)], respectively.

between pre-oil and oil window stage samples. Following the oil window stage, the amount of aromatic carbon fairly increases as well as the rate of change in aromaticity, as seen by the slope of the curve, which is found higher through advancing thermal maturity in the oil generation window.

On the basis of the results, the structural changes of Bakken kerogen, coupled with hydrocarbon generation, are affected by the C−C BDE during the thermal maturation process. As a result of the weaker BDE between α and β carbons than that between α and aromatic carbons, breaking the aliphatic chain bond leads to both hydrocarbon generation and the aromatic abundant structure in the kerogen backbone. In other words, during the thermal maturation, a comparatively light hydrocarbon was detached and the remaining kerogen backbone became a relatively solid-state organic compound having an abundant aromatic structure and well-organized rings.

4.2. Heteroatoms. The loss of oxygen functional groups drives early structural changes. Because the oxygen-related carbon bonds have relatively weak BDE, the carboxyl and carbonyl groups can be easily defunctionalized.[21,34] In our study, the results revealed that kerogen maturation involves relatively bulky oxygen-related carbon reduction at the early stage of maturation (pre-oil window) and then increases in the oil window stage, which is verified by ^{13}C NMR and XPS in Tables 2 and 3.

The changes in the ratios of C═O/aromatic carbon were investigated by three methods (^{13}C NMR, FTIR, and XPS) depicted in Figure 6. Because it is difficult to analyze the organic oxygen group from ^{13}C NMR,[29] the comparison of the three methods is presented in the same graph to help us better understand and verify the results. As thermal maturity increases, first, the ratio of C═O/aromatic carbon decreases, regardless of the method, along with the ratio of carbonyl/carboxyl functional groups to aromatic carbon, which was also found to reduce at the early stages of maturation. Then, in the oil window stage (samples C and D), the ratio of C═O/aromatic carbon starts to rise, showing the amount of oxygen estimated in sample D to become higher than sample C. Although most oxygen-containing functional groups will be expelled from the organic matter during the initial stages of thermal maturation, the results exhibit an unexpected increase in the oxygen content of the functional groups in the higher maturity ranges of kerogen. This can be explained by the enrichment of oxygen through the addition of oxygen from inorganic mineral or water (interstitial water) impurities as thermal maturity increases, which are also observed in other studies.[22,34] It is also expected that the formation of insoluble pyrobitumen, which is highly oxidized as thermal maturity advances, may lead to an unexpected increase of the C═O/aromatic carbon ratio in higher thermal maturation.[8]

The observations pertaining to organic sulfur in our kerogen samples clearly exhibit that the amount of sulfur would decrease significantly as maturation progresses, even from the early onset of this process. The result that is obtained from the XPS data analysis depicts that sample A contains the largest number of sulfur atoms (2.8 sulfur atoms per 100 carbon atoms), whereas samples B−D were measured with lower quantities of sulfur (1.4, 1.1, and 0.7 sulfur atoms per 100 carbon atoms, respectively) compared to sample A. This observed phenomenon is due to the fact that the maturation process entails the depolymerization of the kerogen structure by breaking the weaker bonds (C−O and C−S) that led to generating heavier soluble bitumen compounds, as explained in the literature.[37] Organic sulfur in aliphatic and aromatic compounds, sulfoxide, and SO_x (sulfate/sulfite/sulfone) in addition to inorganic sulfur and pyrite is clearly recorded in the analysis and appears in all spectra, as shown in Table 3. Organic nitrogen as detected by XPS revealed that it mainly contains pyrrolic, pyridinic, quaternary, and amino, which is detected by several peaks based on their energy positions;[5,29] the nitrogen data for each kerogen sample is summarized in Table 3. On the basis of the XPS results from the Bakken kerogen samples, we deduced that a variety of nitrogen-containing compounds can exist in the samples, regardless of their thermal maturation stage. This means that we were not able to establish a meaningful pattern in the changes that would occur in nitrogen quantities as a function of thermal maturation in our samples, and further studies are required to investigate the role of organic nitrogen during depolymerization of the kerogen structure.

Generally speaking, on the basis of the results, the weak bonds in the complex structure of kerogen start to detach containing bonds between C and O and between C and S at the early stages of maturation. These bond-breaking reactions

https://dx.doi.org/10.1021/acs.energyfuels.9b03851
Energy Fuels XXXX, XXX, XXX−XXX

would lead to the generation of H_2S gas, NSO compounds, and a heavy soluble compound (bitumen). It needs to be reiterated that the structural and chemical evolution of Bakken kerogen involves defunctionalization of heteroatom functional groups, coupled with an increase in cross-linked carbon in residual higher maturity kerogen.

5. CONCLUSION

This study shows how hydrocarbon generation can impose changes in the source rock organic compound structure during the maturation process. The analysis of extracted kerogen through spectroscopic techniques (^{1}H and ^{13}C NMR, XPS, and FTIR) was used to determine chemical contents and molecular structures as maturation advances. This study will enable us to better model separation and capture processes in shale plays via theoretical methods. On the basis of the results, the following conclusions can be made: (1) The structural changes of kerogen pertaining to the abundance of the aromatic and aliphatic chain length correlate well with the maturity of kerogen. On the basis of the aliphatic carbon chain that is detected in the kerogen structure by ^{1}H and ^{13}C NMR and FTIR, the ratio of CH_3/CH_2 increases when the maturity increases, accompanied with the shorter aliphatic chain length. (2) In contrast to aliphatic carbon, the aromatic carbon structure becomes more abundant in higher maturity and oil window stage. All three techniques (^{13}C NMR, XPS, and FTIR) confirm an increasing trend similar to aromaticity with the same rate of changes. Also, a considerable discrepancy between pre-oil window and oil window stages regarding aromaticity was observed. (3) Kerogen maturation causes the relatively bulky oxygen compound reduction at the early stage of maturation (pre-oil window) with an increase in the oil window stage based on ^{13}C NMR and XPS results. In addition, the ratio of carbonyl/carboxyl functional groups to aromatic carbon shows an increase in the oil window stage (mature kerogen). This may be driven by contamination from inorganic oxygen in mineral or interstitial water impurities. Besides, the formation of insoluble oxygen-rich pyrobitumen can lead to enrichment of the C═O/aromatic carbon ratio. (4) The reduction of sulfur in kerogen was observed as the level of maturity increases, mostly in SO_x forms. Finally, the XPS results exhibited that the diverse form of nitrogen could exist regardless of the thermal maturation stage; however, further investigations of heteroatoms are necessary for a better understanding of changes in the NSO content as a function of thermal maturity.

■ ASSOCIATED CONTENT

Supporting Information

The Supporting Information is available free of charge at https://pubs.acs.org/doi/10.1021/acs.energyfuels.9b03851.

^{13}C NMR spectra of the samples (Figure S1), ^{1}H NMR spectra of the samples (Figure S2), FTIR spectra of the samples (Figure S3), XPS spectra of sample A (Figure S4), XPS spectra of sample B (Figure S5), XPS spectra of sample C (Figure S6), and XPS spectra of sample D (Figure S7) (PDF)

■ AUTHOR INFORMATION

Corresponding Authors

Mehdi Ostadhassan − *Key Laboratory of Continental Shale Hydrocarbon Accumulation and Efficient Development, Ministry of Education, Northeast Petroleum University, Daqing 163318, China;* orcid.org/0000-0001-9235-4399; Email: mehdi.ostadhassan@nepu.edu.cn

Mohammadreza Shokouhimehr − *Department of Materials Science and Engineering, Research Institute of Advanced Materials, Seoul National University, Seoul 08826, Republic of Korea; Department of Petroleum Engineering, University of North Dakota, Grand Forks, North Dakota 58202, United States;* orcid.org/0000-0003-1416-6805; Email: mrsh2@snu.ac.kr

Authors

Hyeonseok Lee − *Department of Petroleum Engineering, University of North Dakota, Grand Forks, North Dakota 58202, United States*

Nuri Oncel − *Department of Physics & Astrophysics, University of North Dakota, Grand Forks, North Dakota 58202, United States;* orcid.org/0000-0002-0292-3349

Bo Liu − *Key Laboratory of Continental Shale Hydrocarbon Accumulation and Efficient Development, Ministry of Education, Northeast Petroleum University, Daqing 163318, China*

Alexandera Kukay − *Department of Physics & Astrophysics, University of North Dakota, Grand Forks, North Dakota 58202, United States*

Furkan Altincicek − *Department of Physics & Astrophysics, University of North Dakota, Grand Forks, North Dakota 58202, United States*

Rajender S. Varma − *Regional Centre of Advanced Technologies and Materials, Faculty of Science, Palacky University in Olomouc, 783 71 Olomouc, Czech Republic;* orcid.org/0000-0001-9731-6228

Complete contact information is available at: https://pubs.acs.org/10.1021/acs.energyfuels.9b03851

Notes

The authors declare no competing financial interest.

■ REFERENCES

(1) Durand, B. Sedimentary Organic Matter and Kerogen. Definition and Quantitative Importance of Kerogen. In *Kerogen, Insoluble Organic Matter from Sedimentary Rock*; Durand, B., Ed.; Editions Technips: Paris, France, 1980; pp 13−34.

(2) Rullkötter, J.; Michaelis, W. The Structure of Kerogen and Related Materials. A Review of Recent Progress and Future Trends. *Org. Geochem.* **1990**, *16* (4−6), 829−852.

(3) Lee, H.; Shakib, F. A.; Shokouhimehr, M.; Bubach, B.; Kong, L.; Ostadhassan, M. Optimal separation of CO_2/CH_4/Brine with amorphous Kerogen: A thermodynamics and kinetics study. *J. Phys. Chem. C* **2019**, *123* (34), 20877−20883.

(4) Vandenbroucke, M.; Largeau, C. Kerogen Origin, Evolution and Structure. *Org. Geochem.* **2007**, *38*, 719−833.

(5) Tong, J.; Han, X.; Wang, S.; Jiang, X. Evaluation of Structural Characteristics of Huadian Oil Shale Kerogen Using Direct Techniques (Solid-State ^{13}C NMR, XPS, FT-IR, and XRD). *Energy Fuels* **2011**, *25*, 4006−4013.

(6) Tong, L.; Jiang, X.; Han, X.; Wang. Evaluation of the macromolecular structure of Huadian oil shale kerogen using molecular modeling. *Fuel* **2016**, *181*, 330−339.

(7) Clough, A.; Sigle, J. L.; Jacobi, D.; Sheremata, J.; White, J. L. Characterization of Kerogen and Source Rock Maturation Using Solid-State NMR Spectroscopy. *Energy Fuels* **2015**, *29*, 6370−6382.

(8) Lis, G. P.; Mastalerz, M.; Schimmelmann, A.; Lewan, M. D.; Stankiewicz, B. A. FTIR absorption indices for thermal maturity in comparison with vitrinite reflectance R0 in type-II kerogens from Devonian black shales. *Org. Geochem.* **2005**, *36*, 1533−1552.

https://dx.doi.org/10.1021/acs.energyfuels.9b03851
Energy Fuels XXXX, XXX, XXX−XXX

(9) Khatibi, S.; Ostadhassan, M.; Tuschel, D.; Gentzis, T.; Bubach, B.; Carvajal-Ortiz, H. Raman spectroscopy to study thermal maturity and elastic modulus of kerogen. *Int. J. Coal Geol.* **2018**, *185*, 103−118.
(10) Wei, Z.; Gao, Z.; Zhang, D.; Da, J. Assessment of Thermal Evolution of Kerogen Geopolymers with Their Structural Parameters Measured by Solid-State ^{13}C NMR Spectroscopy. *Energy Fuels* **2005**, *19*, 240−250.
(11) Lee, H.; Ostadhassan, M.; liu, K.; Bubach, B. Developing an Amorphous Kerogen Molecular Model Based on Gas Adsorption Isotherms. *ChemRxiv* **2019**; DOI: 10.26434/chemrxiv.7965152.
(12) Khatibi, S.; Ostadhassan, M.; Aghajanpour, A. Raman spectroscopy: An analytical tool for evaluating organic matter. *J. Oil Gas Petrochem. Sci.* **2018**, *1*, 28−33.
(13) Renault, M.; Cukkemane, A.; Baldus, M. Solid-State NMR Spectroscopy on Complex Biomolecules. *Angew. Chem., Int. Ed.* **2010**, *49*, 8346−8357.
(14) Minor, E. C.; Swenson, M. M.; Mattson, B. M.; Oyler, A. R. Structural characterization of dissolved organic matter: a review of current techniques for isolation and analysis. *Environ. Sci.: Processes Impacts* **2014**, *16*, 2064−2079.
(15) VanderHart, D. L.; Retcofsky, H. L. Estimation of Coal Aromaticities by Proton-Decoupled Carbon-13 Magnetic Resonance Spectra of Whole Coals. *Fuel* **1976**, *55*, 202−204.
(16) Hatcher, P. G.; Wilson, M. A.; Vassallo, A. M.; Lerch, H. E. Studies of Angiospermous Wood in Australian Brown Coal by Nuclear Magnetic Resonance and Analytical Pyrolysis: New Insights into the Early Coalification Process. *Int. J. Coal Geol.* **1989**, *13*, 99−126.
(17) Wang, S.; Tang, Y.; Schobert, H. H.; Guo, Y.; Su, Y. FTIR and ^{13}C NMR Investigation of Coal Component of Late Permian Coals from Southern China. *Energy Fuels* **2011**, *25*, 5672−5677.
(18) Kelemen, S. R.; Afeworki, M.; Gorbaty, M. L.; Cohen, A. D. Characterization of Organically Bound Oxygen Forms in Lignites, Peats, and Pyrolyzed Peats by X-ray Photoelectron Spectroscopy (XPS) and Solid-State ^{13}C NMR Methods. *Energy Fuels* **2002**, *16*, 1450−1462.
(19) Wang, Q.; Hou, T.; Wu, W.; Yu, Z.; Ren, S.; Liu, Q.; Liu, Z. A Study on the Structure of Yilan Oil Shale Kerogen based on Its Alkali-Oxygen Oxidation Yields of Benzene Carboxylic Acids, ^{13}C NMR and XPS. *Fuel Process. Technol.* **2017**, *166*, 30−40.
(20) Lin, R.; Ritz, G. P. Studying Individual Macerals using i.r. Microspectroscopy, and Implications on Oil versus Gas/Condensate Proneness and "low-rank" Generation. *Org. Geochem.* **1993**, *20*, 695−706.
(21) Salmon, E.; Behar, F.; Lorant, F.; Hatcher, P. G.; Marquaire, P. M. Early Maturation Processes in Coal. Part 1: Pyrolysis Mass Balance and Structural Evolution of Coalified Wood from the Morwell Brown Coal Seam. *Org. Geochem.* **2009**, *40*, 500−509.
(22) Michels, R.; Langlois, E.; Ruau, O.; Mansuy, L.; Elie, M.; Landais, P. Evolution of Asphaltenes during Artificial Maturation: A Record of the Chemical Processes. *Energy Fuels* **1996**, *10*, 39−48.
(23) Abarghani, A.; Ostadhassan, M.; Gentzis, T.; Carvajal-Ortiz, H.; Bubach, B. Organofacies study of the Bakken source rock in North Dakota, USA, based on organic petrology and geochemistry. *Int. J. Coal Geol.* **2018**, *188*, 79−93.
(24) Khatibi, S.; Ostadhassan, M.; Tuschel, D.; Gentzis, T.; Carvajal-Ortiz, H. Evaluating Molecular Evolution of Kerogen by Raman Spectroscopy: Correlation with Optical Microscopy and Rock-Eval Pyrolysis. *Energies* **2018**, *11*, 1406.
(25) Wei, Q.; Tang, T. ^{13}C-NMR Study on Structure Evolution Characteristics of High-Organic-Sulfur Coals from Typical Chinese Areas. *Minerals* **2018**, *8*, 49.
(26) Wang, Q.; Cui, D.; Wang, P.; Bai, J.; Wang, Z.; Liu, B. A Comparison of the Structures of >300 °C Fractions in Six Chinese Shale Oils Obtained from Different Locations using ^{1}H NMR, ^{13}C NMR and FT-IR. *Fuel* **2018**, *211*, 341−352.
(27) Heide, P. V. D. *X-ray Photoelectron Spectroscopy—An Introduction to Principles and Practices*; Wiley: Hoboken, NJ, 2012.
(28) Coates, J. Interpretation of Infrared Spectra, A Practical Approach. In *Encyclopedia of Analytical Chemistry*; Meyers, R. A., Ed.; John Wiley & Sons, Ltd.: Chichester, U.K., 2006; DOI: 10.1002/9780470027318.a5606.
(29) Kelemen, S. R.; Afeworki, M.; Gorbaty, M. L.; Sansone, M.; Kwiatek, P. J.; Walters, C. C.; Freund, H.; Siskin, M.; Bence, A. E.; Curry, D. J.; Solum, M.; Pugmire, R. J.; Vandenbroucke, M.; Leblond, M.; Behar, F. Direct Characterization of Kerogen by X-ray and Solid-State ^{13}C Nuclear Magnetic Resonance Methods. *Energy Fuels* **2007**, *21*, 1548−1561.
(30) Borrego, A. G.; Blanco, C. G.; Prado, J. G.; Diaz, C.; Guillen, M. D. ^{1}H NMR and FTIR Spectroscopic Studies od Bitumen and Shale Oil from Selected Spanish Oil Shales. *Energy Fuels* **1996**, *10*, 77−84.
(31) Premovic, P. I.; Jovanovic, Lj. S.; Michel, D. Solid-State ^{13}C and ^{1}H NMR in Kerogen Research: Uncertainty of Aromaticity Estimation. *Appl. Spectrosc.* **1992**, *46*, 1750−1752.
(32) Kelemen, S. R.; Rose, K. D.; Kwiatek, P. J. Carbon aromaticity based on XPS $\prod$ to $\prod^*$ signal intensity. *Appl. Surf. Sci.* **1993**, *64*, 167−173.
(33) Yao, X.; Hou, X.; Wu, G.; Xu, Y.; Xiang, H.; Jiao, H.; Li, Y. Estimation of C−C Bond Dissociation Enthalpies of Large Aromatic Hydrocarbon Compounds Using DFT Methods. *J. Phys. Chem. A* **2002**, *106*, 7184−7189.
(34) Craddock, P. R.; Bake, K. D.; Pomerantz, A. E. Chemical, Molecular, and Microstructural Evolution of Kerogen during Thermal Maturation: Case Study from the Woodford Shale of Oklahoma. *Energy Fuels* **2018**, *32*, 4859−4872.
(35) Takeda, N.; Asakawa, T. Study of petroleum generation by pyrolysis—I. Pyrolysis experiments by Rock-Eval and assumption of molecular structural change of kerogen using ^{13}C-NMR. *Appl. Geochem.* **1988**, *3*, 441−453.
(36) Manka, M. J.; Brown, R. L.; Stein, S. E. Flow ESR and Static Studies of the Decomposition of Phenyl-Substituted Ethanes. *J. Phys. Chem.* **1985**, *89*, 5421−5427.
(37) Behar, F.; Lorant, F.; Lewan, M. Role of NSO Compound during Primary Cracking of a Type II Kerogen and a Type III Lignite. *Org. Geochem.* **2008**, *39*, 1−22.

https://dx.doi.org/10.1021/acs.energyfuels.9b03851
Energy Fuels XXXX, XXX, XXX−XXX

Paper 2: Molecular Weight Distribution of Kerogen with MALDI-TOF-MS

Fuel 269 (2020) 117452

Contents lists available at ScienceDirect

Fuel

journal homepage: www.elsevier.com/locate/fuel

Full Length Article

Molecular weight variations of kerogen during maturation with MALDI-TOF-MS

Hyeonseok Lee[b], Arash Abarghani[b], Bo Liu[a], Mohammadreza Shokouhimehr[b,c,*], Mehdi Ostadhassan[a,*]

[a] Key Laboratory of Continental Shale Hydrocarbon Accumulation and Efficient Development, Ministry of Education, Northeast Petroleum University, Daqing 163318, China
[b] Department of Petroleum Engineering, University of North Dakota, Grand Forks, ND 58202, United States
[c] Department of Materials Science and Engineering, Research Institute of Advanced Materials, Seoul National University, Seoul 08826, Republic of Korea

ARTICLE INFO

Keywords:
Kerogen
Organic matter
Bakken
MALDI-TOF
Molecular weight distribution (MWD)
FTIR
EOR

ABSTRACT

Kerogen is an amorphous organic matter (AOM) in fine grain sediments, which produces petroleum and other byproducts when subjected to adequate pressure and temperature (deep burial conditions). Chemical characteristics of kerogen by considering its biogenic origin, depositional environment, and thermal maturity has been studied extensively with different analytical methods, though its molecular structure is still not fully known. In this study, conventional geochemical methods were used to screen bulk rock aliquots from the Bakken Shale with varying thermal maturities. Organic matter was isolated from the mineral matrix and then a mass spectrometry method was utilized to quantify molecular weight distribution (MWD) of four different kerogens at various thermal maturity levels (immature to late mature). Furthermore, to complement mass spectrometry, Fourier transform infrared (FTIR) spectroscopy was employed as a qualitative chemical and structural investigation technique. The MWD of four samples was obtained by matrix-assisted laser desorption/ionization time-of-flight (MALDI-TOF) mass spectrometry, and the results are correlated with the absorption indices (CH_3/CH_2 ratio and aromaticity) calculated from the FTIR attenuated total reflectance (ATR) method. The results showed when the degree of maturity increases, the aliphatic length shortens, and the branching develops, as well as the aromatic structure becomes more abundant. Moreover, based on the MWD results, higher maturity kerogen samples would consist of larger size molecular structures, which are recognized as more developed aromatic, and aliphatic branching stretches. The combination of infrared spectroscopy (AFT-FTIR) and mass spectrometry (MALDI-TOF) provided MWD variations in organic matter samples as a function of maturity based on varying absorption indices and revealed the rate of change in molecular mass populations as a function of thermal maturity in a type II kerogen.

1. Introduction

In the past few years, there has been growing attention to organic-rich shale reservoirs due to their importance in hydrocarbon production and CO_2 sequestration [1,2]. The high abundance of total organic carbon (TOC) in shale layers, which are deposited in these rocks hundreds million years ago, would lead to the generation of oil and gas through thermal maturation. This process takes place due to the exposure of rocks containing organics to adequate temperature and pressure as the depth of burial increases. During this geologic process, the organic matter known as kerogen, which has a complex and amorphous molecular structure, breaks down and goes through a significant structural and compositional transformation [3,4].

Thermal maturity of organic matter is an important phenomenon that still requires further studies at the molecular scale from various perspectives to help us better explain this process [3] which enables us to better explain the phenomenon that'd generate hydrocarbons from the organic matter. In this regard, there has been a limited number of studies to investigate molecular structure of organic matter (kerogen) at different stages of thermal maturity using various spectroscopy methods such as: 13-C nuclear magnetic resonance (^{13}C NMR) [25], X-ray photoelectron spectroscopy (XPS), and X-ray absorption near-edge structure (S-XANES) [5], Raman [6], and infrared (IR) [7,26] spectroscopy. Even though these studies have clarified the structural evolution

* Corresponding authors at: Department of Materials Science and Engineering, Research Institute of Advanced Materials, Seoul National University, Seoul 08826, Republic of Korea (M. Shokouhimehr).
E-mail addresses: mrsh2@snu.ac.kr (M. Shokouhimehr), mehdi.ostadhassan@nepu.edu.cn (M. Ostadhassan).

https://doi.org/10.1016/j.fuel.2020.117452
Received 10 November 2019; Received in revised form 16 January 2020; Accepted 20 February 2020
Available online 03 March 2020
0016-2361/

of kerogen to some extent, this task still demands further analysis since kerogen has different biogenic origins (e.g., lacustrine and marine algae and plankton or terrestrial higher-order plants). One of the methods in better characterizing the molecular structure of organic matter during thermal maturation is measuring its molecular weight (MW) and relating that to the existing chemical compounds or functional groups at every stage of maturity.

Mass spectrometry (MS) technique has been widely utilized in biology [8] and chemistry [9] for decades to identify the molecular weight of various materials such as proteins and synthetic polymers, which is now extended to petroleum and fossil fuels arena. This being said, in the first attempt to characterize kerogen with MALDI by Li et al., [13], a relationship between the minimum laser power sufficient for activating the MALDI-ionization process and the thermal maturity level (reported in the age of samples) of kerogens, was established. This study was later continued by Herod et al. [14], where several isolated kerogens from various thermal maturities and mixed depositional environments (marine, lacustrine and terrestrial) were analyzed by MALDI-TOF-MS (Matrix-assisted laser desorption ionization-time of flight mass spectrometry). Authors found that spectra of isolated kerogens from 'younger' deposits (less mature or less buried) showed larger molecular mass distributions compared to the spectra obtained from extracts of older sediments. Furthermore, kerogen molecular weight estimation measured by MALDI-TOF was in agreement with the values obtained by conventional techniques, such as SEC-chromatograms [13,14]. The issue with these two studies that employed MALDI spectroscopy is that neither of them studied a single origin kerogen specimen, and there was a mixture of samples without a systematic maturity trend among them. The importance would be to reveal the rate of molecular weight alteration at specific thermal maturity stage and the rate of change in the population of molecular fragments, which is missing.

Recently, molecular weight of the organic matter that was artificially matured in a semiopen pyrolysis system to various levels of thermal maturities from Green River Shale Formation was quantified using various mass spectrometry methods including laser desorption laser ionization (L^2MS), surface assisted laser desorption ionization (SALDI) [10], and matrix-assisted laser desorption ionization (MALDI) [11,12]. Results showed a systematic change in molecular weights and correlation between elemental analysis and mass spectroscopy results. It should be mentioned that although chemical information that is provided by MALDI-TOF is considered accurate for both identification and in quantification of chemical substances in a material, it would be difficult to determine the existing functional groups (e.g. carboxyl/amide/carbonyl/methylene/methine functional groups), and non-degradable fractions in the studied compounds. This adds a drawback to MALDI-TOF-MS, which makes it inevitable to be coupled with other analytical techniques such as IR, Raman or nuclear magnetic resonance (NMR) spectroscopy, as was done on these limited studies of kerogen, to provide us more detailed information about the components and materials that are being analyzed [15].

In this study, four isolated (extracted) kerogens from the mineral matrix at four different stages of natural thermal maturity (immature to late mature) from the Bakken Shale were examined by MALDI-TOF-MS combined with FTIR spectroscopy for molecular weight quantification along with chemical and structural analysis. This study enabled us to identify structural characteristics of organic matter as it undergoes thermal advance in nature to relate these variations to both qualitative information from chemical structures and quantitative molecular weight distributions (MWD). Additionally, the outcome helps us to delineate the rate of change in molecular weight intervals populations as thermal maturity progresses.

Table 1
Properties of Four Kerogen Samples (type II).[a]

Sample No.	T_{max} (°C)	TOC (wt %)	HI (mg/g C)	SBRo (%)
A	428	14.56	569	0.33
B	432	15.76	531	0.49
C	449	12.69	260	0.72
D	452	16.36	171	0.94

[a] The values were examined by the solid bitumen reflectance (%SBR_o) and Rock–Eval 6 derived parameters including Tmax, TOC (Total organic carbon), and HI (hydrogen index).

2. Materials and methods

2.1. Samples

Kerogen samples (type II representing a marine environment) were collected from the Bakken Formation which is one of the largest unconventional shale oil plays in North America and is currently being studied for potential CO_2-EOR and sequestration [16,17]. Samples were retrieved from four different wells that are drilled at different locations in the Williston Basin in ND, where the Bakken has different thermal maturities. Aliquots of the bulk samples were examined with programmed pyrolysis (Rock Eval 6) for determining the thermal maturity level of the samples. To be more accurate, samples were also analyzed for the solid bitumen reflectance in the absence/scarcity of the vitrinite maceral, and the measured values then converted to the equivalent vitrinite reflectance using the appropriate conversion equations. Results are summarized in Table 1, where it shows sample A is immature and sample D is late mature. To perform MALD-TOF analysis, which is done on isolated organic matter, first rock pieces are crushed and then washed to remove all contaminations and then submerged in concentrated 37% HCl. This is followed by placing samples in concentrated 48% HF. In the next step, the samples are placed into concentrated HCl for the second time. Using acid will ensure removal of all inorganic minerals including carbonates and silicates. Finally, centrifugation is done to create the kerogen slide and separates insoluble organic matter in the solid form the organic solvents [18,19] a process necessary prior to the mass spectrometry experiments.

2.2. ATR-FTIr

Infrared spectra of kerogen samples were recorded in adsorption between 450 and 4000 cm^{-1} wavelengths using a Thermo Fisher Scientific, Nicolet iS50 FTIR Spectrometer. Four kerogen samples were pulverized using a ball mill before the characterizations. Fourier transform infrared (FTIR) spectroscopy using attenuated total reflectance (ATR) was utilized to analyze the isolated kerogens. Unlike transmittance FTIR, ATR does not require that kerogen samples to be mixed with potassium bromide and form into pellets under high pressure, which reduces the time needed to prepare the samples. Kerogen samples were placed in contact with an internal reflection material, and IR spectra were obtained based on the excitation of the molecular vibrations of chemical bonds by the absorption of light. The stretching absorption of a vibrating chemical bond is observed at higher frequencies (wavenumbers) than the corresponding bending or bond deformation vibrations [22,23]. Although the bending vibrations can support to obtain more details from the chemical structure, we'd face limitations in the analysis of integrated bands in bending vibration areas because kerogen is a complex macromolecule. In this study, it was decided to analyze the C–H set of stretch vibrations that are observed in kerogen samples, which is also done in previous studies [7,26]. It should be noted that recorded bands of the absorption were identified through comparison with the published spectra shown in table 2.

Table 2 presents the stretching absorption for C–H stretch vibrations for methyl (–CH_3), methylene (> CH_2), and aromatics (C–H). These are

Table 2
Saturated aliphatic group and aromatic ring group frequencies [23].

Origin	Group frequency (cm^{-1})	Functional Group/ Assignment
Methyl (–CH_3)	2970–2950	Methyl C–H asymmetric stretch
	2880–2860	Methyl C–H symmetric stretch
Methylene (> CH_2)	2935–2915	Methylene C–H asymmetric stretch
	2865–2845	Methylene C–H symmetric stretch
Aromatic (C–H)	3130–3070	Aromatic C–H stretch

the most common characteristics of an organic compound containing the aliphatic fragments. The intensities observed are corresponding to the asymmetric and symmetric stretching and bending of the C–H bonds of the central carbon atom. The C–H stretching vibrations for the saturated aliphatic and the aromatic ring occur between 2800 and 3000 cm^{-1} and 3070–3130 cm^{-1} bandwidths, respectively. Acquired spectra were analyzed in order to evaluate the IR structural properties [24,26] utilizing the Gaussian curve functions to attain the best possible statistical reconstruction of the evaluated peaks. CH3/CH2 and aromaticity index were calculated utilizing the integrated area under the peaks. In this regard, the CH3/CH2 ratio was computed based on the ratio of the asymmetrical CH3 stretching (2970–2950) to the asymmetrical CH2 stretching (2935–2915). This ratio indicates the average chain length of aliphatic and the degree of chain branching where the lower ratio values indicate the longer aliphatic chains and a lower degree of branching and therefore the high potential for oil generating. Furthermore, the aromaticity index was calculated based on the ratio of the aromatic C–H stretching to the summation of asymmetrical CH3 and CH2 stretching {(3130–3070)/(2970–2950) + (2935–2915)} which is representing the degree of aromatic structures to aliphatic chain structures [7,26,27]. These ratios were considered to better analyze MWD that is acquired by MALDI-TOF at different stages of maturity and were related to the variations in the overall molecular weight of the specimens.

2.3. Maldi-TOF-MS

The AB SCIEX TOF/TOF 5800 mass spectrometry system was used for the identification and relative quantitation of kerogen molecular weight. A dilution series of kerogen powder were prepared for two different test setups, in the absence and the presence of the matrix. In the second set up where the matrix is presented, dilutions were mixed with α-Cyano-4-hydroxycinnamic acid (α-CHCA) in 1:1 ratio. The matrix, α-CHCA, is commonly used in conjunction with organic molecules, particularly for relatively higher-weight ones [28]. Each sample (1 μL) was spotted onto a standard stainless steel plate and allowed to air-dry. Spectra were acquired with MS reflector mode for 1000 shots, and the analysis was conducted over a range of 60 to 5000 Da by use of an adjusted accelerating voltage.

It should be noted that MALDI-TOF-MS analysis has been utilized to characterize kerogen in a very limited scope. However, previous studies conducted on heavy fossil fuels and aromatic compounds have demonstrated the applicability of MALDI-TOF to characterize similar macromolecules [11,12]. These studies suggested that the matrix would not always be necessary to obtain MALDI mass spectra, because lower molecular weight aromatics, can play the role of the matrix for the ablation of the higher molecular weight compounds. Even though suggestions have been made regarding the matrix, its role in the analysis of kerogen has not yet fully understood. Therefore, in our study, the MALDI-TOF spectrum of kerogen samples at various maturations is obtained in the absence and presence of the matrix, and the results are compared and reorganized to delineate the MWDs more accurately and help us investigate the necessity of having a matrix.

In order to confirm accurately the compound measurements validating the technique, we performed control procedures for MALDI-TOF [29,30]. MS technique is possible to detect varying components (fragments) of a complex structure. Hence, we made a 1:1 and 1:1:1 mixture of model compounds including kerogens spanning the mass range occurred for kerogen samples. Then, we checked that MALDI can detect all of these model compounds with about the same cross-section, and that the results give a spectrum with peaks regarding references and kerogens. Additionally, we confirmed that the measured molecular weight (WD) is not adjusted changed by the laser pulse energy. Furthermore, to find optimum laser power for kerogen samples, multiple tests with model compound were performed to obtain clear and exact signals. As a result, we set the laser intensity at 5000 (instrument-specific units) for the case when matrix is absent and at 4200 for the presence of matrix which provided us with consistent spectra.

3. Results and discussions

Since kerogen consists of amorphous and complex chemical compounds, spectroscopy analysis would be inadequate to evaluate its chemical structure quantitatively. As a result, in this study, FTIR and MALDI-TOF-MS are integrated, to assist the chemical characterization of this geo-macromolecule. We have interpreted spectra obtained from several extracted kerogens at different stages of thermal advance to reveal the relationship between various functional groups and molecular weight distributions and chemical alterations in a type II kerogen.

3.1. Structural characterization by FTIR

Considering the FTIR intensities, a given absorption band that is assigned to a specific functional group has a direct relationship with the amount of that functional group overall existence in the structure of the macromolecule [23]. We noted that the methyl group (CH_3) is considered as the terminal for the aliphatic chain, where a methylene group (CH_2) is linked to a neighboring group which can also be attached to another methylene group. This framework presents a carbon to carbon bond, forming the aliphatic chain. Because each section of this group has its corresponding C–H stretching and bending vibrations, identification of this group and skeletal frequency would help to estimate a carbon-based organic compound such as the kerogen. Especially, a strong methylene band (2935–2915 cm^{-1}) and a weak methyl band (2970–2950 cm^{-1}) indicates a longer-chain aliphatic structure. In contrast, the strong methyl band and a comparatively weaker methylene band indicate shorter-chain branching.

Fig. 1 represents the intensities measured for frequency absorptions assigned to methyl, methylene, and aromatic on a relative basis in the spectrum of each kerogen samples. The reason for the overlapped original spectra is due to the same amount of energy required for various vibrations [23]. To analyze each functional group at desired frequencies, the FTIR spectrum area from 2700 to 3200 cm^{-1} was fitted (Fig. 2). In order to do so, intensities and frequencies of the bands in the desired regions were estimated by curve fitting where the peak separation and quantitative calculation were performed using the Fourier self-deconvolution method.

Here, we examined the C–H stretching band intensities for CH_3, CH_2 and, aromatic ring CH-based that was obtained from the deconvolution results. CH_3/CH_2 ratio and the aromaticity indices were calculated based on the relationships that were stated earlier. Considering CH_3/CH_2 ratio, smaller values (sample A) implies comparatively longer and

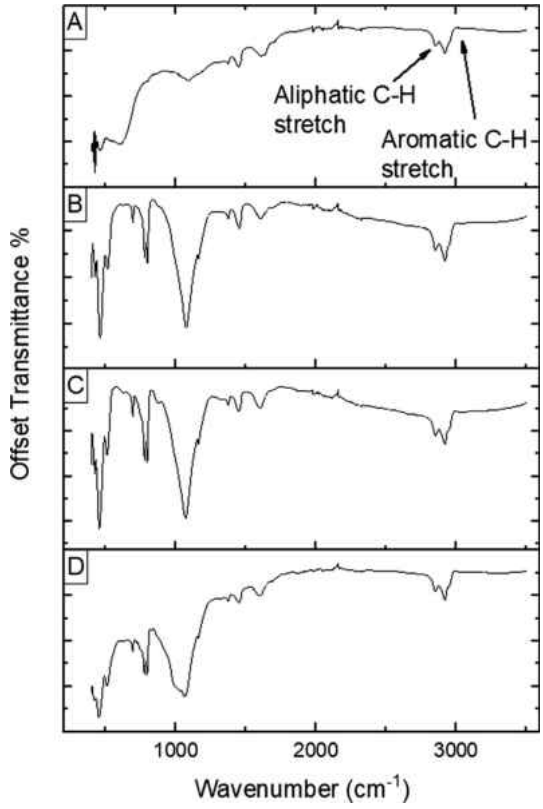

Fig. 1. FTIR spectra of four kerogen samples with varying maturity.

straight chains, whereas larger values (sample D) means shorter and more branched chains (Fig. 3-Left). In other words, when kerogen thermal maturation is advanced, relatively, the aliphatic chain length will become shorter, and branching is developed. As a result, the aromaticity index (Fig. 3-Right), representing the abundance of aromatic structures in the kerogen molecule is also increased as thermal maturity is increased. Furthermore, at a higher degree of thermal maturation where the abundance of aromatic rings and the reduction of methyl/methylene is observed, it is expected this phenomenon to result in a significant change in the molecular weight of the remaining substance. The observed trends in Fig. 3 are consistent with the results from previous findings, which proved that the aliphatic chain lengths have shortened and increased aromaticity during the maturation [7]. It should be stated again during the maturation process, as a result of organic matter exposure to temperature, hydrocarbons are generated and expelled from the organic matter and the remaining molecule is undergone major molecular alteration as being investigated here.

3.2. Molecular characterization by MALDI-TOF MS

The ionization process in MALDI-TOF proceeds through the capture of a proton, which forms a charged adduct with the molecular species of the sample. As the number of charged adducts reflects the signal intensity of the molecular weight, quantitative MWD analysis of any chemical compound is conducted. Four kerogen samples of this study were analyzed by MALDI-TOF to attribute maturation effects on the MWD of organic matter. Furthermore, systematic naturally matured kerogens with single biogenic origin have rarely been researched with MALDI-TOF, which limits the guidelines for an optimal and effective matrix selection based on the literature. Hence, in our study, kerogen samples were examined in both the presence and in the absence of the matrix (α-CHCA) for comparison and more accurate results.

Fig. 4 exhibits the mass spectra of kerogen samples obtained both in the presence and in the absence of the matrix. In all of these spectra for the presence of the matrix, unidentified high-intensity signals were observed in the relatively low-mass region between 200 and 400 *m/z*. Also, we could not find a regular ionization and pattern overall. This confirms that kerogen does not have a specific chemical structure and contains various functional groups which are differently ionized, which hinders the signal interpretation from analyzing molecules in kerogen. Also, overall spectra representing the samples in Fig. 4 does not show a particular relationship with signal intensities unlike polymers and proteins. However, we found that signal intensity changes with respect to the degree of thermal maturation. As a result of this alteration in the intensity, it is conclusive that the maturation process would change the molecular structure of kerogen in terms of the molecular mass of the organic matter. This infers that the chemical structure of kerogen has been evolved while bond-breaking and forming have occurred [31]. Thus, we can at least conclude that MALDI result confirms the chemical structure changes by maturation. Sample A, the immature kerogen, exhibits signals between 250 and 350 *m/z* with the highest intensity regardless of the presence or absence of the matrix. In addition, when the maturation is progressed, strong signals become evident in the presence of the matrix, near 170 *m/z* and 370 *m/z*.

On the other hand, in the absence of the matrix, the highest intensity signals are recorded in the similar mass region in all maturation stages, while molecular alterations have occurred in the higher mass region of the spectra. When the degree of maturation is higher, it was seen that signals become more transparent in the relatively heavier mass regions. This observation was not quite similar to the changes of signals in the presence of the matrix. In the latest experimental conditions, the spectra do not display any clear signals over 800 *m/z*. Therefore, it is probably understood not only that α-CHCA is not the best matrix to investigate complex mixtures of organic matter (kerogen) for the higher mass regions, but also that an excess of matrix inhibits to precisely conduct the ionization process. Based on this, in our study, the mass spectra without any matrix was utilized for the MWD analysis of the kerogen samples to avoid erroneous results.

Fig. 5 exhibits four molecular weight distribution (MWD) diagrams in separate intervals obtained from immature to late mature organic matters. Each independent value of four samples was created through the summation of the area under molecular weight signals based on the normalized spectra (Fig. 4). Furthermore, this particular partitioning (distribution) of MWs is decided through trying different molecular weight intervals and plotting MWDs of these four different samples when the most distinct and meaningful trends are delineated. We also note that the quantitative value in Fig. 5 disregards total MW and solely pertains to the comparative change of MWD regarding the maturity since the area ratio was adopted. It was found that, for relatively immature kerogen (A and B), around 60% of the signals are under 1 kDa range, whereas the majority of recorded signals for relatively higher maturity kerogen samples (C and D) are found between 1 and 2 kDa range. Immature sample (A) has the highest signal in the range under 500 Da; this indicates that relatively lighter molecular structures exist in kerogen compound prior to maturation. Meanwhile, the MWD for samples A and B continuously decreases in higher mass ranges. Remarkably, as the degree of the maturation increases, the higher signal distribution in the heavier range is observed in Fig. 5. It is verified that the MWD variation is certainly a function of the degree of thermal maturation, reflecting the existence of separate molecules detected through the MALDI-TOF-MS process. Although in all kerogen samples, the distributions are almost similar in the ranges over 5 kDa, generally higher maturity kerogens should contain larger size molecular compounds and fragments than lower maturity ones.

Additionally, the rate of change in MW is also investigated for each maturity stage over the entire range from 0 to 5 kDa. The smaller graph in Fig. 5 is obtained through taking the derivatives of integral of MALDI-TOF spectra to represent the rate of change in the quantity of that specific MW interval for each sample. The most important aspect of this graph is that at a specific MW (around 2.5 kDa) all of four samples

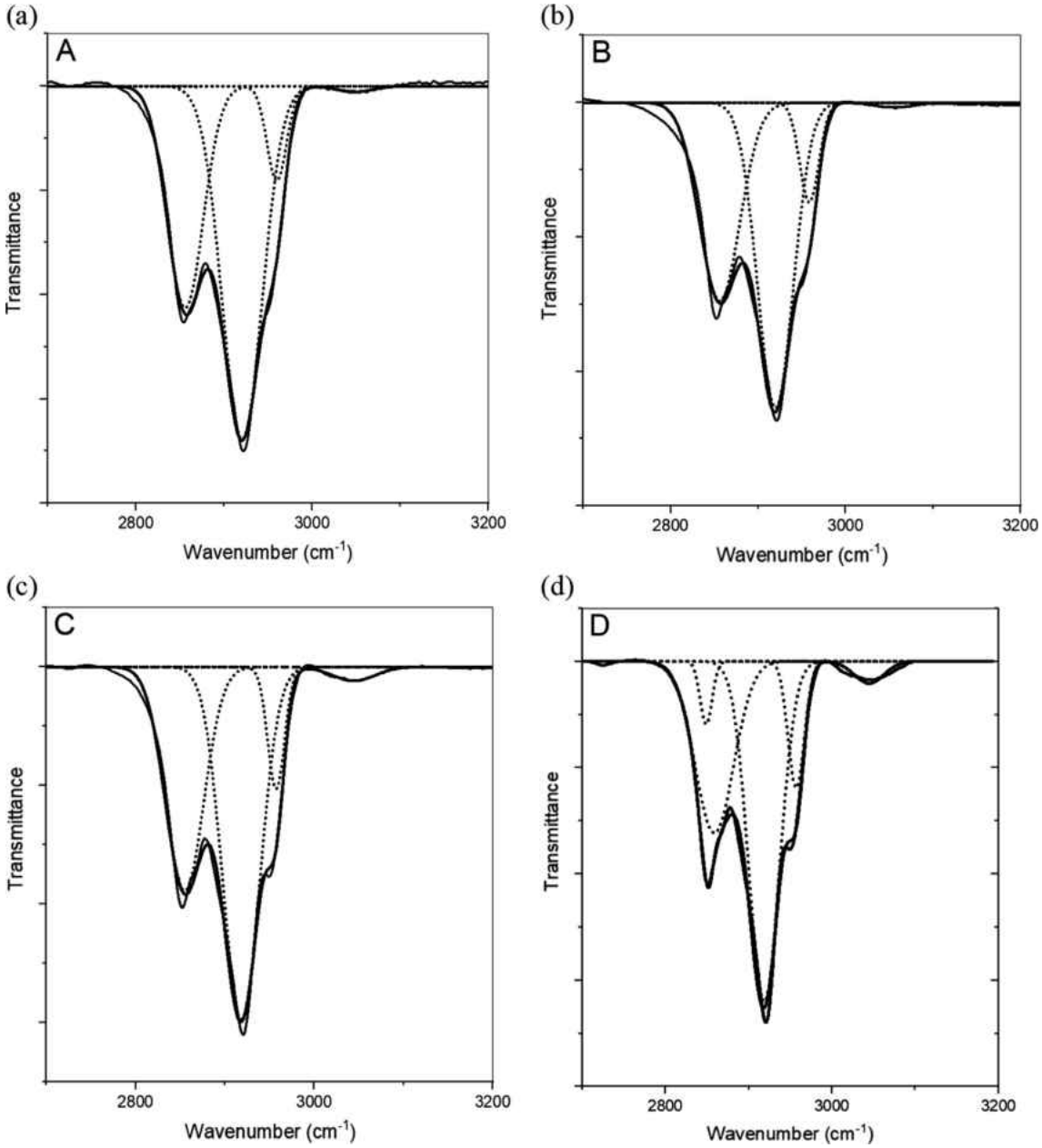

Fig. 2. Peak fitting results for the C–H stretch vibration area for samples A to D respectively. The black line is the original observed spectrum, while the solid line is the fitted spectrum. The coefficients of determination (R^2) of the peak fitting for the region 3200–2700 cm^{-1} in all spectra were between 0.998 and 0.994.

start to show relatively similar increasing trends in the rate of MW quantities, and then this becomes constant regardless of their maturity at higher MW region (> 4 kDa). This means there isn't any change in the molecule's population at higher weights regardless of the maturity. In sample A, the most immature kerogen, relatively large negative rate of change in the lower MW region is observed and the degree of change presents a decreasing trend as the molecular weight increases. The rate of change in sample B rapidly decreases up to around 1.5 kDa MW, then alleviates in higher MW ranges showing similar positive rate over 2 kDa similar to sample A. Unlike immature kerogens, two higher maturity specimens (C and D) have comparable MW rate of changes over the entire MW range. Positive change is observed near lower MW region (< 2 kDa), which means the molecules in 1–2 kDa are becoming more abundant than other MW regions, then the rate of popularity decreases and becomes unchanged like other samples. The difference in MWD and rate of change in MWs between the immature (A and B) and late mature (C and D) kerogens could refer to the boundary from pre-oil to oil generation window and to the phenomenon where hydrocarbons are generated and expelled from the OM through a nonlinear trend [21]. This major change in molecular structure corresponds to the onset of oil-window, when a major alteration is expected to take place (molecular structure and molecular weight) around 2.5 kDa where all MW rate of change graphs in the smaller image in Fig. 5 coincide and start to perform with a similar increasing trend. These two graphs combined illustrate, although we have a relatively linear increase in thermal maturity index (in Table 1) from samples, the variations are nonlinear which is at the onset of oil generation.

The MWD results can be correlated to the structural indices from the FTIR as well. As we discussed in this study, the carbon chain (aliphatic) length has shortened and branching has developed as the degree of maturation is increased, as well as the aromatic structure becomes more abundant. From Sample A to D, the abundancy in lower MW intervals decreases which corresponds to the increase in CH_3/CH_2 ratio. On the contrary, the higher quantity of heavier MW intervals is correlated to

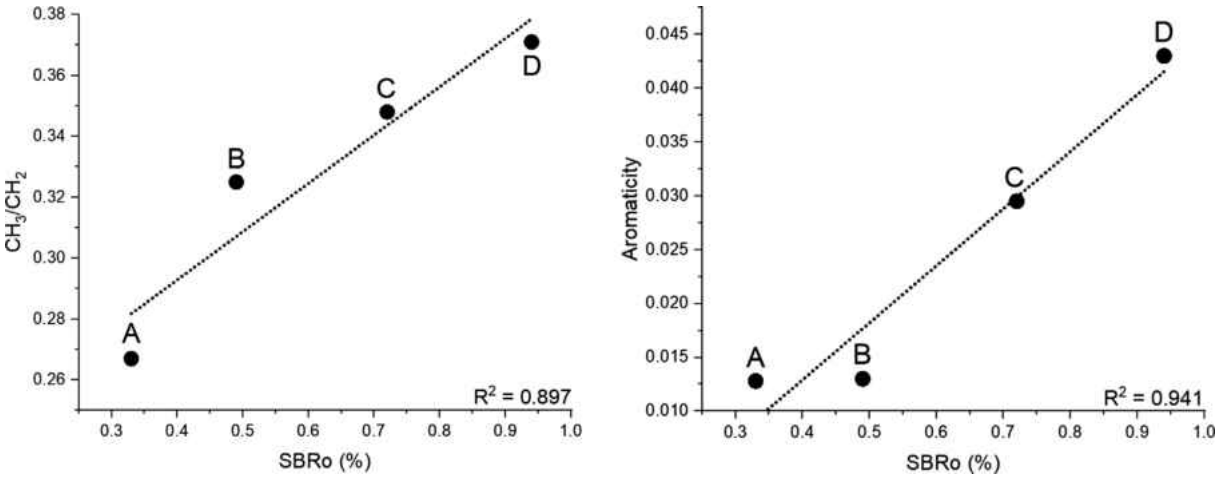

Fig. 3. Thermal maturity index (SBRo (%)) versus two major FTIR structural indices, (Left) CH_3/CH_2 and (Right) Aromaticity.

the aromaticity index where it increases from Sample A to D. These two combined, as a function of increasing the maturity, kerogen should contain a greater number of heavier molecules that are more developed aromatic and aliphatic branching structures. It should be noted that the trend observed here cannot directly convey the change of total weight of kerogen due to fragmentation of larger molecules. In order to provide the exact molecular weight of organic matter which is a large and complex macromolecule, a combination of mass spectrometry instrumentation and methods including MALDI, surface-assisted laser desorption/ionization (SALDI) combined with C and H NMR, and detailed elemental analysis would be necessary. Although this study did not delineate exact molecular weight of existing compounds and fragments in the samples but was able to explain molecular weight distribution and pertaining variations in MW of a single type (type II) kerogen during thermal maturation for the first time and the rate of such a change in a range of samples at various maturity levels. Therefore, it can be said that the structural changes that kerogen undergoes due to the abundance of the aromatic and shorten aliphatic chain length as its maturity progresses is well correlated with the heavier molecular weight of the product.

Ultimately, authors understand that thermal maturation that occurs in nature and sample selection from various locations can affect elemental structure, particularly the NSO content of the samples and overall results of the study. Hence, the best approach would be to artificially take an immature sample through pyrolysis in the lab and then perform all analysis on controlled samples. Though, this study was a preliminary approach to examine how MALDI-TOF can be used to evaluate MS of kerogen and other larger organic compounds.

4. Conclusion

This article presented a characterization of kerogen at 4 different maturity levels using infrared spectroscopy and mass spectrometry. Spectrums obtained by FTIR and MALDI-TOF from organic matters (kerogens) isolated from the bulk rock aliquots collected from the Bakken Shale were analyzed. The results were useful to better understand hydrocarbon generation and maturation process through investigation of a chemical structure and molecular weight variations during the expulsion of hydrocarbons as maturity progresses. Based on the results, the following conclusions can be made:

- MALDI-TOF spectra in the presence of the matrix (α-CHCA) show irregular ionization and pattern between 200 and 400 *m/z* for all maturity stages. It follows that kerogen does not have a specific chemical structure and hardly can be analyzed regarding its composition and molecular weights for specific fragments in the presence of the matrix. Since kerogen is a complex macromolecule, the matrix (α-CHCA) maybe inappropriate to be used during the ionization/mass spectroscopy experiments and existing lower MW aromatic fragments can take the role of the matrix.
- It was found while the increase in the maturation takes place, the results of MALDI-TOF in the absence of the matrix demonstrates that kerogen consists of heavier molecules. The result without the matrix shows obvious signals in the heavier mass regions (over 1000 *m/z*). Based on this, MWD was generated from MALDI-TOF spectra in the absence of matrix.
- The MWD variation provided different molecular weight ranges at different thermal maturity stages in the absence of the matrix. Relatively immature kerogens exhibited around 60% of the signals under 1 kDa range, with the strongest signals in the range under 500 Da, whereas the majority of signals of mature kerogens were found between 1 and 2 kDa range.
- In terms of major changes (molecular structure and molecular weight) through maturation, the boundary from pre-oil to oil generation window can be distinguished based on the rate of change of integrated MALDI-TOF signals with respect to molecular weight. After a specific MW (over 2.5 kDa), all kerogens would show a similar increasing trend in the rate of change of the population of MW intervals.
- The shorter aliphatic chain length and abundant aromatic structure are expected and delineated based on FTIR structural indices (CH_3/CH_2 and Aromaticity) when the degree of maturity increases which was correlated to the MWDs. The structural kerogen alteration in the abundance of the aromatic and shorten aliphatic chain length as its maturity progress tends to make the weight of molecules/fragments in kerogen heavier.

CRediT authorship contribution statement

Hyeonseok Lee: drafted the manuscript. Arash Abarghani: performed FTIR analysis and wrote that section. Bo Liu: analyzed MS spectroscopy and performed data interpretation. Mohammadreza Shokouhimehr: performed MS and FTIR analysis partially and reviewed the manuscript. Mehdi Ostadhassan: acquired financial support for authors and experiments, and designed the experiments, reviewed the manuscript and had oversight on data analysis and interpretation.

Acknowledgments

The authors wish to thank North Dakota Geological Survey, Core Library, for giving us access to the Bakken core samples, particularly Jeffrey Bader, director of the Core Library of North Dakota Geological

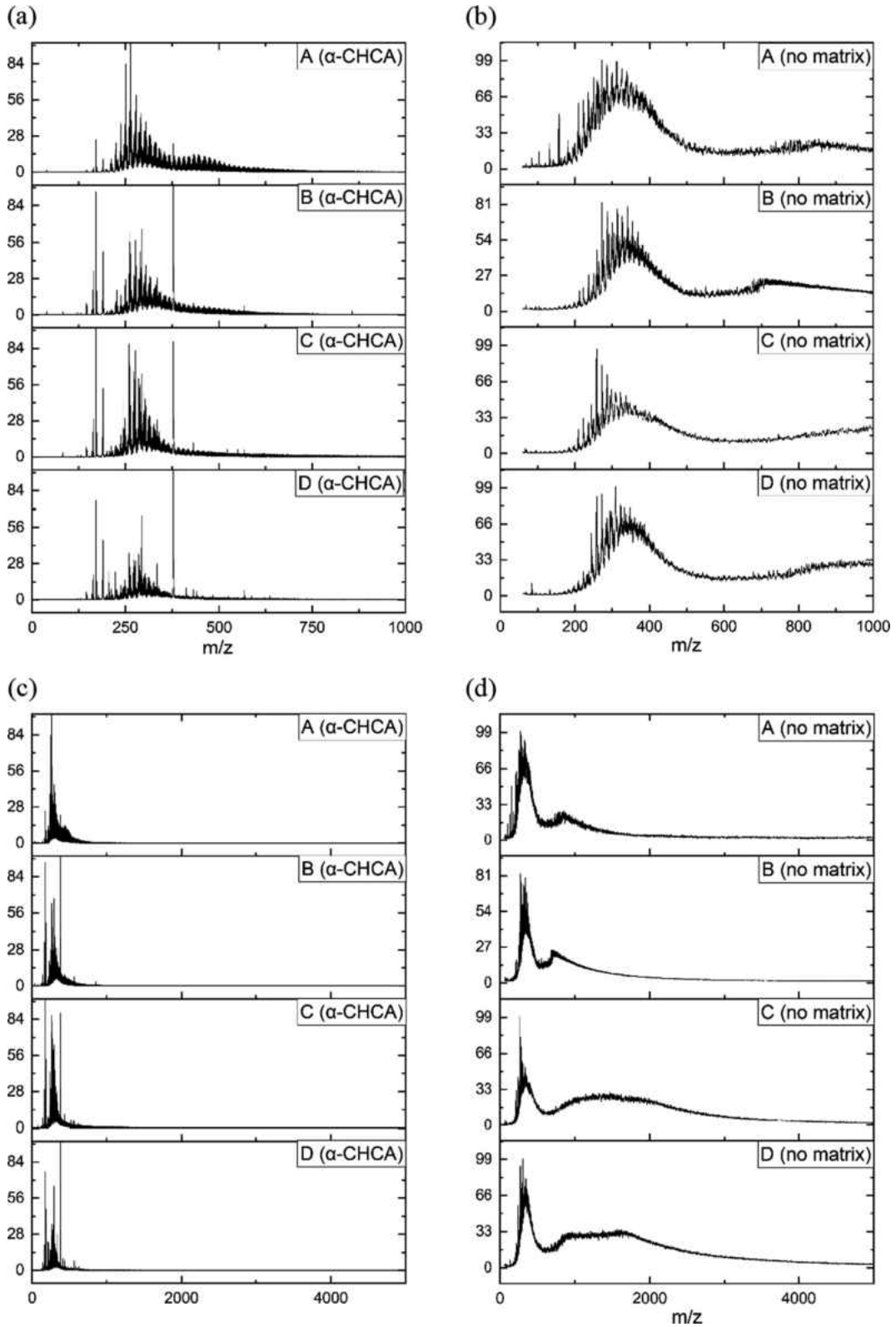

Fig. 4. Normalized MALDI-TOF spectra of kerogens in the order of increasing maturity from A–D (a and c) in the presence of the matrix (α-CHCA) and (b and d) in the absence of the matrix. The spectra are plotted over (a and b) a range of 60–1000 Da and (c and d) a range of 60–5000 Da.

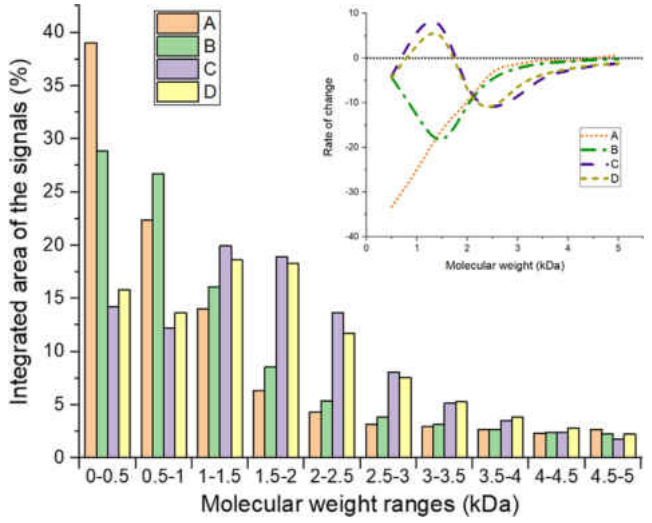

Fig. 5. Molecular weight distribution (MWD) diagrams of four samples presents different molecular weight ranges at different thermal maturity stages in the absence of the matrix. The relative areas of each sample are compared within the designated intervals. This specific MWD and intervals are used since this particular format showed the most distinct variation in MWs. The smaller image is based on MWD, rate of change (derivatives) of integrated MALDI-TOF signals with respect to molecular weight over the interval 0–5 kDa.

Survey, as well as Kent Hollands, lab technician. In addition, authors would like to express their gratitude to two respected reviewers and the editor, Dr. Suuberg for the time and review of this manuscript.

Appendix A. Supplementary data

Supplementary data to this article can be found online at https://doi.org/10.1016/j.fuel.2020.117452.

References

[1] Alvarado V, Manrique E. Enhanced oil recovery: an update review. Energies 2010;3:1529–75.
[2] Jia B, Tsau J, Barati R. A review of the current progress of CO2 injection EOR and carbon storage in shale oil reservoirs. Fuel 2019;236:404–27.
[3] Durand B. Sedimentary organic matter and kerogen. Definition and Quantitative Importance of Kerogen. Kerogen, Insoluble Organic Matter from Sedimentary Rock, Editions technips 1980, 13–34.
[4] Rullkötter J, Michaelis W. The structure of kerogen and related materials. A review of recent progress and future trends. Org Geochem 1990;16(4–6):829–52.
[5] Kelemen SR, Afeworki M, Gorbaty ML, Sansone M, Kwiatek PJ, Walters CC, et al. Direct characterization of kerogen by X-ray and solid-state 13C nuclear magnetic resonance methods. Energy Fuels 2007;21:1548–61.
[6] Khatibi S, Ostadhassan M, Tuschel D, Gentzis T, Bubach B, Carvajal-Ortiz H. Raman spectroscopy to study thermal maturity and elastic modulus of Kerogen. Int J Coal Geol 2018;185:103–18.
[7] Craddock PR, Bake KD, Pomerantz AE. Chemical, molecular, and microstructural evolution of kerogen during thermal maturation: case study from the woodford shale of Oklahoma. Energy Fuels 2018;32:4859–72.
[8] Cai Z, Liu S. Applications of MALDI-TOF spectroscopy; topics in current chemistry 331. Heidelberg New York Dordrecht London: Springer; 2013. p. 1–209.
[9] Marie A, Fournier F, Tabet JC. Characterization of synthetic polymers by MALDI-TOF/MS: investigation into new methods of sample target preparation and consequence on mass spectrum finger print. Anal Chem 2000;72:5106–14.
[10] Pomerantz AE, Le Doan TV, Craddock PR, Bake KD, Kleinberg RL, Burnham AK, et al. Impact of laboratory-induced thermal maturity on asphaltene molecular structure. Energy Fuels 2016;30:7025–36.
[11] Kim JG, Kim JH, Song B-J, Lee CW, Lee Y-S, Im JS. Empirical approach to determine molecular weight distribution using MALDI-TOF analysis of petroleum-based heavy oil. Fuel 2016;186:20–3.
[12] Edwards WF, Jin L, Thies MC. M ALDI-TOF mass spectrometry: obtaining reliable mass spectra for insoluble carbonaceous pitches. Carbon 2003;41:2761–6768.
[13] Li C-Z, Herod AA, John P, Johnson CAF, Parker JE, Smith GP, et al. Characterization of Kerogens by matrix-assisted laser desorption ionization mass spectroscopy. Rapid Commun Mass Spectrom 1994;8:823–8.
[14] Herod AA, Lazaro M-J, Rahman M, Domin M, Cocksedge MJ, Kandiyoti R. Matrix-assisted laser desorption/ionization time-of-flight mass spectrometry of kerogen extracts: effect of interactions between sample structure and matrix. Rapid Commun Mass Spectrom 1997;11:1627–34.
[15] Heroda AA, Lazaro M-J, Domin M, Islas CA, Kandiyoti R. Molecular mass distributions and structural characterization of coal derived liquids. Fuel 2000;79:323–37.
[16] Sorensen J, Braunberger J, Liu G, Smith S, Klenner R, Steadman E, et al. CO2 storage and utilization in tight hydrocarbon-bearing formations: a case study of the bakken formation in the williston basin. Energy Proc 2014;63:7852–60.
[17] Yu W, Lashgari H, Wu K, Sepehrnoori K. CO2 injection for enhanced oil recovery in bakken tight oil reservoirs. Fuel 2015;159:354–63.
[18] Khatibi S, Ostadhassan M, Tuschel D, Gentzis T, Carvajai-Ortiz H. Evaluating molecular evolution of kerogen by raman spectroscopy: correlation with optical microscopy and rock-eval pyrolysis. Energies 2018;11:1406.
[19] Abarghani A, Ostadhassan M, Gentzis T, Carvajal-Ortiz H, Bubach B. Organofacies study of the Bakken source rock in North Dakota, USA, based on organic petrology and geochemistry. Int J Coal Geol 2018;188:79–93.
[21] Abarghani A, Ostadhassan M, Gentzis T, Carvajal-Ortiz H, Ocubalidet S, Bubach B, et al. Correlating rock-Eval™ Tmax with bitumen reflectance from organic petrology in the Bakken formation. J. Coal Geol. 2019;205:87–104.
[22] Chen Y, Zou C, Mastalerz M, Hu S, Gasaway C, Tao X. Applications of micro-fourier transform infrared spectroscopy (FTIR) in geological science—a review. Int J Mol Sci 2015;16:30223–50.
[23] Coates. John interpretation of infrared spectra, a practical approach. Encyclopedia Anal Chem 2006. https://doi.org/10.1002/9780470027318.a5606.
[24] Lis GP, Mastalerz M, Schimmelmann A, Lewan MD, Stankiewicz BA. FTIR absorption indices for thermal maturity in comparison with vitrinite reflectance Ro in type-II kerogens from Devonian black shales. Org Geochem 2005;36:1533–52.
[25] Abdulla HAN, Minor EC, Dias RF, Hatcher PG. Changes in the compound classes of dissolved organic matter along an estuarine transect: a study using FTIR and 13C NMR. Geochim Cosmochim Acta 2010;74:3815–38.
[26] Washburn KE, Birdwell JE. Multivariate analysis of ATR-FTIR spectra for assessment of oil shale organic geochemical properties. Org Geochem 2013;63:1–7.
[27] Zodrow EL, D'Angelo JA, Helleur R, Šimůnek Z. Functional groups and common pyrolysate products of Odontopteris cantabrica (index fossil for the Cantabrian Substage, Carboniferous). Int J Coal Geol 2010;100:40–50.
[28] Beavis RC, Chaudhary T, Chait BT. α-Cyano-4-hydroxycinnamic acid as a matrix for matrixassisted laser desorption mass spectromtry. Org Mass Spectrom 1992;27(2):156–8.
[29] Pomerantz AE, Hammond MR, Morrow AL, Mullins OC, Zare RN. Two-step laser mass spectrometry of asphaltenes. J Am Chem Soc 2008;130:7216–7.
[30] Pomerantz AE, Hammond MR, Morrow AL, Mullins OC, Zare RN. Asphaltene molecular-mass distribution determined by two-step laser mass spectrometry. Energy Fuels 2009;23:1162–8.
[31] Takeda N, Asakawa T. Study of petroleum generation by pyrolysis—I. Pyrolysis experiments by Rock-Eval and assumption of molecular structural change of kerogen using 13C-NMR. Appl Geochem 1988;3:441–53.

Paper 3: Adsorption based realistic molecular model of amorphous kerogen

RSC Advances

PAPER

View Article Online
View Journal | View Issue

Cite this: *RSC Adv.*, 2020, **10**, 23312

Adsorption based realistic molecular model of amorphous kerogen

Hyeonseok Lee,[b] Farnaz A. Shakib,*[c] Kouqi Liu,[b] Bo Liu,[a] Bailey Bubach,[b] Rajender S. Varma,[e] Ho Won Jang,*[d] Mohammadreza Shokouhimher*[bd] and Mehdi Ostadhassan*[a]

This paper reports the results of Grand Canonical Monte Carlo (GCMC)/molecular dynamics (MD) simulations of N_2 and CO_2 gas adsorption on three different organic geomacromolecule (kerogen) models. Molecular models of kerogen, although being continuously developed through various analytical and theoretical methods, still require further research due to the complexity and variability of the organic matter. In this joint theory and experiment study, three different kerogen models, with varying chemical compositions and structure from the Bakken, were constructed based on the acquired analytic data by Kelemen *et al.* in 2007: ^{13}C nuclear magnetic resonance (^{13}C-NMR), X-ray photoelectron spectroscopy (XPS), and X-ray absorption near-edge structure (XANES). N_2 and CO_2 gas adsorption isotherms obtained from GCMC/MD simulations are in very good agreement with the experimental isotherms of physical samples that had a similar geochemical composition and thermal maturity. The N_2/CO_2 uptake by the kerogen model at a range of pressure shows considerable similarity with our experimental data. The stronger interaction of CO_2 molecules with the model leads to the penetration of CO_2 molecules to the sub-surface levels in contrast to N_2 molecules being concentrated on the surface of kerogen. These results suggest the important role of kerogen in the separation and transport of gas in organic-rich shale that are the target for sequestration of CO_2 and/or enhanced oil recovery (EOR).

Received 19th May 2020
Accepted 12th June 2020

DOI: 10.1039/d0ra04453a

rsc.li/rsc-advances

Introduction

The worldwide increase of energy consumption was accompanied by a shift of interest from conventional resources to the unconventional shale gas and oil[1] leading to continuous research and development on how to extract from these reservoirs[2,3] even though such reservoirs require more costly and advanced technologies to exploit.[4–6] In these reservoirs, organic matter or kerogen, which is the source of hydrocarbons,[7,8] is a major but poorly understood constituent compared to inorganic minerals. This is mostly because of the complexity in chemical composition, structure, and properties of kerogen which originates from its biogenic origin.[9] Kerogen, composed of mainly carbon, hydrogen, oxygen, nitrogen, and sulfur, experiences major structural and compositional changes as it undergoes maturation as a function of burial depth, *i.e.* pressure and temperature,[10] and finally breaks down to petroleum and other by-products. Maturation is a complex chemical transformation that encompasses free-radical mechanisms, causing the investigation of volumetric, thermodynamic, and stereochemical properties of porous kerogen to be a highly taxing process. Furthermore, the high submicron porosity of kerogen drastically impacts the storage and transport properties of the entire shale layer[1,7] and adds another layer of complexity to the investigation of this macromolecule. Therefore, building molecular models for kerogen is a much desired but challenging task, and not surprisingly, it has been continuously evolving with the advancements in computational methods.[8,11]

The first kerogen model was published by Burlingame *et al.* in 1968 which had focused on the study of the kerogen extracted from the Green River shale.[12] The suggested model did not represent a comprehensive chemical structure of the sample though, as it did not contain molecular topology. Later in 1995, Siskin *et al.* proposed an updated model for kerogen, particularly by adding the functional groups with oxygen and nitrogen.[13] Recent advancements in computational 3D modeling, drastically renewed the interest in exploring

[a]*Key Laboratory of Continental Shale Hydrocarbon Accumulation and Efficient Development, Ministry of Education, Northeast Petroleum University, Daqing 163318, China. E-mail: mehdi.ostadhassan@nepu.edu.cn*

[b]*Department of Petroleum Engineering, University of North Dakota, Grand Forks, ND 58202, USA*

[c]*Department of Chemistry and Environmental Science, New Jersey Institute of Technology, Newark, New Jersey 07102, USA. E-mail: shakib@njit.edu*

[d]*Department of Materials Science and Engineering, Research Institute of Advanced Materials, Seoul National University, Seoul 08826, Republic of Korea. E-mail: hwjang@snu.ac.kr; mrsh2@snu.ac.kr*

[e]*Regional Centre of Advanced Technologies and Materials, Faculty of Science, Palacky University, Šlechtitelů 27, 783 71 Olomouc, Czech Republic*

kerogen's molecular structure. Varying types of maturity models were introduced for kerogen by Ungerer *et al.* in 2015 (ref. 14) wherein they analyzed diverse kerogen types (based on their biogenic origin) grounded on a set of experimental data and PM7 semiempirical calculations as implemented in MOPAC.[15] In addition to the development of the molecular models for this purpose, the computational techniques have also become frequent tools for simulating the gas adsorption and desorption processes.[16–18] Simulation of adsorption behavior is important since organic-rich shales are becoming a repository of greenhouse gas storage which can also improve their productivity in CO_2 enhanced oil recovery (EOR) and sequestration.

The Bakken formation is one of the largest unconventional shale oil plays in North America and is currently being studied for potential CO_2-enhanced oil recovery and sequestration;[19] recent studies suggest that an injection of CO_2 into organic-rich shales can increase their production potential.[16,19] Hence, in order to precisely estimate the capacity of organic matter in terms of adsorption for sequestration and/or associated mechanisms for enhanced oil recovery, building a 3D molecular model of the Bakken kerogen has become imperative. Here, we report a new representative molecular model for organic matter from the Bakken (kerogen type II) based on previous experimental chemical compositional data.[20] We validate our models with gas (CO_2 and N_2) adsorption isotherms based on both experimental techniques and theoretical simulations. We also investigate CO_2 and N_2 diffusion behavior in the kerogen system to present a complete picture of interactions that would occur between kerogen and gas molecules.

Methods

Model preparation

A variety of methods can be utilized to provide the chemical composition of organic matter. While ^{13}C-NMR is used to examine the chemical structures and parameters related to carbon, the sulfur and nitrogen content are revealed through the X-ray absorption near-edge structure (XANES) analysis. The X-ray photoelectron spectroscopy (XPS) is capable of quantifying several functional groups in carbonaceous materials associated with carbon, oxygen, sulfur, and nitrogen.[21] This information can then be used to build a representative model of any organic material. Here, to build our molecular model of Bakken kerogen, we use the chemical and structural information of kerogen from diverse origins including Bakken, using ^{13}C-NMR, XPS, and XANES data as were reported by Kelemen *et al.* in 2007.[20] The Bakken organic matter is an immature (pre-oil window) type II kerogen representing a marine environment with T_{max} of 419 °C and hydrogen index (HI) of 580 mg g^{-1}.[20] The atomic ratios of carbon, hydrogen, sulfur, and nitrogen atoms were decided by considering the ^{13}C-NMR, XANES, and XPS analysis results. In particular, ^{13}C-NMR data were utilized for carbon and XPS/XANES for heteroatoms estimations to build the molecular model. From this data, around 35% of the total carbon concentration is included within aromatic structures that also contain nitrogen and sulfur, such as pyridine, pyrrole, and thiophene. The functional groups related to sulfur were set as sulfate and sulfoxide structures, while the oxygen-related functional groups were set as carbonyl and ether.

Throughout the text, the theoretical results obtained from our molecular model of the Bakken kerogen will be compared and contrasted to a set of experimental results from literature[20] plus two other sets of results that were collected from the Bakken (type II) and tested for gas adsorption in our lab. For the ease of comparison, we refer to the first set of experimental results as sample B1 and the other two as samples B2 and B3 (sampled at 8387 and 9814 feet in vertical depths, respectively). The geochemical characteristics of all these three samples, obtained from programmed pyrolysis,[22] are reported in Table 1. It can be seen from this table that the two B2 and B3 samples have the same T_{max} of 429 °C, and hydrogen index (HI) of 555 and 513 mg g^{-1}, respectively. Based on this analysis, we conclude that all of these three samples have similar chemical and physical properties and can equivalently represent the immature Bakken kerogen since they are all in the pre-oil generation window. Thus, while we used the data from sample B1 for building molecular models, we obtained the adsorption isotherm data from sample B2 and B3 to verify proposed molecular model.

Molecular model building

The construction of macromolecule kerogen models in this paper consists of the following major steps.

(a) First, the details of chemical composition including the nature and ratio of functional groups were determined through analyzing the experimental data reported by Kelemen *et al.*,[20] sample B1.

(b) Using this information, fragments of monoaromatic/polyaromatics moieties (benzene, pyrrolic, pyridinic, and thiophene) and functional groups (sulfate, sulfoxide, carboxylate, amino) and alkanes were built using molecular drawing software, Avogadro.[23] These fragments were built using General AMBER Force Field (GAFF) parameters.[24,25] The fragments contained the as accurate number of nitrogen, sulfur, and aromatic carbon atoms as possible based on the experimental data. The partial charges on all atoms were assigned by the Gasteiger–Marsili sigma charges[26] at the initial stage of the macromolecular model building. The nature of bridges (*e.g.* ketone and ether) between the fragments were assigned based on the sample analysis and were selected to satisfy the number of oxygen, and carbon atoms.

Table 1 Properties of the Bakken shale kerogen samples, all belonging to type II kerogen and in the pre-oil window (immature)

Property	B1[a]	B2[b]	B3[b]
T_{max} (°C)	419	429	429
HI (mg g^{-1})	580	555	513

[a] T_{max} and HI data of Bakken sample B1 were estimated by Kelemen *et al.*[20] [b] For Bakken sample B2 and B3, Rock-Eval pyrolysis was applied to quantify T_{max} and HI.[22]

(c) In designing aromatic fragments, ^{13}C-NMR data were used to find the percentage of protonated, non-protonated, and bridge carbons, where XPS results were used to obtain the ratio of nitrogen and sulfur-containing aromatic structure.

(d) In order to cross-link all of the prebuilt fragments, we used the "bond creation" feature of the LAMMPS package.[27] This feature can create bonds between specified atomic sites as a molecular dynamics (MD) simulation running, if the distance between the two atoms becomes less than a threshold value. As such, we carefully selected the bonding sites in the form of aromatic carbon (protonated, non-protonated) and oxygen-related fragments, because in that format they can better fit the designed model. The pre-built fragments were positioned in a rectangular simulation box using Packmol package.[28] Then, the cross-linkings between the fragments and bridges were generated during an MD trajectory that converged towards local equilibrium with GAFF force field parameters.[25,27]

(e) When the fragments were branched, conforming to the desired ratio of hydrogen to carbon atoms led to the creation of unpaired free radical sites. Therefore, the cross-linked fragments were inspected and improved maximally by adding or removing hydrogen or methyl groups. Thus, by trial and error process, we built the molecular model of kerogen that interweaves all of the constituent fragments within a single macromolecule.

Quantum mechanics calculations

To obtain the quantitative electrostatic properties and optimized geometries of our kerogen model, we performed quantum mechanical (QM) calculations using the ORCA package[29] based on the density functional theory (DFT) method. As DFT considered to be suitable for organic compounds, we ran our calculations at B3LYP/6-31G(d) method/basis set level.[30] Hirshfeld atomic population[31] analysis was carried out to obtain atomic partial charges since it is less basis-set dependent and can be derived for optimal partitioning of electron density. The partial charges obtained from the QM calculations replaced the initial partial charges which had been set without the polarization of atoms.

Gas adsorption and diffusion simulation (GCMC + MD)

Gas adsorption simulations were carried out using Grand Canonical Monte Carlo (GCMC) simulation, and gas diffusion simulations were utilized by Molecular Dynamics (MD) technique efficiently converging towards local equilibrium for diffusion equation. The equilibrium can be determined in the molecule configuration considering fluctuations in the internal energy and number of adsorbed molecules. We used a hybrid molecular simulation that consists of combining GCMC and MD to perform simulations implemented in LAMMPS package[27,32] (schematic illustration of the simulation system is shown in Fig. 1). At every time step of the simulation, we attempted both GCMC exchanges (insertions and deletions) and MC moves (translations and rotations), followed by MD simulation steps in the canonical ensemble at the constant number of molecules. This process allows the gas molecule

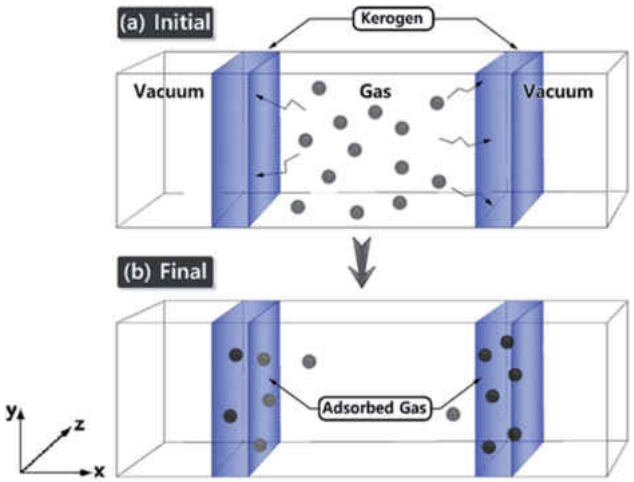

Fig. 1 Schematic illustration of the simulation system. (a) Initial gas adsorption/diffusion simulation set-up within the kerogen models. (b) The system becomes equilibrated and the gas molecules are diffused. Gas molecules are diffuse and adsorbed by driving force along the *x*-axis.

diffusion and kerogen model relaxation at each GCMC time step. Technically, every 100 GCMC insertion/deletion attempts followed by 200 MD time steps. In GCMC simulation, the chemical potential of the gas phase was related to the gas pressure using the ideal gas equation of state. The Metropolis algorithm was utilized to calculate the potential energy in the system and to control GCMC exchange or MC move. The gas adsorption and diffusion simulations were run for 5×10^7 MD steps and 2.5×10^5 GCMC cycles using a Nosé–Hoover thermostat to keep the temperature constant. The time step in all simulations was 1 fs.

Interactions were modeled by the sum of short-range Pauli repulsion and long-range electrostatic attraction embedded within Lennard-Jones potential with a cutoff distance of 10 Å using a particle–particle particle–mesh solver (PPPM).[33,34] The N_2 and CO_2 molecules were simulated using the TraPPE force field parameter set shown in Table 2,[35] which is useful for complex chemical systems with molecular simulation. In the TraPPE force field, CO_2 was modeled as a linear triatomic and N_2 as a diatomic molecule with fixed bond lengths and bond angles. These models are suitable for reproducing the densities and the diffusion of N_2 and CO_2 in bulk and surface phases at the conditions simulated in this work. The system was set in order to maintain a constant temperature of 77 K and 273 K which is the experimental gas adsorption temperatures and

Table 2 Parameters related to the adsorbates (CO_2 and N_2).[35]

Molecules	Atoms	Charge	σ (Å)	ε/k_B (K)
N_2	N	−0.482	3.31	36.0
	N-COM	+0.964		0.0
CO_2	C	+0.70	2.80	27.0
	O	−0.35	3.05	79.0

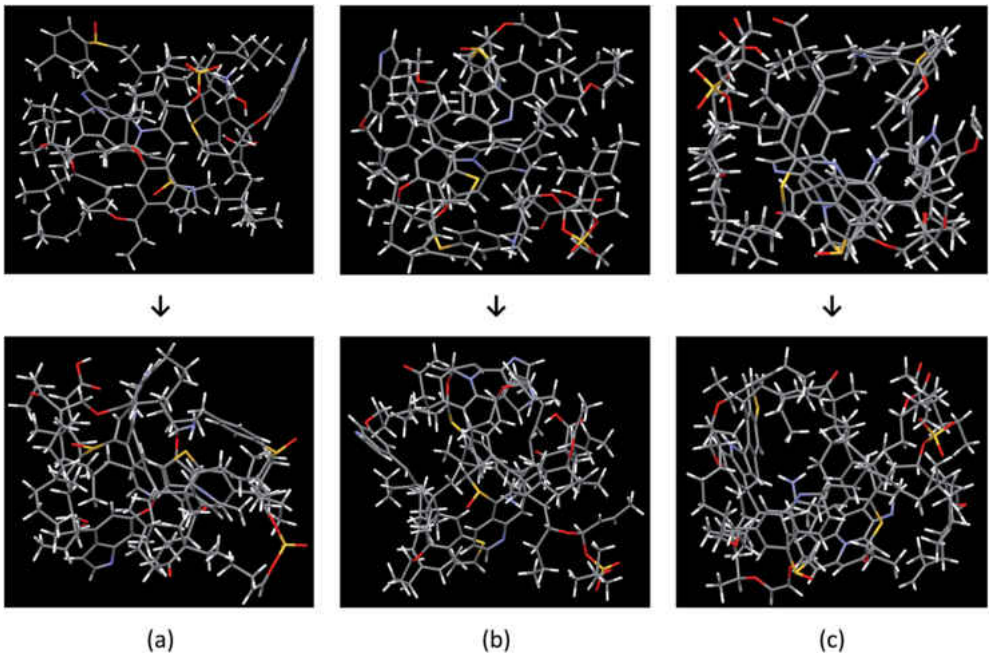

Fig. 2 Constructed and optimized Bakken kerogen model A (a), model B (b), and model C (c). Different geometric configuration and chemical compositions with the following color code, carbon: black; hydrogen: white; oxygen: red; sulfur: yellow and nitrogen: blue. (a) $C_{141}H_{187}N_6O_{15}S_4$, (b) $C_{152}H_{193}N_6O_{15}S_4$, and (c) $C_{158}H_{207}N_6O_{16}S_4$.

applied with the Nosé–Hoover thermostats. All partial charges of the kerogen models were obtained from QM calculations as explained in the previous section. At equilibrium, the number of gas molecules in the kerogen surface and bulk phase was kept constant.

Gas adsorption experiment

Gas adsorption experiments were performed on isolated kerogen from the bulk shale based on already established procedures.[36] Briefly, we collected the samples and removed the bitumen using a mixture of methanol and toluene. Then, we added HCl into the solid residue to remove carbonates. Subsequently, HF was added to remove the silicate minerals, and pyrite was removed by using $CrCl_2$, and finally, acid with dissolved inorganic minerals was separated from the organic matter by centrifugation.

After isolation from the rock matrix, the solid kerogen was degassed for at least 8 hours at 110 °C to remove moisture and volatiles, crushed (to less than 250 μm size) and loaded into the instruments. Low-pressure N_2 was measured on a Micromeritics® Tristar II apparatus at 77 K while CO_2 adsorption was performed on a Micromeritics® Tristar II plus apparatus at 273 K. The gas adsorption quantity was measured over the relative equilibrium adsorption pressure (P/P_0) range of 0.01–0.99, where P is the gas vapor pressure in the system and P_0 is the saturation pressure of N_2.

Table 3 Structural parameters relevant to carbons in the Bakken kerogen (sample B1 (ref. 20)) and the constructed models (A, B, and C)[a]

Structure	Sample B1	Model A	Model B	Model C
Aromatic	0.35	0.371	0.344	0.330
Carboxyl/amide/carbonyl	0.02	0.028	0.026	0.025
Protonated aromatic	0.17	0.180	0.180	0.140
Phenoxy/phenolic	0.02	0.021	0.021	0.021
Alkyl-substituted aromatic	0.08	0.064	0.064	0.070
Bridged aromatic	0.09	0.092	0.092	0.092
Aliphatic	0.63	0.61	0.63	0.64
Methylene/methine	0.46	0.44	0.45	0.48
Methyl/methoxy	0.15	0.12	0.12	0.13
Alcohol/ether	0.06	0.04	0.04	0.04
H/C ratio	1.22	1.32	1.27	1.31
Average density (g cm^{-3})	—	0.927	0.919	0.974

[a] The data presented here are ratio per 1 number of carbon.

Results and discussion

Bakken molecular models

The Bakken shale models were constructed and verified by analyzing experimental data coupled with computational techniques (molecular builder, quantum mechanics calculations, and Monte Carlo/molecular dynamics simulation). The models consist of a complicated mixture of chain and mesh structures. Fig. 2 visualizes the three molecular models, before and after the optimization process, which do not have the same chemical composition and structure. The final chemical compositions of models A, B, and C are $C_{141}H_{187}N_6O_{15}S_4$, $C_{152}H_{193}N_6O_{15}S_4$, and $C_{158}H_{207}N_6O_{16}S_4$, respectively.

Table 3 summarizes the aromatic carbons in the constructed models that were found compatible with ^{13}C-NMR data in

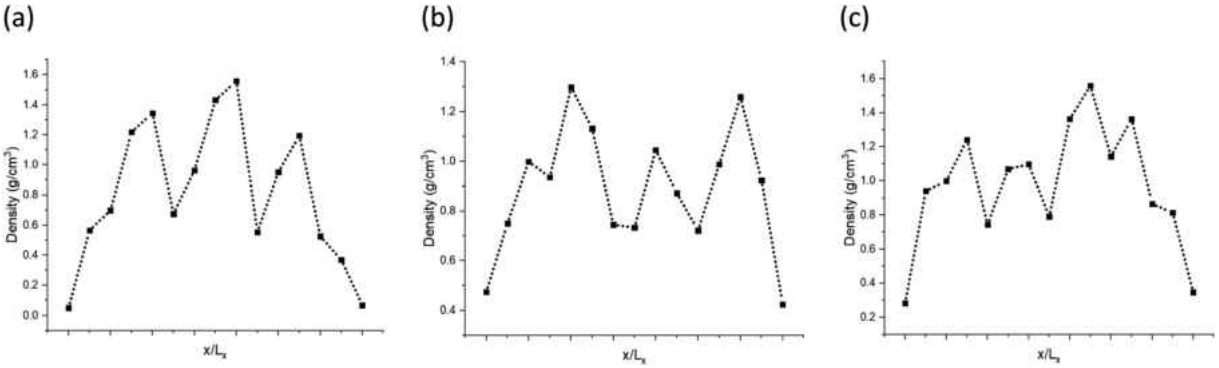

Fig. 3 Density (g cm^{-3}) profiles of the model A (a), B (b), and C (c) along the *x*-axis.

sample B1. Since aromatic carbons were set up at the initial stage of molecular model building, where aromatic fragments were prebuilt, carbons in aromatic structures are very close to sample B1 in regard to the structural parameters (*e.g.* protonated, non-protonated, and bridged carbon in aromatic structure). However, some discrepancies were detected such as the ratio of hydrogen to carbon atoms and methylene/methine structure. Because we improved the models by adding or removing methyl groups and hydrogens, it was not possible for every structure parameter of the models to meet the sample B1 perfectly.

The models have average densities between 0.92 and 0.98 g cm^{-3} (in Table 3) demonstrating density profiles along the *x*-axis around 1.6 to 0.1 g cm^{-3} (in Fig. 3). The density

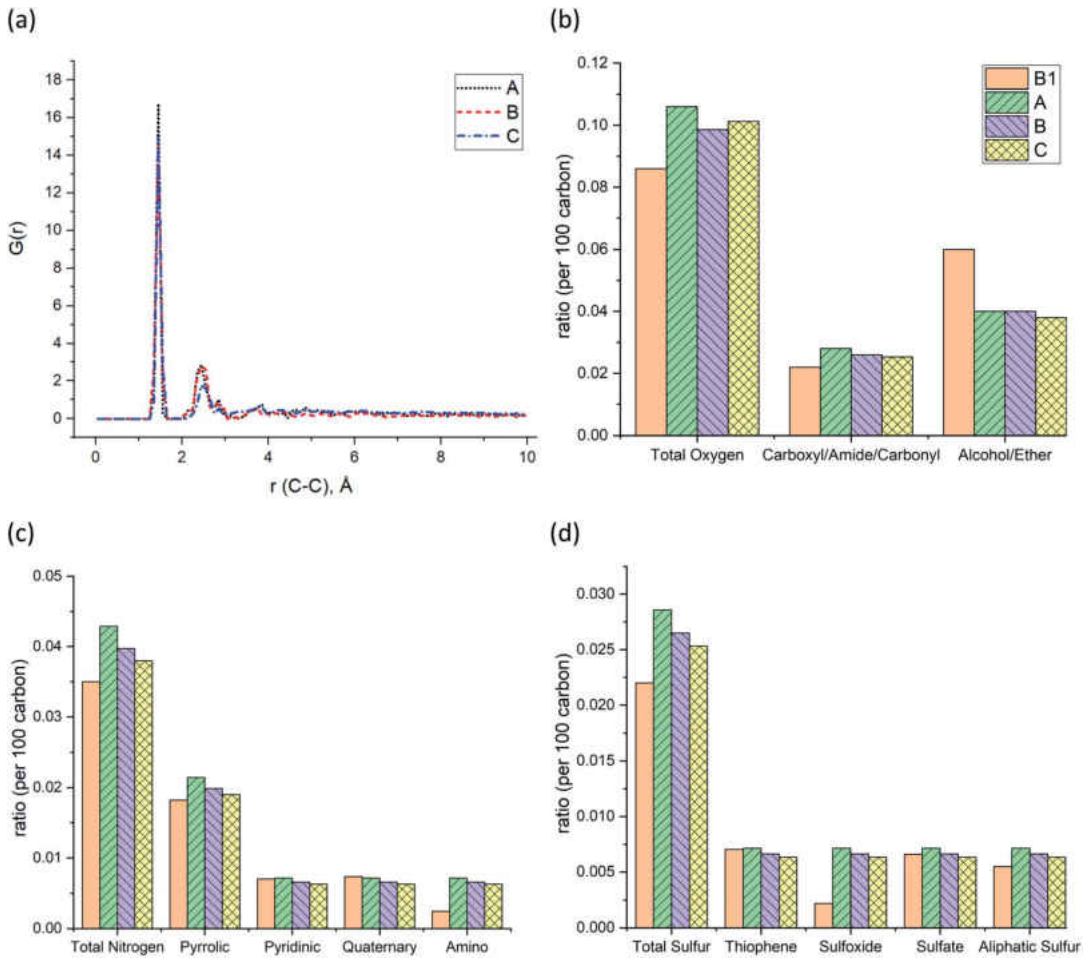

Fig. 4 (a) Pair distribution functions (PDF) or G(r) of the Bakken kerogen models. The comparison between sample B1 and the models in terms of (b) the ratio of oxygen-containing functional groups, (c) the ratio of nitrogen-containing functional groups, and (d) the ratio of sulfur-containing functional groups.

profiles of models exhibit that the generated kerogen structures are amorphous and the internal/external surfaces are rough at the sub-nanometer level in Fig. 3. Since gas molecules diffuse and adsorbed along the *x*-axis (Fig. 1), the gas molecules could heavily be affected this internal density of models.

The pair distribution function (PDF) profile, Fig. 4a, shows the probability of carbon existence at the distance *r* (Å) from another carbon, and it is exclusively related to carbon structure. The highest peak position is between 1.4 and 1.45 Å which represents aromatic carbons. Since almost 35% of the carbons in the models have an aromatic structure, this is the highest peak of all. The three models have similar peak positions with a similar width. Fig. 4b shows the comparison of the three models with sample B1 based on the total oxygen, *i.e.* carbonyl, ether, and alcohol groups per 100 carbons. It is apparent from this figure that the constructed models (A–C) contain a higher total number of oxygens per carbon than sample B1. It is the result of sample B1 having a higher number of ether and alcohol groups compared to the models but a similar ratio of carbonyl functional groups. It should be noted since the carboxyl and alcohol groups both contain –OH, the peak involving ether and alcohol groups could have been overlapped and intensified as a result, in the XPS spectrum.[20] This phenomenon has led to a higher amount of alcohol/ether as a result of the summation of carboxyl and alcohol with –OH group shown in Fig. 4b. Fig. 4c and d also indicate that both prebuilt aromatic fragments (pyrrolic, pyridinic, and thiophene) and the bridges (quaternary, sulfate, and aliphatic sulfur) have comparable ratio with sample B1. However, the ratio of amino and sulfoxide in the models are somewhat higher. Screening Fig. 4b–d, one can also find that all three models have a smaller percentage of oxygen, nitrogen, and sulfur atoms than the original input data from XPS of sample B1. Our macromolecule models of Bakken kerogen consist of around 150 carbon atoms due to the size limitation of the model building. This limited total number of atoms in the models is not enough to thoroughly represent the perfect ratios.

Gas diffusion/adsorption on the surface of kerogen

The ultimate goal of this study is to develop reliable amorphous kerogen molecular models. In order to verify the reliability of these models, here we compare and contrast the gas adsorption/diffusion simulation results of these models with the experimental gas adsorption isotherms that we have obtained from Bakken kerogen samples B2 and B3. We performed GCMC/MD simulations to investigate N_2 and CO_2 gas molecular adsorption on the surface of the models as well as their diffusion to the sub-surface levels. Apart from validating our models, because the three kerogen models cover a variety of structure and chemical composition and contain small size pore (<1 nm) that are irregularly spread all over the models, we expect that this study sufficiently clarifies the behavior of N_2 and CO_2 molecules through the small size pores of organic matter.

First, we focus on the results of adsorption/diffusion of N_2 molecules on/into three molecular models (A–C) and compare the results to the experimental N_2 adsorption isotherms of samples B2 and B3 in Fig. 5.

As can be clearly seen, samples B2 and B3 capture around 43.18 and 40.78 ($cm^3\ g^{-1}$ STP) of the N_2 gas, respectively, at 100 kPa and 77 K. N_2 molecules adsorption behavior with the model A and B (40.29 and 40.15 $cm^3\ g^{-1}$ STP, respectively) are fairly close to the two experimental samples. Meanwhile, the number of adsorbed molecules into model C (38.5 $cm^3\ g^{-1}$ STP) is almost 4% lower than both of the other two models and the experimental samples B2 and B3. We conclude that the difference of functional group distribution and internal density profile among the three models affects the adsorption of N_2 molecules on the kerogen surface and pores. For instance, the model C containing a larger ratio of aliphatic carbon structure, specifically more methyl groups, cannot provide adequate space for N_2 molecules for adsorption as much as the model A and B. The steric effect of the methyl groups may be the main reason preventing the attachment of N_2 molecules to the framework compared to the planar configurations of aromatic structures.[37]

Since the overall results of N_2 adsorption on the three models were close to the experiment, we clustered the three models for CO_2 gas adsorption and diffusion simulations. Packmol package was utilized to place one of each kerogen models (A, B, and C) in two sides of a feed compartment with the size of around 16 × 57 × 40 angstrom, as shown in Fig. 1. These two systems were then allowed to come to relaxation by running a 1 ps NVT molecular dynamics simulations. The final average density of the kerogen models compartment is 0.922 g cm^{-3}. Since the three kerogen models were simply adhered to one another and clustered, packing them in different modes was not considered. In this system, gaseous fluids would diffuse to two different surfaces of the clustered kerogen model. Unlike N_2 gas adsorption experimental conditions, CO_2 gas adsorption experiment, and accordingly theoretical simulations, were performed under a series of varying pressure values at 273 K (Fig. 6).

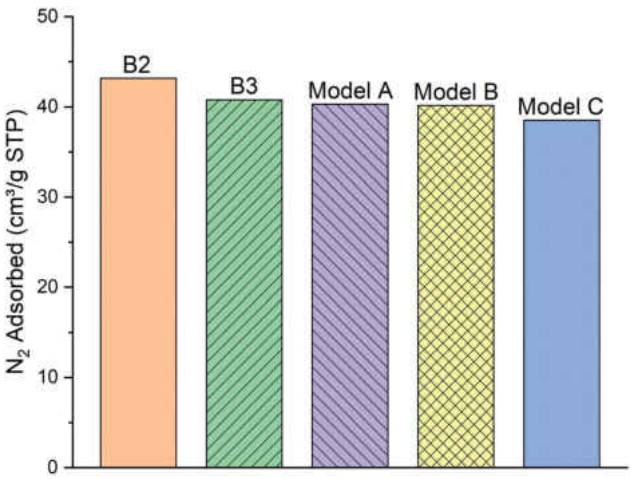

Fig. 5 The comparison of the simulated excess nitrogen (N_2) adsorption isotherms between the models (A–C) with experimental loadings (sample B2 and B3) at 100 kPa, 77 K.

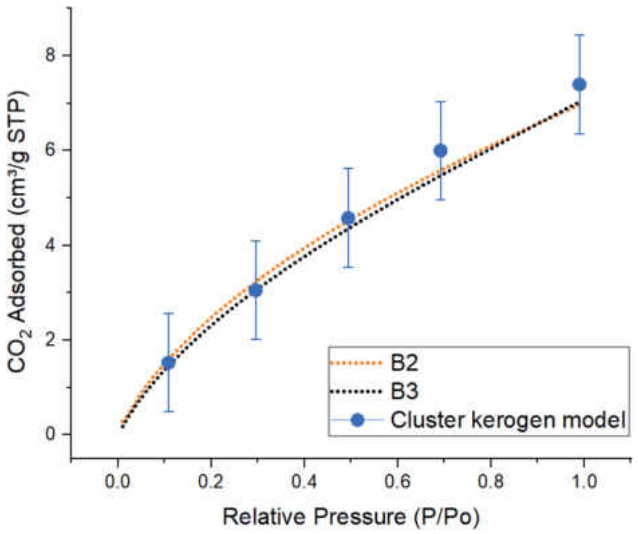

Fig. 6 Comparison of simulated excess CO_2 adsorption isotherms between the cluster kerogen model, blue dots, and the experimental samples B2, orange, and B3, black, at 273 K.

The result of CO_2 gas adsorption isotherms of the samples B2 and B3 show a nearly linear relationship of gas adsorption with respect to the pressure. The cluster model very closely follows this behavior and only slightly deviates at higher pressure. At lower pressure of 10, 30, and 50 kPa, the cluster model shows a total amount of adsorbed CO_2 molecules of 1.53, 3.05, and 4.58 $cm^3\ g^{-1}$ STP, respectively. These are very close to those of experimental samples B2 (1.59, 3.22, and 4.52 $cm^3\ g^{-1}$ STP), and B3 (1.45, 3.05, and 4.35 $cm^3\ g^{-1}$ STP). The small discrepancy, around 5%, between the cluster model and samples B2 and B3 occurs when the simulation and experimental pressures reach 70 kPa. This phenomenon can be explained due to the increase in chemical potential in the smaller pores. As the pore radius decreases, the overlapping potentials from the strong pore wall–wall interactions and the strong CO_2–wall interactions would lead to higher amounts of CO_2 molecules to get adsorbed in smaller pores compared to the larger ones.[38,39] Since the model hosts ultra-micro pores (0.3 nm to 0.7 nm) and larger number of CO_2 molecules are placed in a fixed system at higher pressures (larger number of CO_2 molecules in GCMC/MD simulation), it is observed that higher quantities of CO_2 are adsorbed on the pore surfaces. This is in contrast with how samples B2 and B3 that both contain meso (less than 3–5 nm) and ultra-micro pores performed. The results proclaim that the pore structure plays an important role in adsorption mechanisms as a function of pressure.

The simulated mass density profile in Fig. 7 shows that CO_2 and N_2 molecules have migrated to the kerogen model during the process and penetrated to the sub-surface levels of the model as well as being adsorbed on the surface. This simulation confirms that the interaction between gas (CO_2 and N_2) molecules and kerogen molecular models is strong enough to capture the molecules on or inside the models. Because the internal density of the model is irregular and highly densed subsurfaces are existed (Fig. 3), the gas molecules could be captured into these densed areas inside the kerogen model. In particular, CO_2 molecules show a much stronger interaction than N_2 such that a considerable number of CO_2 molecules penetrate to the sub-surface levels of the kerogen model. N_2 molecules, on the other hand, are mostly diffused in the bulk region with a smaller number of molecules detained on the surface of the kerogen model. These results demonstrate that kerogen can be used as a porous filter for optimal separation of CO_2 and N_2 gas molecules.

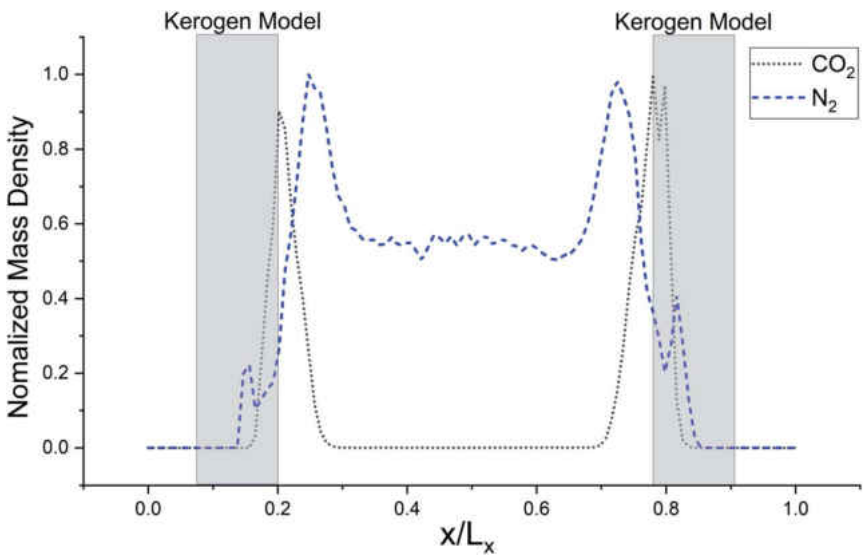

Fig. 7 Normalized mass density profile of CO_2 from clustered Bakken kerogen models at 100 kPa and 273 K, and of N_2 from kerogen model A at 100 kPa and 77 K from GCMC/MD simulation. This density profile shows that CO_2 and N_2 molecules are crowded near Bakken models at one million time steps.

Conclusion

In this work, we reported a molecular model for amorphous organic matter (kerogen) built based on experimental constraints. The numerical analysis of the kerogen by the methods ^{13}C-NMR, XPS, and XANES was used to determine the chemical composition and structure of three different models. GAFF parameters combined with partial charges computed *via* quantum mechanics calculations were used to build a more realistic model. GCMC and MD simulations were run to compute N_2 and CO_2 gas adsorption isotherms on the model and were compared to our experimental results. N_2 gas adsorption behavior in the three kerogen model systems was in very good agreement with experimental results in similar conditions, 100 kPa and 77 K. Adsorption of CO_2 molecules on a clustered model also shows similar adsorption isotherm behavior overall. Based on the simulation results we uncovered, the kerogen model seems to have a stronger interaction with CO_2 molecules than N_2 molecules such that CO_2 molecules are not only adsorbed on the surface but also penetrate to the sub-surface level of the model.

Conflicts of interest

There are no conflicts to declare.

Acknowledgements

The financial supports of the Future Material Discovery Program (2016M3D1A1027666) and the Basic Science Research Program (2017R1A2B3009135) through the National Research Foundation of Korea are appreciated. Authors wish to thank two anonymous reviewers and respected editor for comments and feedbacks that helped to improve this manuscript.

References

1 B. Jia, J. Tsau and R. Barati, A Review of the Current Progress of CO_2 Injection EOR and Carbon Storage in Shale Oil Reservoirs, *Fuel*, 2019, **236**, 404–427.

2 Y. Shen, H. Ge, C. Li, Z. Yang, X. Yang, K. Ren and S. Su, Water Imbibition of Shale and Its Potential Influence on Shale Gas Recovery—A Comparative Study of Marine and Continental Shale Formations, *J. Nat. Gas Sci. Eng.*, 2016, **35**, 1121–1128.

3 E. Fathi and I. Y. Akkutlu, Multi-Component Gas Transport and Adsorption Effects during CO_2 Injection and Enhanced Shale Gas Recovery, *Int. J. Coal Geol.*, 2014, **123**, 52.

4 A. Vengosh, R. B. Jackson, N. Warner, T. H. Darrah and A. Kondash, A Critical Review of the Risks to Water Resources from Unconventional Shale Gas Development and Hydraulic Fracturing in the United States, *Environ. Sci. Technol. Lett.*, 2014, **48**, 8334–8348.

5 A. Muggeridge, A. Cockin, K. Webb, H. Frampton, I. Collins, T. Moulds and P. Salino, Recovery Rates, Enhanced Oil Recovery and Technological Limits, *Philos. Trans. R. Soc., A*, 2013, **372**, 20120320.

6 C. Guo, M. Wei and H. Liu, Study of Gas Production from Shale Reservoirs with Multi-Stage Hydraulic Fracturing Horizontal Well Considering Multiple Transport Mechanisms, *PLoS One*, 2018, **13**, e0188480.

7 B. Durand *Sedimentary Organic Matter and Kerogen. Definition and Quantitative Importance of Kerogen. Kerogen, Insoluble Organic Matter from Sedimentary Rock*, Editions Technips, 1980, pp. 13–34.

8 H. Wang, Z. Qu, Y. Yin, J. Bai and B. Yu, Review of Molecular Simulation Method for Gas Adsorption/desorption and Diffusion in Shale Matrix, *J. Therm. Sci.*, 2019, **28**, 1–16.

9 M. Vandenbroucke and C. Largeau, Kerogen Origin, Evolution and Structure, *Org. Geochem.*, 2007, **38**, 719–833.

10 A. Abarghani, M. Ostadhassan, T. Gentzis, H. Carvajal-Ortiz and B. Bubach, Organofacies Study of The Bakken Source Rock in North Dakota, USA, Based on Organic Petrology and Geochemistry, *Int. J. Coal Geol.*, 2018, **188**, 79–93.

11 C. Bousige, C. M. Ghimbeu, C. Vix-guterl, A. E. Pomerantz, A. Suleimenova, G. Vaughan, G. Garbarino, M. Feygenson, C. Wildgruber, F. Ulm, R. J. Pellenq and B. Coasne, Realistic Molecular Model of Kerogen's Nanostructure, *Nat. Mater.*, 2016, **15**, 576.

12 A. L. Burlingame, P. A. Haug, H. K. Schnoes and B. R. Simoneit, Fatty Acids Derived from the Green River Formation Oil Shale by Extractions and Oxidations—A Review, *Advances in Organic Geochemistry, Proceedings of the 4th International Meeting on Organic Geochemistry*, 1968, pp. 85–129.

13 M. Siskin, C. G. Scouten, K. D. Rose, D. Aczel, S. G. Colgrove and R. E. Pabst, Detailed Structural Characterization of the Organic Material in Rundle Ramsay Crossing and Green River Oil Shales, in *Composition, Geochemistry and Conversion of Oil Shales*, ed. C. Snape, NATO ASI Series (Series C: Mathematical and Physical Sciences), 1995, p. 455.

14 P. Ungerer, J. Collell and M. Yiannourakou, Molecular Modeling of the Volumetric and Thermodynamic Properties of Kerogen: Influence of Organic Type and Maturity, *Energy Fuels*, 2015, **29**, 91–105.

15 J. J. P. Stewart, Optimization of Parameters for Semiempirical Methods VI: More Modifications to the NDDO Approximations and Re-optimization of Parameters, *J. Mol. Model.*, 2013, **19**, 1–32.

16 H. Lee, F. A. Shakib, M. Shokouhimehr, B. Bubach, L. Kong and M. Ostadhassan, Optimal Separation of CO_2/CH_4/Brine with Amorphous Kerogen: A Thermodynamics and Kinetics Study, *J. Phys. Chem. C*, 2019, **123**(34), 20877–20883.

17 J. Collell, P. Ungerer, G. Galliero, M. Yiannourakou, F. Montel and M. Pujol, Molecular Simulation of Bulk Organic Matter in Type II Shales in the Middle of the Oil Formation Window, *Energy Fuels*, 2014, **28**, 7457–7466.

18 S. Tesson and A. Firoozabadi, Methane Adsorption and Self-Diffusion in Shale Kerogen and Slit Nanopores by Molecular Simulations, *J. Phys. Chem. C*, 2018, **122**, 23528–23542.

19 R. Kelemen, C. D. Gorecki, G. Liu, E. N. Steadman, J. R. Braunberger, J. A. Harju, J. Ge and J. A. Sorensen, CO_2-Based Enhanced Oil Recovery from Unconventional Reservoirs: A Case Study of the Bakken Formation, *SPE*

Unconventional Resources Conference, Society of Petroleum Engineers, 2014, vol. 21(3), pp. 1548–1561.

20 S. R. Keleman, M. Afeworki, M. L. Gorbaty, M. Sansone, P. J. Kwiatek, C. C. Walters, H. Freund, M. Siskin, A. E. Bence, D. J. Curry, M. Solum, R. J. Pugmire, M. Vandenbroucke, M. Leblond and F. Behar, Direct Characterization of Kerogen by X-ray and Solid-State ^{13}C Nuclear Magnetic Resonance Methods, *Energy Fuels*, 2007, **21**, 1548–1561.

21 J. Tong, X. Han, S. Wang and X. Jiang, Evaluation of Structural Characteristics of Huadian Oil Shale Kerogen Using Direct Techniques (Solid-State^{13}C NMR, XPS, FT-IR, and XRD), *Energy Fuels*, 2011, **25**, 4006–4013.

22 F. Behar, V. Beaumont and H. L. D. B. Penteado, Rock-Eval 6 Technology: Performances and Developments, *Oil Gas Sci. Technol.*, 2001, **56**, 111–134.

23 M. D. Hanwell, D. E. Curtis, D. C. Lonie, T. Vandermeersch, E. Zurek and G. R. Hutchison, Avogadro: An Advanced Semantic Chemical Editor, Visualization, and Analysis Platform, *J. Cheminf.*, 2012, **4**, 17.

24 J. Wang, W. Wang, P. A. Kollman and D. A. Case, Automatic Atom Type and Bond Type Perception in Molecular Mechanical Calculations, *J. Mol. Graph. Model.*, 2006, **25**, 247–260.

25 J. Wang, R. M. Wolf, J. W. Caldwell, P. A. Kollman and D. A. Case, Development and Testing of a General Amber Force Field, *J. Comput. Chem.*, 2004, **25**, 1157–1174.

26 J. Gasteiger and M. Marsili, A New Model for Calculating Atomic Charges in Molecules, *Tetrahedron Lett.*, 1978, **19**, 3181–3184.

27 S. Plimpton, Fast Parallel Algorithms for Short-Range Molecular Dynamics, *J. Comput. Phys.*, 1995, **117**, 1–19.

28 L. Martinez, R. Andrade, E. G. Birgin and J. M. Martinez, Packmol: A Package for Building Initial Configurations for Molecular Dynamics Simulations, *J. Comput. Chem.*, 2009, **30**, 2157–2164.

29 T. Hočevar and J. Demšar, Computation of Graphlet Orbits for Nodes and Edges in Sparse Graphs, *J. Stat. Software*, 2016, **71**, 1–24.

30 J. Tirado-Rives and W. L. Jorgensen, Performance of B3LYP Density Functional Methods for a Large Set of Organic Molecules, *J. Chem. Theory Comput.*, 2008, **4**, 297–306.

31 F. L. Hirshfeld, Bonded-Atom Fragments for Describing Molecular Charge Densities, *Theor. Chim. Acta*, 1977, **44**, 129–138.

32 W. Humphrey, A. Dalke and K. Schulten, VMD: Visual Molecular Dynamics, *J. Mol. Graph.*, 1996, **14**, 33–38.

33 W. M. Brown, A. Kohlmeyer, S. J. Plimpton and A. N. Tharrington, Implementing Molecular Dynamics on Hybrid High Performance Computers - Particle-Particle Particle-Mesh, *Comput. Phys. Commun.*, 2012, **183**, 449–459.

34 S. J. Plimpton, R. Pollock and M. Stevens, Particle-Mesh Ewald and rRESPA for Parallel Molecular Dynamics Simulations, in *Proceedings of the Eighth SIAM Conference on Parallel Processing for Scientific Computing*, 1997.

35 J. J. Potoff and J. I. Siepmann, Vapor–Liquid Equilibria of Mixtures Containing Alkanes, Carbon Dioxide, and Nitrogen, *AIChE J.*, 2001, **47**, 1676–1682.

36 K. Liu, M. Ostadhassan, J. Zhou, T. Gentzis and R. Rezaee, Nanoscale Pore Structure Characterization of the Bakken Shale in the USA, *Fuel*, 2017, **209**, 567–578.

37 R. G. Kadesch and S. W. Weller, The steric Inhibition of Resonance in Aromatic Carbonyl Compounds, *J. Am. Chem. Soc.*, 1941, **63**(5), 1310–1314.

38 P. Psarras, R. Holmes, V. Vishal and J. Wilcox, Methane and CO_2 Adsorption Capacities of Kerogen in the Eagle Ford Shale from Molecular Simulation, *Accounts Chem. Res.*, 2017, **50**, 1818–1828.

39 Y. Liu and J. Wilcox, Effects of Surface Heterogeneity on the Adsorption of CO_2 in Microporous Carbons, *Environ. Sci. Technol.*, 2012, **46**, 1940–1947.

Paper 4: Optimal Separation of CO2/CH4/Brine with Amorphous Kerogen: A Thermodynamics and Kinetics Study

THE JOURNAL OF PHYSICAL CHEMISTRY C

Article

Cite This: J. Phys. Chem. C 2019, 123, 20877−20883

pubs.acs.org/JPCC

Optimal Separation of CO_2/CH_4/Brine with Amorphous Kerogen: A Thermodynamics and Kinetics Study

Hyeonseok Lee,[†] Farnaz A. Shakib,[*,‡] Mohammadreza Shokouhimehr,[*,†,§] Bailey Bubach,[†] Lingyun Kong,[†] and Mehdi Ostadhassan[*,†,∥]

[†]Department of Petroleum Engineering, University of North Dakota, Grand Forks, North Dakota 58202, United States

[‡]Department of Chemistry and Environmental Science, New Jersey Institute of Technology, Newark, New Jersey 07102, United States

[§]Department of Materials Science and Engineering, Seoul National University, Seoul 08826, Republic of Korea

[∥]Key Laboratory of Continental Shale Hydrocarbon Accumalation and Efficient Development, Northeast Petroleum University, Daqing 163318, China

Supporting Information

ABSTRACT: Carbon dioxide (CO_2)-enhanced oil recovery and sequestration are both processes that are associated with the separation and storage of gas in organic-rich shale formations. The current study investigates the applicability of kerogen, an amorphous and insoluble organic matter abundant in unconventional shale formations, for the separation of the mixture of gases (CO_2 and CH_4) in dry and wet (brine) conditions for an effective storage and injection operation. Here, through molecular dynamics, thermodynamics, and kinetics, we investigate the CO_2 transportation and adsorption behavior on three-dimensional kerogen molecular models from the Bakken, which contains nonperiodically arrayed functional groups. The diffusion/separation of CO_2 and CH_4 is probed subject to a varying range of concentrations as well as pressure from atmospheric to high (30 bar) and realistic temperatures (333−393 K) to represent an unconventional reservoir system. It is found that kerogen models from the Bakken would demonstrate an unprecedented CO_2 sorption selectivity over methane in the presence of brine (formation or interstitial water, a mixture of water and salt). Moreover, the concentration of brine shows a positive effect for CO_2/CH_4 selectivity that supports our goals of sequestration and enhanced production. Based on the quantitative results, the developed kerogen model is suggested as an appropriate framework for CO_2 sequestration and injection to further facilitate hydrocarbon-improved recovery in organic-rich shale reservoirs and promote sequestration in a major shale formation.

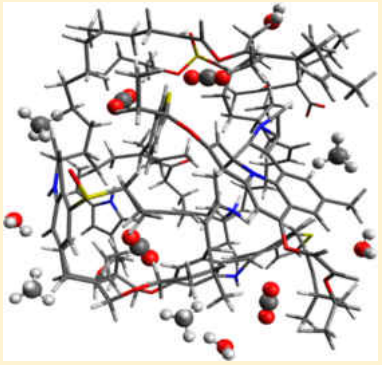

INTRODUCTION

Over the last two decades, there has been growing attention toward separation and sequestration of greenhouse gases using organic-rich shales, which can also address a viable injection/production scheme for CO_2 enhanced oil recovery (EOR) operation.[1,2] The injection of CO_2 into unconventional organic-rich shales is not only an effective method to boost hydrocarbon productivity and more efficient recovery but also can serve as a large-scale CO_2 capture technique.[3−6] The organic matter, which is abundant in shale formations, also known as kerogen, has a complex molecular structure and mainly consists of carbon, hydrogen, oxygen, nitrogen, and sulfur.[7] Studies have found that kerogen in shale formations can chemically interact with CO_2 and hydrocarbons to enhance the selectivity of CO_2 over hydrocarbons in the presence of other fluids.[8] However, it is a challenge to produce hydrocarbons and store CO_2 simultaneously due to the interference of hydrocarbons and brine in CO_2 sorption.[9] Moreover, the CO_2 selectivity, the ratio of the adsorbed CO_2 onto the membrane (here kerogen) over hydrocarbons,[10] is drastically affected by temperature and pressure.[9] Hence, it is necessary to have a clear picture of the CO_2 diffusion kinetics and thermodynamics over a range of brine concentrations at different temperatures and pressures for more efficient CO_2 separation, injection, and sequestration. The investigation of CO_2 selectivity in the presence of mixtures (CO_2, CH_4, and the brine) is the key to improve CO_2 separation in unconventional organic-rich reservoirs.

Kerogen, which contains a large surface area within its nano- to micrometer pore spaces,[9,11] is inherently CO_2-phillic, meaning this macromolecule compound would act as a CO_2-selective membrane.[7] The selectivity of this amorphous organic material for CO_2 sorption over CH_4 has been confirmed through experimentally measured volumetric uptake as well as computational simulations.[12−16] Although the large surface area of the adsorbent encourages high uptake of CO_2 gas molecules, it is not necessarily advantageous for optimal separations in a specific system in the presence of other

Received: May 9, 2019
Revised: July 17, 2019
Published: August 2, 2019

DOI: 10.1021/acs.jpcc.9b04432
J. Phys. Chem. C 2019, 123, 20877−20883

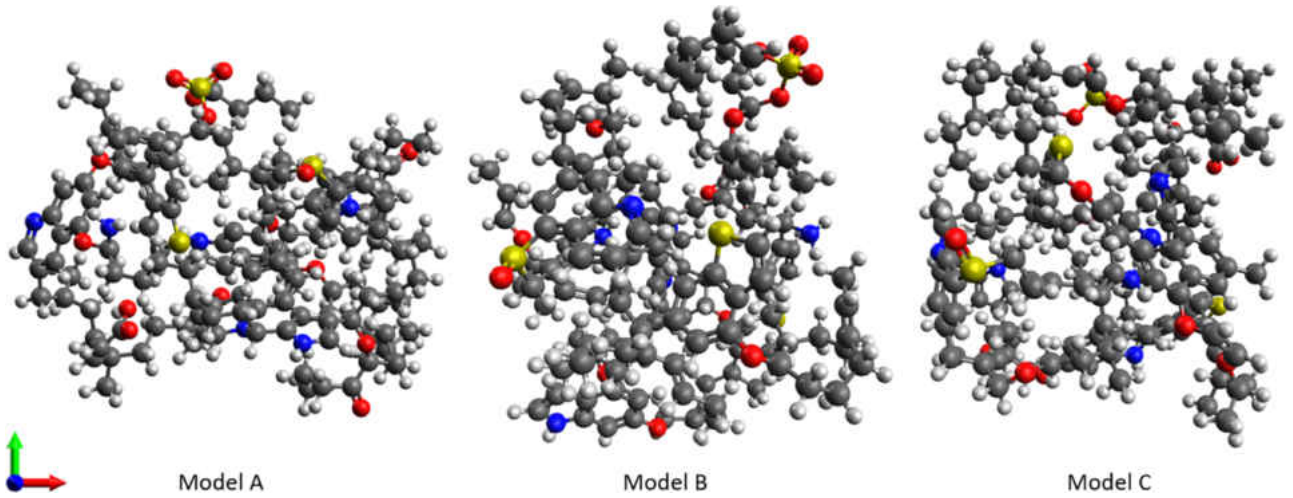

Figure 1. Immature (preoil window) Bakken kerogen models. Different geometric configurations and chemical compositions with the color code, carbon in black; hydrogen in white; oxygen in red; sulfur in yellow; and nitrogen in blue.[16]

important influencing components such as temperature, pressure, and existing fluids.

In a recent study, we have developed three different computational models to represent the Bakken kerogen.[17] The Bakken formation is one of the largest unconventional shale oil plays in North America and is currently being studied for potential CO_2-enhanced oil recovery and sequestration. It has also attracted extensive geochemistry and organic petrography studies entailing its geological background and physical properties.[18,19] Representing Bakken kerogen, our models contain surface pores and functional groups consisting of carbon, hydrogen, oxygen, nitrogen, and sulfur. Using these models, we studied the diffusion of CO_2 and N_2 molecules through the kerogen membrane obtaining comparable results to the experimental adsorption outcomes.[17,20] Having established the reliability of our Bakken kerogen model, here, we employ these models to demonstrate the applicability of kerogen for the separation of the mixture of gases CO_2 and CH_4 in dry and wet (brine) conditions via molecular simulations. Here, we put a special emphasis on the effect of brine as the formation water and investigate the interaction of brine with the gases CO_2 and CH_4 and its overall effect on the gas sorption by kerogen.[21] We analyze the diffusion and separation of CO_2/CH_4/brine systems, which would affect the performance of the EOR process in particular tight shale formations where the improvement of recovery through CO_2 injection is still ambiguous and under research.[22,23]

MATERIALS AND METHODS

Statistical mechanics, equilibrium molecular dynamics, in particular, was employed to study the selectivity of CO_2 over CH_4 in realistic molecular models of the Bakken kerogen to report diffusion/separation that occurs under three variants of environments: pressure, temperature, and various existing fluids (CH_4, H_2O, and NaCl).

Bakken Kerogen Model. The molecular models of the Bakken kerogen were obtained from computational simulations in accordance with the experimental analysis obtained from geochemistry screening by the Rock−Eval pyrolysis,[13] C-13 nuclear magnetic resonance (NMR) spectroscopy, X-ray photon spectroscopy (XPS), and gas adsorption isotherms.[20,24] The organic matter structures were modeled based on type II kerogen (representative of the Bakken) in the preoil window (immature) and were mainly composed of carbon and hydrogen with nitrogen, oxygen, and sulfur atoms as attachments (Figure 1). A brief introduction to the models is presented here, whereas readers are referred to Lee et al.[17] and the Supporting Information (SI) for further details.

Kerogen is a heavy and amorphous organic material, which is quantitatively difficult to describe in terms of its chemical composition and functional groups. This originates from the fact that the chemical structure of the organic matter varies significantly based on its biogenic origin whether it is animal based or plant based, from marine environments or terrestrial. Bakken, in particular, is a type II kerogen, which is made up of marine organisms. The difference in each kerogen type is represented by their O/C and H/C ratios in elemental analysis.[7] Although a general chemical composition for kerogen can be used, the models in this study are based on the experimental data collected exclusively from the Bakken to ensure the highest level of similarity to physical samples.[17] The structures of these three Bakken kerogen models (models A, B, and C) are a complicated mixture of chain and mesh. Although these models were constructed through the same procedure (i.e., analyzing experimental data, molecular mechanics simulation, and quantum mechanics calculations), each model owns a different chemical composition and topology, $C_{140}H_{176}N_6O_{15}S_4$, $C_{151}H_{179}N_6O_{15}S_4$, and $C_{158}H_{188}N_6O_{16}S_4$, respectively.[17] The structures contain disordered pores with the radius ∼3−7 Å, the calculated densities of models A, B, and C are around 1.1, 1.2, and 1.3 g cm^{-3}, respectively. These models have been already shown to reproduce the experimental adsorption isotherms for CO_2 and N_2 uptake at low pressure and correctly assign Bakken kerogen as a selective CO_2 absorbent in the presence of N_2.[17,20]

In the current study, we collect and tether all three molecular models into one gas diffusion/separation system to avoid a biased outcome from our simulation results. The Packmol package was utilized to place one of each kerogen models (models A, B, and C) in a feed compartment with the size of 16 × 57 × 40 Å, as shown in Figure 2. These two systems were then allowed to come to relaxation by running a 1 ps NVT molecular dynamics simulations. Since the three kerogen models were simply adhered to one another and

DOI: 10.1021/acs.jpcc.9b04432
J. Phys. Chem. C 2019, 123, 20877−20883

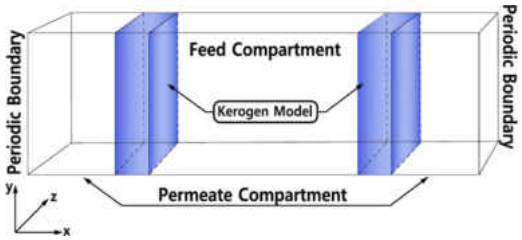

Figure 2. Schematic illustration of alternating Feed/Permeate compartment; the molecular kerogen model is collected and tethered into one gas diffusion/separation system.

clustered, packing them in different modes was not considered. In this system, gaseous fluids in the feed compartment would diffuse to two different surfaces of kerogen, to the left and right models in Figure 2. The details of all parameters, which attribute to the chemical composition and the carbon-based structure of these molecules, are described in Table 1. The kerogen model in this system is composed of inner and outer pores, which is a disordered molecular structure and includes functional groups.

Table 1. Average of Carbon Structural Parameters for the Bakken Kerogen Models (Combination of Models A, B, and C)[17a]

structure	kerogen model (combined)
aromatic	35
carboxyl/amide/carbonyl	2.6
protonated aromatic	17
phenoxy/phenolic	2.1
alkyl-substituted aromatic	6.6
bridged aromatic	9.2
aliphatic	62
methylene/methine	32
methyl/methoxy	12
alcohol/ether	4.1

[a]Note: the data presented here are ratio per 100 number of carbon.

Simulation Setup. The simulation of molecular transport utilizes a system setup that is developed by others on an osmosis/reverse osmosis system and is briefly discussed here.[25] The simulation system for studying gas separation/diffusion based on our kerogen model can be found in Figure 2. Two identical kerogen models are used along with periodic boundary conditions to create alternating fluid compartments in the *X*-direction, whereas the system is infinite in the transverse dimensions (*y*, *z*) (Figure 2). Kerogen atoms are tethered to their known equilibrium positions using a simple harmonic tether. The region between the two kerogen models (feed compartment) was filled with the fluid to be separated at the desired conditions. Initially, empty left and right permeate compartments were set up to provide the driving force, whereas periodic boundary conditions would allow a continuous compartment. Long-range site−site interactions are modeled using Lennard−Jones (LJ) and Coulombic potentials as following

$$E_{\text{total}} = \sum_{i<j} 4\varepsilon\left[(\frac{\sigma_{ij}}{r_{ij}})^{12} - \left(\frac{\sigma_{ij}}{r_{ij}}\right)^{6}\right] + \sum_{i<j}\frac{Cq_iq_j}{\varepsilon R_{ij}}, \quad r_{ij} < r_c \tag{1}$$

where r_{ij} is the distance between sites i and j, r_C is the cutoff radius beyond which the short-range interactions are neglected, σ_{ij} and ε are the L−J parameters, q_i and q_j represent the charges on sites i and j, and C is a unit conversion constant. These potentials are summed over all sites to obtain the total intermolecular interactions.

To carry out molecular dynamics simulation on the mixture fluid (CO_2, CH_4, H_2O, Na^{1+}, and Cl^{1-}), the harmonic potential was employed between the model and gas molecules, along with the site to site nonbonding interaction potential. The transportation of fluid particles within the kerogen models was investigated using molecular dynamics simulations at a practical temperature and pressures relevant to the Bakken Formation (T = 333−393 K and P = 1−30 bar).[26] Water was modeled under a simple point charge (SPC),[27] whereas CO_2 is modeled using the flexible force field developed by Cygan et al.,[28] CH_4 is represented by the TraPPE force field, and Na^{1+} and Cl^{1-} ions are modeled using the parameters proposed by Smith and Dang.[29,30] The parameters and charges used in this study are summarized in Table 2. The reliability of the SPC water model is confirmed by utilizing two other models, TIP3P and SPC/Fw, for similar calculations, which resulted in consistant results, Figures S1 and S2 in the SI.

Table 2. Parameters Related to the Adsorbates (CH_4, CO_2, and Brine)

molecules	atoms/ions	charge	σ (Å)	ε (kcal/mol)
CH_4	C	0.00	3.73	0.2941
H_2O	O	−0.82	3.17	0.1554
	H	0.41	0.0	0.0
CO_2	C	0.65	2.80	0.0559
	O	−0.325	3.028	0.1597
salt	Na^{1+}	1.00	2.35	0.13
	Cl^{1-}	−1.00	4.40	0.10

Initial configurations were created using the Packmol to construct nonoverlapping random fluid initial configurations.[31] All equilibrium simulations (EMD) of the systems considered here, were carried out by molecular dynamics of gas adsorption processes using the "osmosis and reverse osmosis" technique with the LAMMPS simulation package.[25,32] The particle−particle/particle−mesh (PPPM) technique was used in the treatment of long-range Coulombic interactions beyond the cutoff radius of 1.4 nm.[33]

All simulation cells are parallel to the kerogen/mixture fluid interface, and periodic boundary conditions are employed in all of the three dimensions. The system size is sufficiently large to ensure that finite-size effects are negligible in our 1 ns equilibration simulations that is performed in the NPT ensemble, where the volume variations are achieved by changing the box length only in the *x*-direction. Then, NVT ensemble equilibrium molecular dynamics simulations were performed, in which the temperature of the system is kept at a fixed value by a Gaussian thermostat. All simulations were carried out at three different temperatures, 333, 363, and 393 K, which are typical temperatures for the Bakken formation.[26] A time step of 1 fs was used for runs up to 10 ns in length (10 million steps).

To further clarify the competitive separation, the selectivity of CO_2 over CH_4 in the mixture of CO_2 and CH_4 is determined using the following equation[16,35]

DOI: 10.1021/acs.jpcc.9b04432
J. Phys. Chem. C 2019, 123, 20877−20883

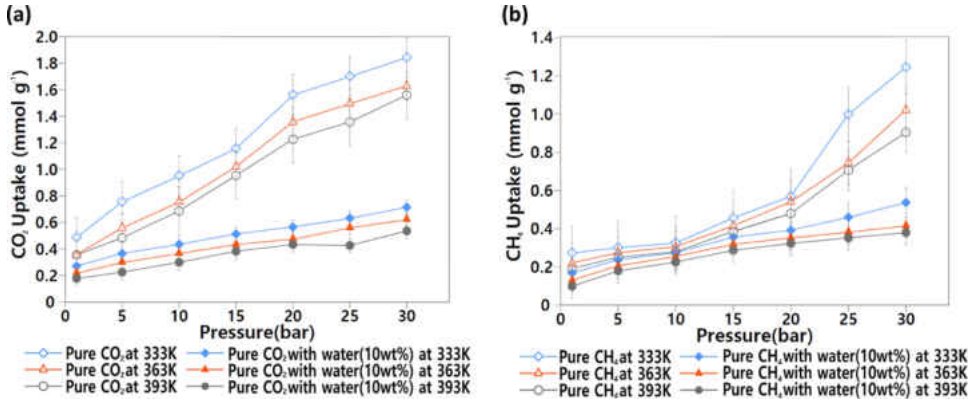

Figure 3. Gas uptake in single and binary (with 10 wt % of H_2O) systems for CO_2 (a) and CH_4 (b) on the kerogen model at variable temperatures (333, 363, and 393 K) and pressures (1−30 bar) with corresponding error bars at certain pressures.

$$S_{CO_2/CH_4} = \frac{x_{CO_2}/x_{CH_4}}{y_{CO_2}/y_{CH_4}} \quad (2)$$

where x and y refer to the mole fractions of the component of the adsorbed surface phase and the bulk phase, respectively. Higher adsorption selectivity (values over 1) indicates a stronger adsorption capacity of CO_2 over CH_4. We also used the isosteric heat of adsorption (Q_{st}) to estimate the strength between molecules and the molecular models. The adsorption is accompanied by temperature variations since the adsorbed molecules are more stabilized on the adsorbent surface than in the bulk phase. Q_{st} is defined by the Clausius−Clapeyron equation[34]

$$Q_{st} = RT^2\left[\frac{\partial \ln P}{\partial T}\right]_N \quad (3)$$

where P is the equilibrium pressure at temperature T and N represents the number of adsorbed species. The equation, when integrated, allows one to calculate Q_{st} obtained at two or more temperatures. Prediction is based on the assumption that the isosteric heat of adsorption is independent of temperature.

RESULTS AND DISCUSSION

Open data points in Figure 3a,b illustrate CO_2 and CH_4 molecules uptake in/on the dry Bakken model surface region collected from atmospheric pressures to an elevated pressure (30 bar) at 333, 363, and 393 K temperatures. Overall, the CO_2 uptake capacity is higher than CH_4, in the range of 0.35−1.85 vs 0.2−1.26 mmol/g, indicating that CO_2 is preferably adsorbed in/on the Bakken kerogen model surface region compared to CH_4. It is worth mentioning that due to the structural properties of the kerogen molecular model, the final gas uptake is the result of the presence of both the functional groups and the porous structure.

Moreover, the presence of water (10 wt %) in the single CO_2 and CH_4 gas is shown to have a negative effect on gas uptake (filled data points in Figure 3a,b). The uptake of CO_2 gas molecules at higher pressure (over 20 bar) declines as much as 60%, whereas the ones at lower pressures (less than 15 bar) show a decrease of about 50%. On the other hand, the uptake of CH_4 gas molecules at lower pressures (less than 20 bar) demonstrates a smaller reduction compared to the higher pressures (above 20 bar), around 15 vs 55% decrease. The observed trends are consistent with the previous studies where the uptake capacity of gases on moist type II kerogen exhibited a decline with the increasing moisture content at constant temperatures.[35,36]

Figure 4 presents the isosteric heat of adsorption (Q_{st}) of CO_2 and CH_4 on the kerogen model as a function of the amount of molecules adsorbed, obtained from the CH_4 and CO_2 single systems (Figure 3a,b). It is seen that Q_{st} decreases at the beginning of the adsorption process and then stays relatively constant. This infers that the adsorbent (the kerogen model) becomes a homogeneous binding site on its surface over 0.9 mmol/g of CO_2 and 0.3 mmol/g of CH_4 loadings (Figure 4). The reduction in the isosteric heat of total adsorption at low coverage indicates that the electrostatic and van der Waals interactions between gas molecules and the kerogen model are dominant in the system.[37] Notably, Q_{st} of CO_2 is found to be larger than CH_4, which represents the strong interaction between the positively charged carbon atom and negatively charged oxygen atoms of CO_2 and the functional groups of the kerogen model. These results demonstrate that the kerogen model is a good absorbent for CO_2 separation from the CH_4, which is also confirmed by its selectivity of CO_2 over CH_4 (Figure 6a).

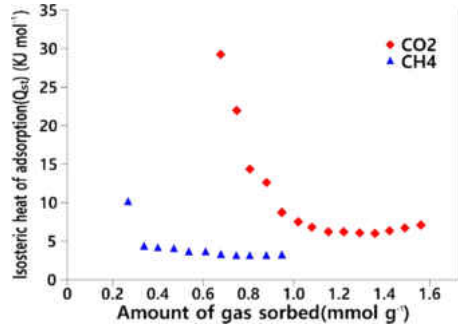

Figure 4. CO_2 and CH_4 isosteric heat of adsorption (Q_{st}) in the low-pressure region.

Figure 5 represents the mean square displacement (MSD) of CO_2 and CH_4 at 333 K temperature. It is shown that CO_2 diffuses much faster than CH_4 within the kerogen macromolecule. We have confirmed that this is the outcome of any scenario at different pressure/temperature conditions where CO_2 always shows a higher self-diffusion in single-gas systems. Figure 5 also shows that at a constant temperature, 333 K, the self-diffusion of CO_2 decreases with the increase of pressure. It can be said that higher pressures would have a negative effect

DOI: 10.1021/acs.jpcc.9b04432
J. Phys. Chem. C 2019, 123, 20877−20883

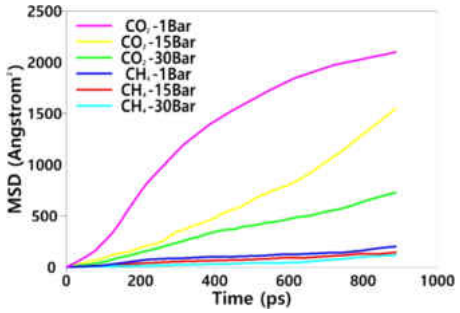

Figure 5. Mean square displacement (MDS) of CO_2 and CH_4 over pressure difference.

on the diffusion of both CO_2 and CH_4 molecules but with a more pronounced effect on the former.

To better understand the governing thermodynamics and kinetics parameters on CO_2 capture, the competitive adsorption kinetics of the CO_2/CH_4 gas mixtures was investigated in the presence of brine (formation water), Figure 6. The CO_2/CH_4 selectivity of the model was investigated using CO_2/CH_4:50/50 gas mixtures at 333, 363, and 393 K temperatures and a range of pressure from 1 to 30 bar. CO_2 molecules are preferentially adsorbed on the surface of the kerogen with higher potential than CH_4 when both exist in the dry system, as shown in Figure 6a. In the system, where the Bakken kerogen and mixed gases are present, CO_2 can displace CH_4, which would facilitate the production of CH_4 from unconventional gas reservoirs. The result indicates that a relatively good production of CH_4 and simultaneously high CO_2 capture capacity could be expected. Remarkably, CO_2/CH_4 selectivity decreases with increasing pressure at any temperature. Considering the CO_2/CH_4:50/50 mixture, CO_2/CH_4 selectivity slightly declines in the presence of pure water at 10 wt % (Figure 6a–d). This is also in agreement with the previous findings that CO_2/CH_4 selectivity decreases when water is added to the mixture.[35]

Figure 6b–d displays CO_2/CH_4 selectivity of the Bakken kerogen in the presence of 5, 7, and 10% brine concentrations at different system temperatures. The motivation of this study was to investigate the possibility of a successful CO_2 EOR and sequestration operation from the molecular point of view in the Bakken at different concentrations of brine, since it varies regionally in the Williston Basin where this rock unit is extended in the subsurface. Considering this important factor, the concentration of brine was broadly selected to particularly explain the effects of brine on such operation, i.e., a range of 3–10% of brine concentration in the mixture with 10 wt % of the whole mixture. The very notable result is that when the gas mixture contains a higher concentration of brine, kerogen demonstrates a much higher CO_2/CH_4 selectivity over the entire pressure range (1–30 bar). To be more specific, the selectivity of the mixture system comprising of CO_2/CH_4/brine is found to be higher than the mixture system of CO_2/CH_4/pure water, at the same pressure and temperature; furthermore, the selectivity increases in the presence of higher concentrations of brine. It has been previously discussed that salinity will result in an increase of interfacial tension (IFT) not only in the CO_2/CH_4/brine but also in both the CH_4/Brine and CO_2/brine systems.[38] It has been demonstrated that IFT of CO_2/Brine is generally lower than CH_4/Brine at the same brine concentration confirming the weaker intermolecular interaction between CO_2 and brine compared to CH_4. Therefore, lower IFT between CO_2 and brine can be generally inferred as the higher selectivity of Bakken kerogen for CO_2 over CH_4 in the presence of brine.

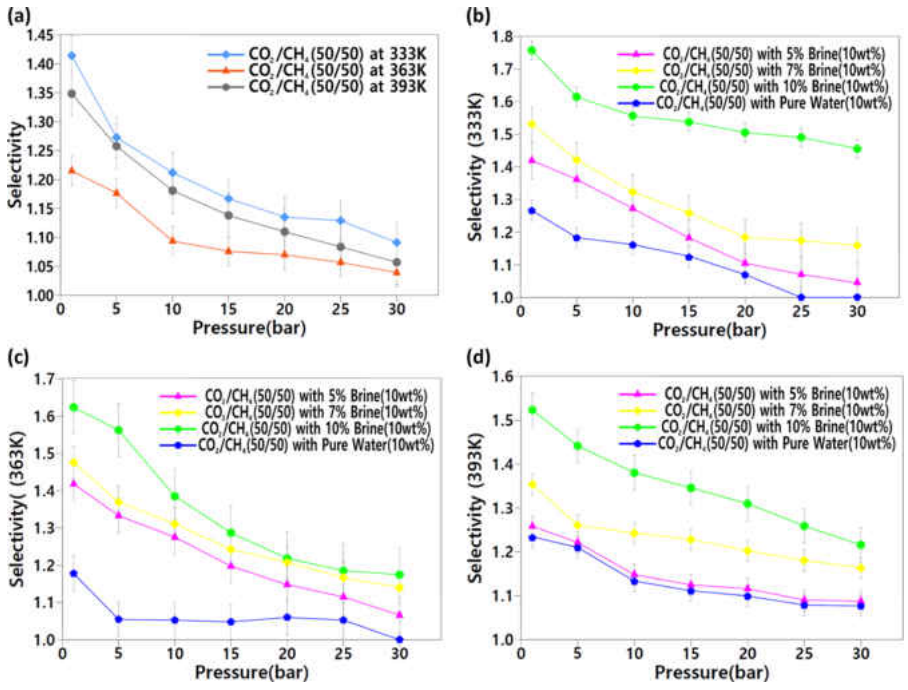

Figure 6. (a) Estimated CO_2/CH_4 selectivity for the binary mixture (CO_2/CH_4:50/50 mol %) on the kerogen model. Estimated CO_2/CH_4 selectivity for the mixture of CO_2/CH_4/brine on the kerogen model at (b) 333 K, (c) 363 K, and (d) 393 K. In panels (b)–(d), the comparative concentrations of $CO_2/CH_4/H_2O$/NaCl in solutions of 5, 7, and 10% brine are 42.3/42.3/15.2/0.2, 42.3/42.3/15.1/0.4, and 42.5/42.5/14.5/0.5 mol %, respectively. Error bars are shown at certain pressure steps.

DOI: 10.1021/acs.jpcc.9b04432
J. Phys. Chem. C 2019, 123, 20877–20883

On the other hand, the selectivity declines as a function of pressure when the system reaches equilibrium, regardless of the presence of brine. The highest CO_2/CH_4 selectivity (maximum of 1.76) is found in the highest brine concentration (10%) at a comparatively lower temperature (333 K) and pressure (1 bar), whereas the mixture including pure water had the lowest CO_2/CH_4 selectivity at every simulation condition. Also, the pure water mixture did not support increasing CO_2/CH_4 selectivity at higher pressures and nearly converged to 1. Moreover, the simulation results demonstrate that when the concentration of the brine reaches over 7%, the presence of brine has a more positive impact on the selectivity, compared to the scenario when water is absent. Hence, it can be concluded that brine plays an important role in CO_2/CH_4 selectivity, which can cause sequestration and EOR outcome to vary in the field based on regional interstitial water chemistry within the organic-rich shale formation.

To better evaluate higher CO_2/CH_4 selectivity trends, diffusion/separation of single and mixture of gases (CO_2, CH_4, and brine) was measured at both low and high pressures, in a long simulation run (over 10 ns). This will enable us to predict diffusion equilibria for the CO_2/CH_4:50/50 mixtures with different concentrations of brine. The molecules were diffused and separated in the system dominantly on a count of the electrostatic and van der Waals interactions between gas molecules and the kerogen model. It was found that when CO_2 containing mixtures diffuse in the system, Figure 7, the

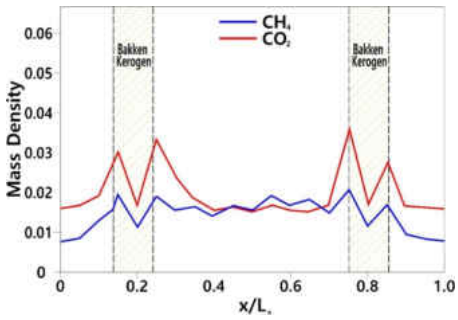

Figure 7. Density mass profile for CO_2 and CH_4 molecules with 10 wt % brine at 333 K in a steady-state simulation and an initial solution concentration of 42.5 CO_2/42.5 CH_4/14.5 H_2O/0.5 NaCl mol %. L_x is the system dimension perpendicular to the kerogen model.

interaction between the kerogen model and each molecule would vary. Considering the competitive diffusion of CO_2 and CH_4 in the system, CO_2 molecules are mainly observed to place on the surface region of the model, whereas CH_4 molecules are detected on both the bulk and the surface of the model due to weaker interactions with the kerogen molecule and functional groups. CO_2 molecules express higher interactions with kerogen pore surfaces than CH_4 and water molecules, thus occupying available space and sites on the kerogen surface. This will result in the exclusion of other gases to get adsorbed to the kerogen surface. Additionally, increasing the temperature of the CO_2 diffusion/separation system did not meaningfully decrease the CO_2/CH_4 selectivity at higher pressures, which makes it beneficial in the CO_2 separation and sequestration applications. Based on these results, the injection of CO_2 in the Bakken can provide us with the desired outcome to satisfy a successful and economical carbon capture and EOR operation simultaneously.

CONCLUSIONS

CO_2 selectivity and the effect of brine for both sequestration and EOR in the Bakken, which is an organic-rich shale, were studied. We have demonstrated that electrostatic and van der Waals interactions between the disordered surface of the kerogen and different gases govern the separation process. The provided insights into the thermodynamics and kinetics of the adsorption selectivity phenomenon in this work could be useful to design a more effective CO_2 separation and capture process in kerogen. Based on the results, the following conclusions can be made:

- Considering the case of a single gas (CO_2 and CH_4) in the system, the temperature has a negative effect on the adsorption of the gas where the gas uptake capacity decreases with increasing temperature at a given pressure. On the other hand, the pressure has a positive effect on the gas uptake capacity at given a given temperature. Similar results were found to govern adsorption of the mixture of gas and pure water (nonsaline) system.
- The interactions between the Bakken kerogen models and CO_2 are stronger than the one with CH_4. The self-diffusion of gases decreases as the pressure increases at a given temperature.
- Higher CO_2/CH_4 selectivity happens when the gas mixture contains a higher concentration of brine at a given temperature and pressure. When the mixture contains pure water, CO_2/CH_4 selectivity will become less than a dry system.
- Based on the previous conclusion, brine and its concentration seem to have a significant impact on the CO_2/CH_4 selectivity at different temperature and pressure and can be the main controlling factor for a successful carbon dioxide capture and EOR operation in an unconventional organic-rich shale.

ASSOCIATED CONTENT

Supporting Information

The Supporting Information is available free of charge on the ACS Publications website at DOI: 10.1021/acs.jpcc.9b04432.

Bakken kerogen models (molecular dynamics simulation and quantum mechanics); water models comparison; radial distribution function analysis; Bakken kerogen models − *xyz* information (PDF)

AUTHOR INFORMATION

Corresponding Authors

*E-mail: shakib@njit.edu (F.A.S.).
*E-mail: mrsh2@snu.ac.kr (M.S.).
*E-mail: mehdi.ostadhassan@und.edu, mehdi.ostadhassan@nepu.edu.cn (M.O.).

ORCID

Hyeonseok Lee: 0000-0002-9808-2272
Farnaz A. Shakib: 0000-0003-1432-2812
Mohammadreza Shokouhimehr: 0000-0003-1416-6805
Lingyun Kong: 0000-0001-9703-8299

Notes

The authors declare no competing financial interest.

DOI: 10.1021/acs.jpcc.9b04432
J. Phys. Chem. C 2019, 123, 20877−20883

REFERENCES

(1) Bachu, S. Sequestration of CO2 in Geological Media: Criteria and Approach for Site Selection in Response to Climate Change. *Energy Convers. Manage.* **2000**, *41*, 953−970.

(2) Jia, B.; Tsau, J.; Barati, R. A Review of The Current Progress of CO2 Injection EOR and Carbon Storage in Shale Oil Reservoirs. *Fuel* **2019**, *236*, 404−427.

(3) Department of Energy. https://www.netl.doe.gov/coal/carbon-storage/publications.

(4) Busch, A.; Alles, S.; Gensterblum, Y.; Prinz, D.; Dewhurst, D. N.; Raven, M. D.; Stanjek, H.; Krooss, B. M. Carbon Dioxide Storage Potential of Shales. *Int. J. Greenhouse Gas Control* **2008**, *2*, 297−308.

(5) Kuuskraa, V. A.; Godec, M. L.; Dipietro, P. CO2 Utilization from "Next Generation" CO2 Enhanced Oil Recovery Technology. *Energy Procedia* **2013**, *37*, 6854−6866.

(6) Jessen, K.; Kovscek, A. R.; Orr, F. M. Increasing CO2 Storage in Oil Recovery. *Energy Convers. Manage.* **2005**, *46*, 293−311.

(7) Durand, B. *Sedimentary Organic Matter and Kerogen. Definition and Quantitative Importance of Kerogen. Kerogen, Insoluble Organic Matter from Sedimentary Rock*; Editions Technips, 1980; pp 13−34.

(8) Cancino, O. P. O.; Perez, D.; Pozo, M.; Bessieres, D. Adsorption of Pure CO2 and A CO2/CH4 mixture on A Black Shale Sample: Manometry and Microcalorimetry Measurements. *J. Pet. Sci. Eng.* **2017**, *159*, 307−313.

(9) Alvarado, V.; Manrique, E. Enhanced Oil Recovery: An Update Review. *Energies* **2010**, *3*, 1529−1575.

(10) Zhang, J.; Liu, K.; Clennell, M. B.; Dewhurst, D. N.; Pervukhina, M. Molecular Simulation of CO2−CH4 Competitive Adsorption and Inducedcoal Swelling. *Fuel* **2015**, *160*, 309−317.

(11) Liu, K.; Ostadhassan, M.; Sun, L.; Zou, J.; Yuan, Y.; Gentzis, T.; Zhang, Y.; Carvajal-Ortiz, H.; Rezaee, R. A Comprehensive Pore Structure Study of the Bakken Shale with SANS, N2 Adsorption and Mercury Intrusion. *Fuel* **2019**, *245*, 274−285.

(12) Heller, R.; Zoback, M. Adsorption of Methane and Carbon Dioxide on Gas Shale and Pure Mineral Samples. *J. Unconv. Oil Gas Resour.* **2014**, *8*, 14−24.

(13) Wang, T.; Tian, S.; Li, G.; Sheng, M. Selective Adsorption of Supercritical Carbon Dioxide and Methane Binary Mixture in Shale Kerogen Nanopores. *J. Nat. Gas Sci. Eng.* **2018**, *50*, 181−188.

(14) Huang, L.; et al. Molecular Simulation of Adsorption Behaviors of Methane, Carbon Dioxide and their Mixtures on Kerogen: Effect of Kerogen Maturity and Moisture Content. *Fuel* **2018**, *211*, 159−172.

(15) Psarras, P.; Holmes, R.; Vishal, V.; Wilcox, J. Methane and CO2 Adsorption Capacities of Kerogen in the Eagle Ford Shale from Molecular Simulation. *Acc. Chem. Res.* **2017**, *50*, 1818−1828.

(16) Wang, T.; Tian, S.; Li, G.; Sheng, M.; Ren, W.; Liu, Q.; Zhang, S. Molecular Simulation of CO2/CH4 Competitive Adsorption on Shale Kerogen for CO2 Sequestration and Enhanced Gas Recovery. *J. Phys. Chem. C* **2018**, *122*, 17009−17018.

(17) Lee, H.; Ostadhassan, M.; liu, K.; Bubach, B. Developing an Amorphous Kerogen Molecular Model Based on Gas Adsorption Isotherms, 2019. [Online early access]. DOI: DOI: 10.26434/chemrxiv.7965152. Published Online: April 09, 2019. https://chemrxiv.org/s/dbfe102258d971e948f6.

(18) Abarghani, A.; Ostadhassan, M.; Gentzis, T.; Carvajal-Ortiz, H.; Bubach, B. Organofacies Study of the Bakken Source Rock in North Dakota, USA, based on organic petrology and geochemistry. *Int. J. Coal Geol.* **2018**, *188*, 79−93.

(19) Smith, M. G.; Bustin, R. M. Sedimentology of the Late Devonian and Early Mississippian Bakken Formation, Williston Basin. Proceedings of Seventh International Williston Basin Symposium, Billings, Montana, Jul 23−25, 1995; L. D., Vern Hunter, R. A., Schalla, Eds.; Montana Geological Society: Montana, 1995; pp 103−114.

(20) Liu, K.; Ostadhassan, M.; Zhou, J.; Gentzis, T.; Rezaee, R. Nanoscale Pore Structure Characterization of the Bakken Shale in The USA. *Fuel* **2017**, *209*, 567−578.

(21) Fakcharoenphol, P.; Kurtoglu, B.; Kazemi, H.; Charoenwongsa, S.; Wu, Y. The Effect of Osmotic Pressure on Improve Oil Recovery from Fractured Shale Formations. *SPE Unconventional Resources Conference*; Society of Petroleum Engineers, 2014.

(22) Edwards, R. W.; Celia, M. A.; Bandilla, K. W.; Doster, F.; Kanno, C. M. A Model to Estimate Carbon Dioxide Injectivity and Storage Capacity for Geological Sequestration in Shale Gas Wells. *Environ. Sci. Technol.* **2015**, *49*, 9222−9229.

(23) Jin, L.; Hawthornea, S.; Sorensena, J.; Pekota, L.; Kurza, B.; Smitha, S.; Heebinka, L.; Herdegenb, V.; Bossharta, N.; Torresa, J.; et al. Advancing CO2enhanced Oil Recovery and Storage in Unconventional Oil Play—Experimental Studies on Bakken Shales. *Appl. Energy* **2017**, *208*, 171−183.

(24) Kelemen, S. R.; Afeworki, M.; Gorbaty, M. L.; Sansone, M.; Kwiatek, P. J.; Walters, C. C.; Freund, H.; Siskin, M.; et al. Direct Characterization of Kerogen by x-ray and Solid-State 13C Nuclear Magnetic Resonance Methods. *Energy Fuels* **2007**, *21*, 1548−1561.

(25) Murad, S.; Lin, J. Using Thin Zeolite Membranes and External Electric Fields To Separate Supercritical Aqueous Electrolyte Solutions. *Ind. Eng. Chem. Res.* **2002**, *41*, 1076−1083.

(26) Gosnold, W. D.; Mcdonald, M. R.; Klenner, R.; Merriam, D. Thermostratigraphy of the Williston Basin. *GRC Trans.* **2012**, *36*, 663−670.

(27) Berendsen, H. J. C.; Postma, J.; Gunsteren, W. F.; Hermans, J. Interaction Models for Water in Relation to Protein Hydration. *Intermolecular Forces*; Springer: Dordrecht, 1981; pp 331−342.

(28) Cygan, R. T.; Romanov, V. N.; Myshakin, E. M. Molecular Simulation of Carbon Dioxide Capture by Montmorillonite Using an Accurate and Flexible Force Field. *J. Phys. Chem. C* **2012**, *116*, 13079−13091.

(29) Martin, M. G.; Siepmann, J. I. Transferable Potentials for Phase Equilibria. 1. United-Atom Description of n-Alkanes. *J. Phys. Chem. B* **1998**, *102*, 2569−2577.

(30) Smith, D. E.; Dang, L. X. Computer Simulations of NaCl Association in Polarizable Water. *J. Chem. Phys.* **1994**, *100*, 3757.

(31) Martinez, L.; Andrade, R.; Birgin, E. G.; Martinez, J. M. Packmol: A Package for Building Initial Configurations for Molecular Dynamics Simulations. *J. Comput. Chem.* **2009**, *30*, 2157−2164.

(32) Plimpton, S. Fast Parallel Algorithms for Short-range Molecular Dynamics. *J. Comput. Phys.* **1995**, *117*, 1−19.

(33) Brown, W. M.; Kohlmeyer, A.; Plimpton, S. J.; Tharrington, A. N. Implementing Molecular Dynamics on Hybrid High Performance Computers - Particle-Particle Particle-Mesh. *Comput. Phys. Commun.* **2012**, *183*, 449−459.

(34) Çengel, Y. A.; Boles, M. A. *Thermodynamics: an Engineering Approach*; McGraw-Hill: Boston, 1998.

(35) Huang, L.; Ning, Z.; Wang, Q.; Zhang, W.; Cheng, Z.; Wu, X.; Qin, H. Effect of Organic Type and Moisture on CO2/CH4 Competitive Adsorption in Kerogen with Implications for CO2 Sequestration and Enhanced CH4 Recovery. *Appl. Energy* **2018**, *210*, 28−43.

(36) Zhao, T.; Li, X.; Ning, Z.; Zhao, H.; Li, M. Molecular Simulation of Methane Adsorption on Type II Kerogen with the Impact of Water Content. *J. Pet. Sci. Eng.* **2018**, *161*, 302−310.

(37) Lodish, H.; Berk, A.; Zipursky, S. L.; Matsudaira, P.; Baltimore, D.; Darnell, J. *Molecular Cell Biology*, 4th ed., New York: W. H. Freeman, 2000; Section 2.2.

(38) Liu, Y.; Li, H. A.; Okuno, R. Measurements and Modeling of Interfacial Tension for CO2/CH4/Brine Systems under Reservoir Conditions. *Ind. Eng. Chem. Res.* **2016**, *55*, 12358−12375.

DOI: 10.1021/acs.jpcc.9b04432
J. Phys. Chem. C 2019, 123, 20877−20883